

Synthesis and Evaluation of Pyrazolopyrimidinyl-based  
TSPO Ligands for Cancer Imaging

By

Dewei Tang

Dissertation

Submitted to the Faculty of the  
Graduate School of Vanderbilt University

In partial fulfillment of the requirements

For the degree of

DOCTOR OF PHILOSOPHY

In

Chemical & Physical Biology

May, 2013

Nashville, TN

Approved:

H. Charles Manning, Ph.D.

John C. Gore, Ph.D.

Robert J. Coffey, M.D.

Thomas E. Yankeelov, Ph.D.

Brian O. Bachmann, Ph.D.

## ACKNOWLEDGEMENTS

With this work, I am especially thankful to my professor Dr. H. Charles Manning, an optimistic genius, who has been supportive and continuously encouraging to me as I fulfill my career goals. Without his guidance and persistent help, this dissertation would not have been possible.

I would like to thank my committee members, Professor John C. Gore , Professor Robert J. Coffey, Professor Thomas E. Yankeelov and Professor Brian O. Bachmann for their guidance during my Ph.D. studies. Special thanks to Professor John C. Gore and Professor Robert J. Coffey for their extensive personal and professional guidance, both in scientific research and life in general, as I aim to be a scientist. Special thanks to Professor Thomas E. Yankeelov and Professor Brian O. Bachmann for their professional suggestions and guidance during my qualifying exam and thesis research.

I am also grateful to those colleagues with whom I have had the pleasure to work during this project. These include members of the Manning laboratory, Dr. Jason R. Buck, Matthew R. Hight, Eliot T. McKinley, Allie Fu, Ping Zhao, Dr. Mohammed Noor Tantawy, Dr. Michael Nickels, and Sam Saleh. I am very appreciative of their help during these studies.

Finally, I would like to thank my parents and sister, whose love and guidance are always with me in whatever I pursue.

## TABLE OF CONTENTS

	Pages
ACKNOWLEDGEMENTS.....	ii
LIST OF TABLES.....	v
LIST OF FIGURES.....	vi
Chapter	
1. INTRODUCTION.....	1
1.1 Imaging TSPO in Glioma.....	4
1.2 A Strategy for Developing TSPO Imaging Probes.....	6
2. MICROWAVE-ASSISTED ORGANIC SYNTHESIS OF A HIGH-AFFINITY PYRAZOLOPYRIMIDINYL TSPO LIGAND.....	9
2.1 Abstract.....	9
2.2 Introduction.....	9
2.3 Results and Discussion.....	11
2.4 Conclusion.....	17
2.5 Results and Methods.....	18
3. QUANTITATIVE PRECLINICAL IMAGING OF TSPO EXPRESSION IN GLIOMA USING <sup>18</sup> F-DPA-714.....	28
3.1 Abstract.....	28
3.2 Introduction.....	28
3.3 Material and Methods.....	30
3.4 Results.....	36
3.5 Discussion.....	44
3.6 Conclusion.....	48
4. AN EFFICIENT STRATEGY TO GENERATE PYRAZOLOPRIMIDINE LIBRARIES: POTENTIAL MOLECULAR IMAGING LIGANDS FOR TRANSLOCATOR PROTEIN.....	49
4.1 Abstract.....	49
4.2 Introduction.....	49

4.3 Results and Discussion.....	51
4.4 Conclusion.....	55
4.5 Results and Methods.....	56
5. SYNTHESIS AND STRUCTURE-ACTIVITY RELATIONSHIPS OF 5,6,7- SUBSTITUTED PYRAZOLOPYRIMIDINES: DISCOVERY OF A NOVEL TSPO PET LIGAND FOR CANCER IMAGING.....	68
5.1. Abstract.....	68
5.2 Introduction.....	68
5.3 Results and Discussion.....	71
5.4 Conclusion.....	83
5.5 Results and Methods.....	84
6. QUANTITATIVE, PRECLINICAL EVALUATION OF NOVEL TSPO-PET LIGAND <sup>18</sup> F-VUIIS1008 TO IMAGE GLIOMA.....	102
6.1 Abstract.....	102
6.2 Introduction.....	103
6.2 Materials and Methods.....	105
6.3 Results.....	110
6.4 Discussion.....	116
6.5 Conclusion.....	118
7. CONCLUSION.....	119
BIBLIOGRAPHY.....	121

## LIST OF TABLES

TABLE	Page
2.1. Synthesis of 3-cyano- <i>N,N</i> -diethyl-4-(4-methoxyphenyl)-4-oxobutanamide.....	12
2.2. Synthesis of 2-(3-amino-5-(4-methoxyphenyl)-1 <i>H</i> -pyrazol-4-yl)- <i>N,N</i> -diethylacetamide.....	13
2.3. Synthesis of <i>N,N</i> -diethyl-2-(2-(4-methoxyphenyl)-5,7-dimethylpyrazolo[1,5- <i>a</i> ]pyrimidin-3-yl) acetamide (5, DPA-713).....	14
2.4. Synthesis of <i>N,N</i> -diethyl-2-(2-(4-hydroxyphenyl)-5,7-dimethylpyrazolo[1,5- <i>a</i> ]pyrimidin-3-yl) acetamide.....	14
2.5. Synthesis of <i>N,N</i> -diethyl-2-(2-(4-(2-fluoroethoxy)phenyl)-5,7-dimethylpyrazolo[1,5- <i>a</i> ]pyrimidin-3-yl)acetamide (7, DPA-714).....	15
2.6. Synthesis of 2-(4-(3-(2-(diethylamino)-2-oxoethyl)-5,7-dimethylpyrazolo[1,5- <i>a</i> ]pyrimidin-2-yl)phenoxy)ethyl 4-methylbenzenesulfonate.....	16
2.7. Synthesis of pyrazolopyrimidine intermediates.....	16
2.8. Synthesis of pyrazolopyrimidines.....	17
3.1. HPLC Radiometabolite Analysis of [ <sup>18</sup> F]DPA-714.....	38
3.2. Parameter Estimations for [ <sup>18</sup> F]DPA-714 Uptake.....	45
4.1. TSPO ligands obtained with the modified pyrazolopyrimidine MAOS.....	55
5.1. Affinity, lipophilicity, and molecular weight of pyrazolopyrimidines.....	74
6.1. Modeling fit of <sup>18</sup> F-VUIIS1008 with 1-tissue, 2-constant kinetic model and 2-tissue, 4-constant kinetic model.....	115
6.2. Comparison between <sup>18</sup> F-VUIIS1008 and <sup>18</sup> F-DPA-714.....	116

## LIST OF FIGURES

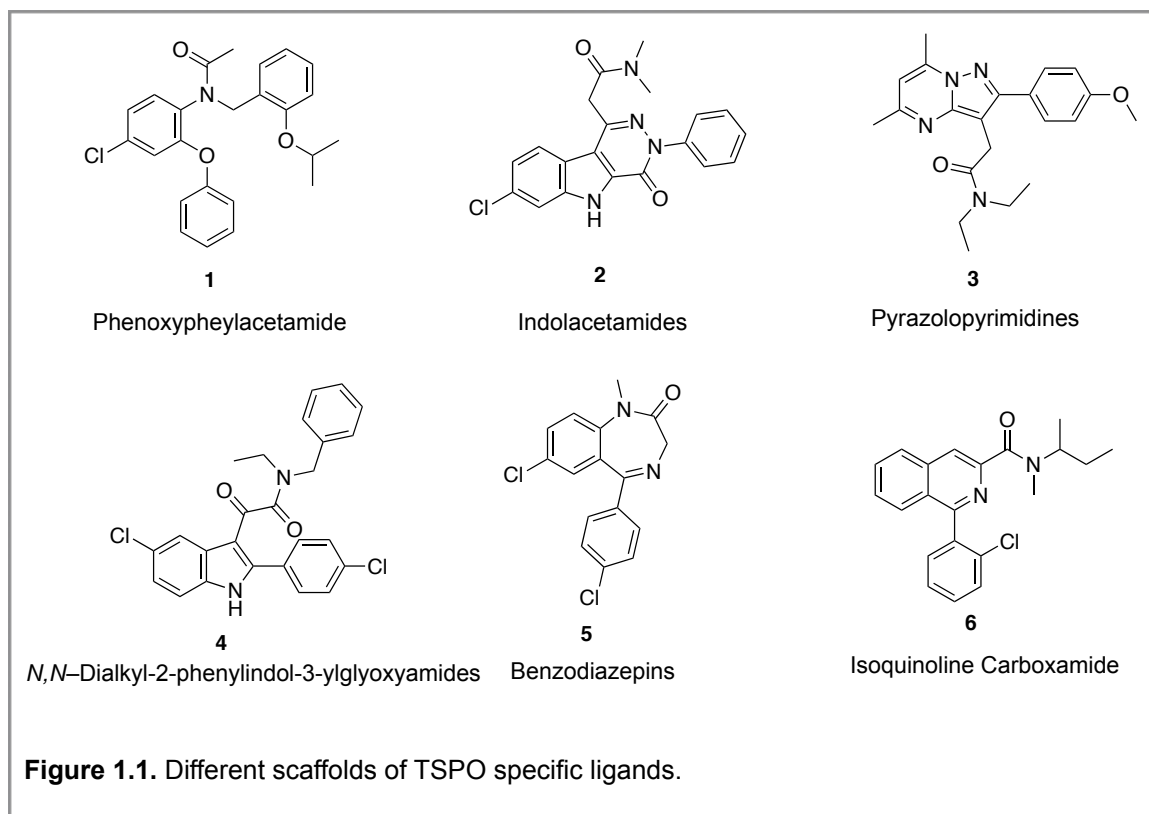
FIGURE	Page
1.1. Different scaffolds of TSPO specific ligands.....	2
1.2. Possible determinants of pyrazolopyrimidines to TSPO.....	7
3.1. Chemical structure and binding affinity curve of DPA-714.....	36
3.2. PET imaging and TACs for <sup>18</sup> F-DPA-714.....	38
3.3. <i>In vivo</i> displacement of <sup>18</sup> F-DPA-714 in C6 glioma-bearing rat.....	40
3.4. Comparison of <sup>18</sup> F-PBR06 and <sup>18</sup> F-DPA-714 in same glioma-bearing rat.....	41
3.5. Activity ratio for different components in the metabolite analysis.....	42
3.6. Pharmacokinetic model fit of typical <sup>18</sup> F-DPA-714 time-activity curves.....	43
3.7. Representative graphical analysis of $V_T$ for a subject from this investigation.....	44
3.8. TACs for Tumor and Brain with <sup>18</sup> F-DPA-714 in 11 rats.....	47
4.1. <sup>18</sup> F-DPA-714 and generic pyrazolopyrimidine scaffold.....	50
5.1. PET imaging of preclinical glioma using <sup>18</sup> F-6b.....	79
5.2. HPLC radiometabolite analysis <sup>18</sup> F-6b.....	80
5.3. Biodistribution of <sup>18</sup> F-6b in normal rat tissues.....	81
5.4. Crystal structure of 6b.....	82
6.1. Structure for DPA-714 and VUIIS1008.....	105
6.2. <sup>18</sup> F-VUIIS1008 accumulation and displacement in healthy mice.....	110
6.3. <sup>18</sup> F-VUIIS1008 accumulation and target specificity in C6 glioma.....	112
6.4. Compartment model with 2-tissue, 4-rate-constant kinetic model.....	113
6.5. Compartmental modeling with 1-tissue, 2-constants kinetic model.....	114

## CHAPTER 1

### INTRODUCTION

This multidisciplinary project seeks to develop, evaluate, and validate novel translocator protein (TSPO) positron emission tomography (PET) imaging ligands as probes for cancer imaging. Formerly referred to as peripheral benzodiazepine receptor (PBR), TSPO is an 18 kDa high-affinity cholesterol- and drug-binding protein that participates in regulation of numerous cellular processes, including cholesterol metabolism, steroid biosynthesis, proliferation and apoptosis.<sup>1</sup> Elevated TSPO expression is well-documented in neuroscience<sup>2-4</sup> and oncology.<sup>5</sup> To date, many preclinical and clinical studies have shown that tumors arising in the breast, prostate, oral cavity, colon, liver, and brain can express high levels of TSPO.<sup>6-16</sup> Given the role of TSPO in regulation of proliferation and BCL-2-mediated apoptosis, it is not surprising that TSPO expression tends to correlate with tumor proliferation and aggressive, invasive tumor behavior.<sup>17</sup> Clinically, TSPO levels predict metastatic potential, disease progression and diminished survival in patients with breast, oral, colorectal, and brain tumors.<sup>8</sup> Collectively, these data illuminate the potential significance of an *in vivo* assay of TSPO expression as a predictive biomarker in cancer.

The elevated expression and apparent functional role of TSPO in oncology suggest the attractiveness of assaying TSPO expression in tumors with molecular imaging. In part due to advancements in chemical synthesis, several



novel, structurally diverse TSPO ligand classes have been reported recently, including aryloxyanilides (1), indolacetamides (2), pyrazolopyrimidines (3), *N,N*-Dialkyl-2-phenylindol-3-ylglyoxyamides (4), benzodiazepines (5), and isoquinoline carboxamides (6) (**Fig. 1.1**). Several candidates from these classes exhibit significant improvements over the classic TSPO ligand, such as the isoquinoline carboxamide PK 11195 (**Fig 1.1**). A few of these ligands have been further developed as positron emission tomography (PET) imaging probes for neuroscience applications. Some of these imaging probes include [<sup>11</sup>C]PK 11195 and [<sup>18</sup>F]PK 14105; [<sup>11</sup>C]VC195; [<sup>11</sup>C]VC193M; [<sup>11</sup>C]Ro5-4864; [<sup>11</sup>C]DPA-713; [<sup>18</sup>F]DPA-714; [<sup>11</sup>C]DAA1106; [<sup>18</sup>F]FMDAA1106 and [<sup>18</sup>F]FEDAA1106; [<sup>11</sup>C]PBR28; and [<sup>11</sup>C]PBR01.<sup>18</sup> Surprisingly, very few TSPO imaging probes have been explored in oncology<sup>16, 19-21</sup> and few, if any, have been developed exclusively



for cancer imaging as we propose here. Central to our rationale, TSPO imaging ligands that are effective candidates for neuroscience applications may not be ideal tumor imaging agents. Unlike most non-neoplastic tissues, TSPO exists in polymeric form in many human tumors.<sup>22</sup> Compounds exhibiting excellent binding affinity for the 18 kDa monomer do not necessarily bind polymeric TSPO with the same efficiency<sup>23</sup>. Furthermore, characterization of tumor TSPO has revealed at least two coding mutations<sup>23</sup> and their impact on ligand binding has not been thoroughly explored. Significantly, highly aggressive and metastatic tumors tend to express both nuclear and mitochondrial TSPO,<sup>24</sup> a major departure from prototypical mitochondrial localization in non-neoplastic tissues. In general, these determinants are under-appreciated within the canonical TSPO ligand development paradigm. Consequently, the precise chemical and physical characteristics of ligands ideally suited for cancer imaging are not well understood.

In this study, we sought to test the hypothesis that TSPO ligands could be developed and optimized for cancer imaging studies. By exploiting many of the known tumor-specific TSPO molecular determinants throughout our experimental design, such as a tendency for polymerization and nuclear localization, we anticipate that our compound discovery program will be uniquely suited for identifying compounds relevant to cancer imaging. These efforts build upon our extensive prior experience exploring TSPO imaging ligands within the preclinical contexts of colorectal,<sup>7</sup> breast,<sup>25</sup> and brain cancer.<sup>26</sup> This dissertation has two

**Specific Aims:**

**[1] To synthesize novel, high-affinity TSPO ligands suitable for development as cancer imaging probes.** We will apply high-throughput parallel synthesis and automated sequential microwave-assisted organic synthesis (MAOS) methodologies<sup>27</sup> towards the optimization of pyrazoloprимidines. Candidates will be triaged using an innovative battery of physical and biochemical assays relevantly applied to TSPO expressed in tumors.

**[2] To evaluate promising TSPO imaging ligands *in vivo*.** The most promising candidate imaging ligands will be rigorously evaluated and validated using established preclinical brain tumor models (C6 glioma). Quantitative PET imaging data will be complemented by coregistered MRI metrics and subsequently correlated with coregistered histological and immunohistochemical sections of imaging-matched tumor specimens.

### **1.1 Imaging TSPO in Glioma**

The earliest published evidence supporting the hypothesis that TSPO ligands could be useful for detection and possibly grading of human brain tumors emerged more than twenty years ago,<sup>14, 28, 29</sup> easily predating molecular studies seeking elucidation for the role of TSPO in tumorigenesis, many of which continue today<sup>10, 17, 30, 31</sup>. The first proof-of-principle imaging studies employed [<sup>3</sup>H]PK 11195 and autoradiography to visualize TSPO expression in experimental models of glioma and post-mortem human brain sections<sup>14, 29, 32</sup>. These *ex vivo*

studies established that [<sup>3</sup>H]PK 11195, a highly selective TSPO ligand, without appreciable affinity for the central benzodiazepine receptor (CBR), could discriminate brain tumors from normal cortex. Furthermore, the amount of ligand uptake appeared to be proportional to tumor aggressiveness, cell proliferation, and tumor grade. Supported by these data, the first human PET studies using [<sup>11</sup>C]PK 11195 to image brain tumors were conducted, and these seminal investigations led to a number of important observations. In one report, Junck *et al.* imaged a range of human gliomas with [<sup>11</sup>C]PK 11195, as well as a different TSPO ligand, [<sup>11</sup>C]Ro5-4864.<sup>33</sup> While both PK 11195 and Ro5-4864 are potent and selective TSPO ligands with *in vitro* affinity in the low nanomolar range, this study established the clear superiority of [<sup>11</sup>C]PK 11195 over [<sup>11</sup>C]Ro5-4864 for brain tumor imaging. Surprisingly, PET scans with [<sup>11</sup>C]Ro5-4864 failed to demonstrate higher levels of radioactivity in tumor tissue than in normal brain, supporting an earlier autoradiography study comparing [<sup>3</sup>H]PK 11195 with [<sup>3</sup>H]Ro5-4864.<sup>33</sup> In contrast, [<sup>11</sup>C]PK 11195 demonstrated significantly elevated uptake in gliomas in 80% patients when compared to contralateral normal brain, with tumor/gray matter ratios approaching 2 in 3/10 patients.<sup>34</sup> In addition to the tumor-selective nature of [<sup>11</sup>C]PK 11195, these data illustrate that chemical, biochemical, and pharmacological determinant are not well understood regarding the rational selection of TSPO ligands as potential cancer imaging probes. In subsequent investigations, Pappata *et al.*<sup>33</sup> found similar levels of [<sup>11</sup>C]PK 11195 uptake in a glioma study when compared to the study reported by Junck *et al.*<sup>34</sup> However, these authors also performed a displacement study using a

nonradioactive ligand in this patient and demonstrated that slightly less than 30% of the [ $^{11}\text{C}$ ]PK 11195 was displaceable. Although both of these studies suggest the utility of TSPO ligands for brain tumor imaging, the relatively modest uptake and attendant contrast afforded by [ $^{11}\text{C}$ ]PK 11195 in tumor tissue compared to normal brain, despite considerably larger differences in relative TSPO expression, coupled with high levels of non-displaceable ligand binding, suggest that exploration and development of novel TSPO ligands could improve the prospects of advancing TSPO as a cancer imaging biomarker.

Based on this hypothesis, in our group, we explored the aryloxyanilide ligand, [ $^{18}\text{F}$ ]PBR06, as a PET tracer for glioma imaging.<sup>35</sup> PET studies with this agent illustrated the feasibility of using a TSPO ligand for molecular imaging of cancer. However, we observed a number of drawbacks with these agents, such as metabolism and relatively high uptake in normal brain, prompting our development of novel ligands that might boast superior properties. In this project, we focused on developing and evaluating novel pyrazolopyrimidines, a scaffold with proven TSPO affinity.

## **1.2 A Strategy for Developing TSPO Imaging Probes**

Initially, we evaluated a known pyrazolopyrimidine, [ $^{18}\text{F}$ ]-DPA-714, in preclinical models of glioma. This agent previously demonstrated nanomolar binding affinity for TSPO when evaluated against [ $^3\text{H}$ ]PK 11195.<sup>36</sup> Like [ $^{18}\text{F}$ ]PBR06, we found [ $^{18}\text{F}$ ]-DPA-714 to be an attractive probe in this setting, but not without certain limitations.<sup>37</sup> To improve on this agent, we first decide to retain the

pyrazolopyrimidine scaffold of DPA-713/DPA-714 since as a class the pyrazolopyrimidines are attractive due to their adaptability to high-throughput synthesis methods.<sup>27</sup> For example, in this project, we developed a rapid, automated MAOS of pyrazolopyrimidines that reduced the synthesis time of DPA-714 from weeks to hours.<sup>27</sup> Subsequently, we used these methods to synthesize a variety of novel pyrazolopyrimidines and evaluated structure-activity relationships (SARs) with *in vitro* binding assays. Previous structure-activity studies conducted by Selleri *et al.* demonstrated that substitution on the pyrimidine ring is important for developing high-binding affinity and highly selective compounds.<sup>38</sup> Therefore, our synthetic activities primarily focused on evaluating novel chemical space within this portion of the molecule (**Fig. 1.2**).

In summary, to determine a baseline for pyrazolopyrimidine performance in this setting, we first synthesized and carefully evaluated [<sup>18</sup>F]-DPA-714 in preclinical models of glioma (**Chapter 2** and **Chapter 3**). Finding this agent

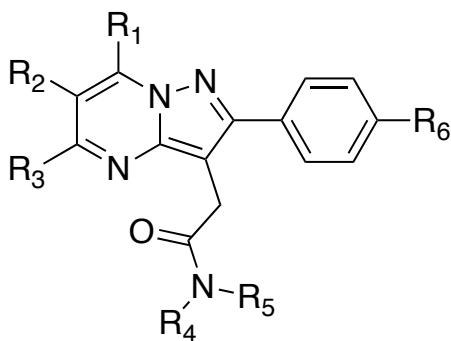


**Figure 1.2.** Possible determinants of pyrazolopyrimidines to TSPO (Adapted from Selleri *et al.*<sup>38</sup>).

promising in this setting, yet with drawbacks, we set-out to develop novel

pyrazolopyrimidines with improved properties (**Chapter 4**). This led to improved synthetic methods that yielded novel pyrazolopyrimidines, and the discovery of a significantly improved ligand, VUHS1008 (**Chapter 5**), which we evaluated in the C6 glioma model (**Chapter 6**). The discovery and superior performance of this agent highlights our efforts to develop an improved molecular imaging probe for cancer imaging.

## CHAPTER 2

### MICROWAVE-ASSISTED ORGANIC SYNTHESIS OF A HIGH-AFFINITY PYRAZOLOPYRIMIDINYL TSPO LIGAND

#### **2.1 Abstract**

We developed a dramatically improved total synthesis of the high-affinity translocator protein (TSPO) ligand DPA-714, featuring microwave-assisted organic synthesis (MAOS). Compared with previously described approaches, our novel MAOS method dramatically reduces overall reaction time without adversely affecting reaction yields. We envision that the described MAOS protocol may be suitably applied to high-throughput, diversity-oriented synthesis of novel compounds based on the pyrazolo-pyrimidinyl scaffold. Such an approach could accelerate the development of focused libraries of novel TSPO ligands with potential for future development as molecular imaging and therapeutic agents.

#### **2.2 Introduction**

Translocator protein (TSPO), formerly known as the peripheral benzodiazepine receptor (PBR), is an 18 kDa outer-mitochondrial membrane protein that participates in the regulation of numerous cellular processes, including cholesterol metabolism, steroid biosynthesis, proliferation and apoptosis.<sup>39, 40 41</sup> Under normal circumstances, TSPO expression tends to be

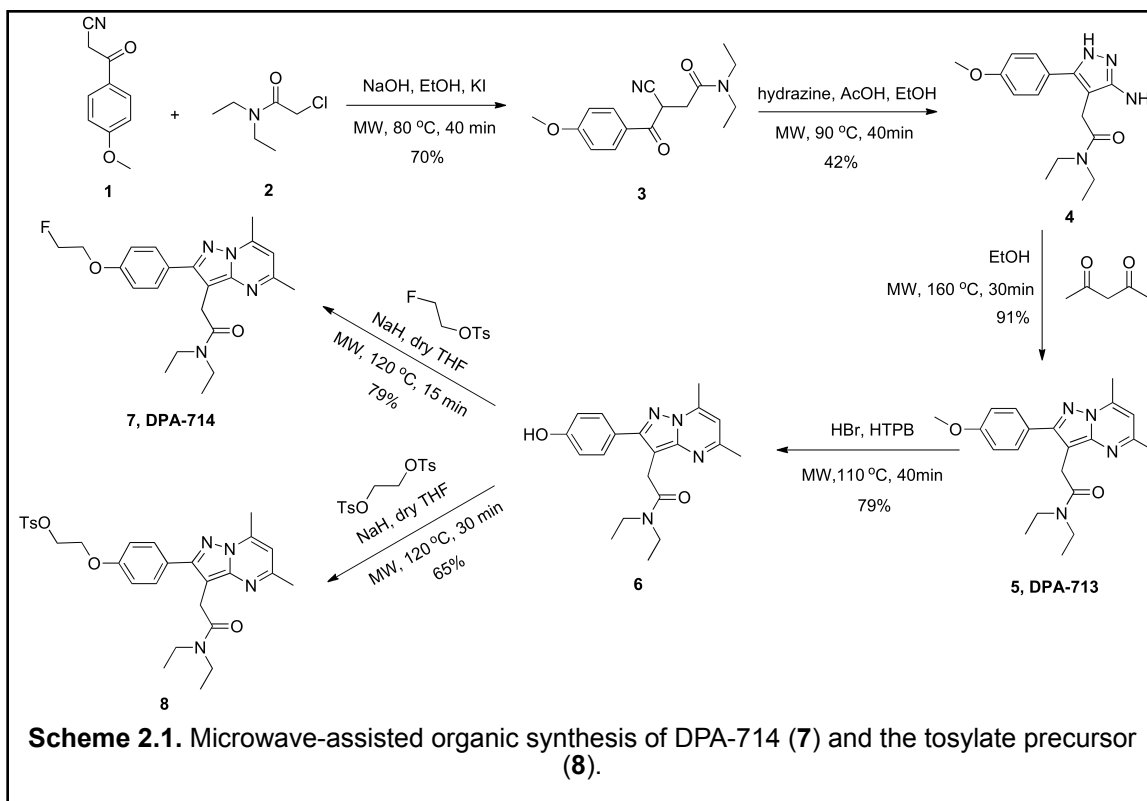
highest in steroid producing tissues and mitochondrial enriched tissues such as skeletal muscle, kidney and heart. TSPO expression is also elevated in disease states such as neuroinflammation and cancer.<sup>20, 42, 43</sup> For this reason, TSPO is regarded as a potentially important target for drug and molecular imaging probe development. Our previous research involving TSPO resulted in the development of several labeled TSPO ligands for *in vitro* and *in vivo* fluorescence imaging and high-throughput screening applications.<sup>7, 26, 44, 45</sup> Presently, a diverse array of TSPO-targeted probes has been developed and radiolabeled with positron emitting isotopes such as carbon-11 and fluorine-18 for positron emission tomography (PET) imaging.<sup>18</sup> One such compound, [<sup>18</sup>F]DPA-714 (*N,N*-diethyl-2-(2-(4-(2-[<sup>18</sup>F])fluoroethoxy)phenyl)-5,7-dimethylpyrazolo[1,5-*a*]pyrimidin-3-yl)acetamide, is a high-affinity TSPO ligand that has shown promise for PET imaging of neuroinflammation.<sup>36, 46</sup> Previous publications report total syntheses of this compound and its tosylate precursor, suitable for radiolabeling with fluorine-18, that incorporate lengthy, multi-step schema.<sup>38, 47, 48</sup> Our interest in evaluating pyrazolo-pyrimidinyl compounds as TSPO imaging ligands, such as [<sup>18</sup>F]DPA-714, led us to explore methodologies applicable to rapid, high-throughput synthesis of this compound and potentially novel analogues thereof. To this end, we have evaluated microwave assisted organic synthesis (MAOS) as an approach to accelerate the synthesis of DPA-714 and similar compounds. Compared with previously reported approaches, this study illustrates that MAOS applied to each reaction step dramatically reduces the overall time required to prepare the compound while achieving comparable, or in most cases, superior



synthetic yields. According to the authors, this is the first MAOS-facilitated synthesis of DPA-714 and accordingly, this methodology can be extended to the synthesis of similar pyrazolo-pyrimidinyl-based compounds. As evidence of this, we illustrate application of MAOS to several additional pyrazolo-pyrimidinyl synthetic intermediates with good utility.

### 2.3 Results and Discussion

The overall synthetic methodology utilized in this study is shown in **Scheme 2.1** Though the synthesis reported here utilized starting materials similar to previous methods, those syntheses were carried out either at room temperature or with conventional thermal heating. By applying MAOS to each step as further



described below, the overall reaction time could be reduced from over 50 hours to approximately three, while maintaining consistently high yields.

### 2.3.1. MAOS of 3-cyano-*N,N*-diethyl-4-(4-methoxyphenyl)-4-oxobutanamide (**3**)

The consecutive five-step synthesis begins with formation of **3** by reaction of 3-(4-methoxyphenyl)-3-oxopropanenitrile (**1**) and 2-chloro-*N,N*-diethylacetamide (**2**) in 80% EtOH, NaI/KI and NaOH. Previous studies carried out this reaction at either room temperature or reflux over 8 h with reported yields ranging from 10 – 70%.<sup>38, 47</sup> To reduce the reaction time required, microwave irradiation provided a reaction temperature of 80°C. Brief irradiation for 40 min and flash chromatography on silica gel gave **3** with a slightly higher yield when compared with the best previously reported method.<sup>47</sup> (**Table 2.1**)

Entry	MAOS	Reaction Conditions	Temperature	Time	Yield <sup>a</sup>
1 <sup>38</sup>	No	80% EtOH, NaI, NaOH	RT	8 h	10%
2 <sup>47</sup>	No	80% EtOH, NaI, NaOH	RT	8 h	64%
3	Yes	80% EtOH, KI, NaOH	80°C	40 min	70%

<sup>a</sup> Isolated yield. See reference.<sup>38, 47</sup>

### 2.3.2. Synthesis of 2(3-amino-5-(4-methoxyphenyl)-1H-pyrazol-4-yl)-*N,N*-diethylacetamide (**4**)

Synthesis of **4** features pyrazolo ring formation from the reaction of **3** with hydrazine. According to previous reports, this reaction can be carried out at room

temperature or with traditional thermal heating for 4 – 6 h in ethanol/acetic acid to achieve yields ranging from 68 – 72%.<sup>38, 47</sup> In this study, this reaction could be adapted to MAOS via microwave irradiation at 90°C for 40 min, albeit with a somewhat lower yield (42%) than previous studies (**Table 2.2**). Efforts to increase the reaction yield above 42% while maintaining the rapid 40 min reaction time included elevated temperature (> 90°C) and hydrazine concentration. However, these conditions resulted in increased byproduct formation and further diminished synthetic yields (data not shown). Despite the slightly reduced yield, the significantly increased speed with which this reaction could be performed using MAOS is a considerable advantage over traditional methods.

**Table 2.2. Synthesis of 2-(3-amino-5-(4-methoxyphenyl)-1H-pyrazol-4-yl)-N,N-diethylacetamide(4).**

Entry	MAOS	Reaction Conditions	Temperature	Time	Yield <sup>a</sup>
1 <sup>38</sup>	No	EtOH, acetic acid	RT	6 h	72%
2 <sup>47</sup>	No	EtOH, acetic acid	Reflux	4 h	68%
3	Yes	EtOH, acetic acid	90°C	40 min	42%

<sup>a</sup> Isolated yield. See reference.<sup>38, 47</sup>

### 2.3.3. MAOS of *N,N*-diethyl-2-(2-(4-methoxyphenyl)-5,7-dimethylpyrazolo [1,5-*a*] pyrimidin-3-yl) acetamide (5, DPA-713)

In the third step, **5** (DPA-713) was synthesized from the reaction of **4** and 2,4-pentanedione in ethanol. Previous studies have reported carrying out this reaction at room temperature or with conventional thermal heating.<sup>38, 47</sup> Optimization with microwave irradiation resulted in final reaction conditions of 160°C in ethanol for 30 min. Purification by flash chromatography on silica gel

gave **5** in near quantitative yield (91%), comparable to the best previously reported synthesis while requiring only a fraction of the reaction time.<sup>47</sup> (**Table 2.3**)

Entry	MAOS	Reaction Conditions	Temperature	Time	Yield <sup>a</sup>
1 <sup>38</sup>	No	EtOH	RT	4 h	44%
2 <sup>47</sup>	No	EtOH	Reflux	12 h	93%
3	Yes	EtOH	160°C	30 min	91%

<sup>a</sup> Isolated yield. See reference.<sup>38, 47</sup>

#### **2.3.4. MAOS of *N,N*-diethyl-2-(2-(4-hydroxyphenyl)-5,7-dimethylpyrazolo[1,5-a]pyrimidin-3-yl) acetamide (**6**)**

The fourth reaction in the synthesis of DPA-714 features deprotection of **5**, performed using either BBr<sub>3</sub> in CH<sub>2</sub>Cl<sub>2</sub> at -60°C or with aqueous HBr under conventional thermal conditions. To optimize this reaction with MAOS, examination of various reaction temperatures ranging from 100 to 140 °C demonstrated that temperatures > 120°C resulted in byproduct formation. However, irradiation at 110°C for 40 min in aqueous HBr with addition of hexadecyl tributyl phosphonium bromide (HTPB) proved successful. Compared

Entry	MAOS	Reaction Conditions	Temperature	Time	Yield <sup>a</sup>
1 <sup>47</sup>	No	HTPB, HBr, H <sub>2</sub> O	100°C	7 h	54%
2 <sup>49</sup>	No	BBr <sub>3</sub> , CH <sub>2</sub> Cl <sub>2</sub>	-60°C	2 h	55%
3	Yes	HTPB, HBr, H <sub>2</sub> O	110°C	40 min	79%

<sup>a</sup> Isolated yield. See reference.<sup>47, 49</sup>

to previously reported methods, this approach yielded **6** in higher yield (79%), with a significantly reduced reaction time (40 min versus 2 – 7 h) (**Table 2.4**).

### 2.3.5. MAOS of *N,N*-diethyl-2-(2-(4-(2-fluoroethoxy)phenyl)-5,7-dimethylpyrazolo[1,5-*a*]pyrimidin-3-yl) acetamide (**7**, DPA-714)

From compound **6**, reported syntheses of **7** describe reactions carried out at room temperature with NaH in dry THF for 16 h with yields ranging from 60 – 80%. Employing microwave irradiation, an optimized reaction temperature of 120°C was achieved with a subsequent reduction in reaction time from 16 h to 15 min, a factor of 64, while still achieving a comparable yield (79%) (**Table 2.5**)

Entry	MAOS	Reaction Conditions	Temperature	Time	Yield <sup>a</sup>
1 <sup>48</sup>	No	NaH, THF	RT	16 h	80%
2 <sup>49</sup>	No	NaH, THF	RT	16 h	58%
3	Yes	NaH, THF	120°C	15 min	79%

<sup>a</sup> Isolated yield. See reference.<sup>48, 49</sup>

### 2.3.6. MAOS of 2-(4-(3-(2-(diethylamino)-2-oxoethyl)-5,7-dimethylpyrazolo[1,5-*a*]pyrimidin-2-yl)phenoxy)ethyl-4-methylbenzenesulfonate (**8**), a precursor for radiosynthesis of [<sup>18</sup>F]DPA-714

In order to produce <sup>18</sup>F-labeled DPA-714 as a PET tracer, **8** is commonly prepared as the precursor. Previous syntheses of this compound were carried out at room temperature in high yield. However, the prolonged reaction time reported (16 h) is a considerable disadvantage. We found that this reaction could

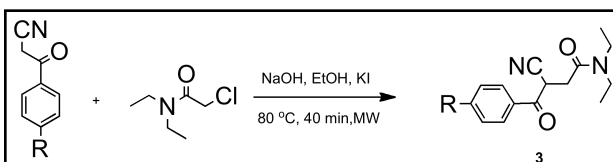
be optimized using microwave irradiation for 30 min at 120°C. Following purification, we obtained **8** in a yield of 65%, comparable to previous reports<sup>49</sup> (**Table 2.6**).

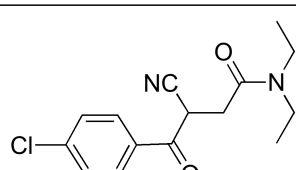
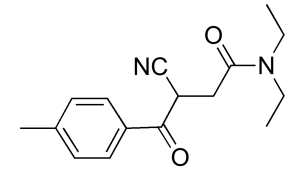
**Table 2.6. Synthesis of 2-(4-(3-(2-(diethylamino)-2-oxoethyl)-5,7-dimethylpyrazolo[1,5-a]pyrimidin-2-yl)phenoxy)ethyl 4-methylbenzenesulfonate (**8**).**

Entry	MAOS	Reaction Conditions	Temperature	Time	Yield <sup>a</sup>
1 <sup>48</sup>	No	NaH, THF	RT	16 h	59%
2 <sup>49</sup>	No	NaH, THF	RT	16 h	77%
3	Yes	NaH, THF	120°C	30 min	65%

<sup>a</sup> Isolated yield. See reference.<sup>48, 49</sup>

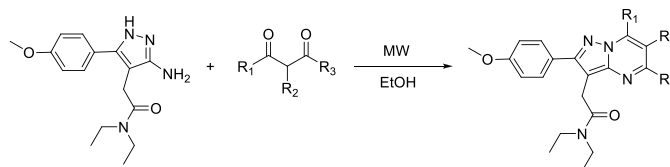
Extending the utility of MAOS to the synthesis of additional pyrazolo-pyrimidinyl-based compounds, we performed the first and third reactions shown in **Scheme 2.1** using a variety of different reagents, mimicking a library-based synthetic approach. For example, substitution of **1** with the corresponding *p*-chloro or *p*-methyl reagent results in rapid synthesis of **3a** and **3b** in acceptable yields (**Table 2.7**). Similarly, application of MAOS to reactions featuring unique diones also appears feasible, enabling synthesis of potential TSPO ligands following the third reaction (**Table 2.8**). Interestingly, in evaluating somewhat bulkier diones, we observed significantly



Entry	Product	Yield (%) <sup>a</sup>
<b>3a</b>		42
<b>3b</b>		40

<sup>a</sup> Isolated yield.

**Table 2.7. Synthesis of pyrazolopyrimidine intermediates.**

**Table 2.8.** Synthesis of pyrazolopyrimidines.

Entry	R <sub>1</sub>	R <sub>2</sub>	R <sub>3</sub>	Temperature (°C)	Time (min)	Yield (%) <sup>a</sup>
<b>5a</b>	-CF <sub>3</sub>		-CF <sub>3</sub>	160	30	11
<b>5b</b>	-CH <sub>3</sub>	-CH <sub>3</sub>	-CH <sub>3</sub>	160	30	77
<b>5c</b>	-CH <sub>3</sub>	-CH <sub>2</sub> CH <sub>3</sub>	-CH <sub>3</sub>	160	30	24
<b>5d</b>	-CH(CH <sub>3</sub> ) <sub>2</sub>		-CH(CH <sub>3</sub> ) <sub>2</sub>	180	45	6
<b>5e</b>	-Ph		-Ph	180	45	5
<b>5f</b>	-C(CH <sub>3</sub> ) <sub>3</sub>		-C(CH <sub>3</sub> ) <sub>3</sub>	195	60	0

<sup>a</sup> Isolated yield

reduced reaction yield, presumably due to the geometric constraints afforded by groups in R<sub>1</sub>, R<sub>2</sub> and R<sub>3</sub>. We anticipate that synthetic optimization of the bulkier pyrazolo-pyrimidines is possible, though beyond the scope of this focused work.

## 2.4 Conclusion

In summary, a detailed optimization of the total synthesis of a high-affinity TSPO ligand, DPA-714, utilizing MAOS, is described. The protocol reported here significantly improves overall reaction times while maintaining or even improving synthetic yields. We envision that this protocol can be extended to library synthesis of novel TSPO ligands with potential use for noninvasive visualization of TSPO expression *in vivo* as well as treatment of TSPO-expressing disease.

## 2.5 Results and Methods

**General information.** All commercially available reagents were used without further purification. All reactions were carried out with a Biotage Initiator™ Sixty microwave system (Uppsala, Sweden). All reaction residues were purified by Biotage flash purification system with SNAP silica cartridges. All <sup>1</sup>H- and <sup>13</sup>C-NMR spectra were recorded on a Bruker 400 MHz spectrometer. Chemical shifts are reported in ppm using the residual of chloroform as the internal standard (7.26 ppm for <sup>1</sup>H and 77.160 ppm for <sup>13</sup>C, respectively). All CH/CHN elemental analyses were performed by Atlantic Microlab, INC (Norcross, GA, USA).

### **3-cyano-*N,N*-diethyl-4-(4-methoxyphenyl)-4-oxobutanamide (3)**

To a solution of 3-(4-methoxyphenyl)-3-oxopropanenitrile (1.0 g, 5.71 mmol, **1**), 2-chloro-*N,N*-diethylacetamide (0.854 g, 5.71 mmol, **2**) in 80% EtOH (40 mL) were added NaOH (0.22 g, 5.71 mmol) and KI (2.84 g, 17.1 mmol). The mixture was irradiated in a Biotage Initiator at 80°C for 40 min. The reaction was monitored by TLC (Hexane/Ethyl acetate = 50/50, V:V). When completed, the mixture was filtered and extracted with CH<sub>2</sub>Cl<sub>2</sub>. The residue was concentrated and purified with flash chromatography on silica gel (Hexane/Ethyl acetate = 50/50, V:V) to afford **3** (1.14 g, 70%) as a brown oil. [Found: C, 62.06; H, 6.59; N, 8.56. C<sub>16</sub>H<sub>20</sub>N<sub>2</sub>NaO<sub>3</sub> requires C, 61.73; H, 6.48; N, 9.00%]. <sup>1</sup>H-NMR (CDCl<sub>3</sub>, 400 MHz) δ 8.05 (d, 2H, J = 8.8 Hz), 6.85 (d, 2H, J = 8.8 Hz), 5.00 (dd, 1H, J = 9.2 Hz, 4.5 Hz), 3.89 (s, 3H), 3.39 (m, 4H), 3.33 (m, 1H), 2.86 (m, 1H), 1.28 (t, 3H, J = 7.2 Hz), 1.09 (t, 3H, J = 7.2 Hz). <sup>13</sup>C-NMR (CDCl<sub>3</sub>, 400 MHz) δ 187.7, 167.1,



164.5, 131.4, 127.1, 117.5, 114.2, 55.5, 41.9, 40.6, 33.6, 32.5, 14.05, 12.9.

HRMS calcd for  $C_{16}H_{20}N_2O_3Na$   $m/z = 311.1372$  ( $M + Na$ )<sup>+</sup>, found 311.1381.

#### **2-(3-amino-5-(4-methoxyphenyl)-1H-pyrazol-4-yl)-N,N-diethylacetamide (4)**

To a solution of **3** (1.14 g, 3.95 mmol) in EtOH (18 mL) were added to hydrazine (0.126 g, 3.95 mmol) and AcOH (0.13 mL). The mixture was irradiated at 90°C for 40 min in a Biotage Initiator. Reaction was monitored with TLC ( $CH_2Cl_2/MeOH = 90/10$ , V:V). When completed, the residue was washed with saturated aqueous  $NaHCO_3$  (50 mL) and extracted with  $CH_2Cl_2$  (50 mL). The organic layer was then collected and concentrated in vacuo. Purification of the residue with flash chromatography on silica gel ( $CH_2Cl_2/MeOH = 100/0 - 90/10$ , V:V) afforded **4** (0.5 g, 42%) as yellow crystals. [Found: C, 58.60; H, 6.59; N, 16.90.  $C_{16}H_{22}N_4NaO_2$  requires C, 59.06, H, 6.82, N, 17.22%].  $^1H$ -NMR ( $CDCl_3$ , 400 MHz)  $\delta$  7.32 (d, 2H,  $J = 8.8$  Hz), 6.97 (d, 2H,  $J = 8.8$  Hz), 3.85 (s, 3H), 3.51 (s, 2H), 3.32 (m, 2H), 3.06 (m, 2H), 1.08 (t, 3H,  $J = 7.2$  Hz), 0.93 (t, 3H,  $J = 7.2$  Hz).  $^{13}C$ -NMR ( $CDCl_3$ , 400 MHz)  $\delta$  170.2, 159.8, 129.0, 126.6, 122.8, 114.3, 55.3, 42.3, 40.4, 28.5, 14.0, 13.0. HRMS calcd for  $C_{16}H_{23}N_2O_2$   $m/z = 303.1821$  ( $MH^+$ ), found 303.1814.

#### **N,N-diethyl-2-(2-(4-methoxyphenyl)-5,7-dimethylpyrazolo[1,5-a]pyrimidin-3-yl)acetamide (5, DPA-713)**

To a solution of **4** (0.5 g, 1.65 mmol) in EtOH (8.0 mL) was added 2,4-pentanedione (0.165 g, 1.65 mmol). The mixture was irradiated with a Biotage Initiator at 160°C for 30 min. Reaction was monitored with TLC (CH<sub>2</sub>Cl<sub>2</sub>/MeOH = 90/10, V:V). Following the reaction, the residue was purified with flash chromatography (CH<sub>2</sub>Cl<sub>2</sub>/MeOH = 100/0 - 90/10, V:V) to afford **5** (0.55 g, 91%) as brown crystals. [Found: C, 68.61; H, 6.98; N, 15.11. C<sub>21</sub>H<sub>26</sub>N<sub>4</sub>O<sub>2</sub> requires C, 68.83; H, 7.15; N, 15.29%] <sup>1</sup>H-NMR (CDCl<sub>3</sub>, 400 MHz) δ 7.78 (d, 2H, J = 8.8 Hz), 6.99 (d, 2H, J = 8.8 Hz), 6.50 (s, 1H), 3.92 (s, 2H), 3.85 (s, 3H), 3.50 (m, 2H), 3.41 (m, 2H), 2.74 (s, 3H), 2.54 (s, 3H), 1.20 (t, 3H, J = 7.2 Hz), 1.12 (t, 3H, J = 7.2 Hz). <sup>13</sup>C-NMR (CDCl<sub>3</sub>, 400 MHz) δ 170.0, 159.7, 157.3, 154.9, 147.6, 144.6, 129.9, 126.3, 113.8, 108.0, 100.7, 55.2, 42.2, 40.5, 28.1, 24.6, 16.8, 14.3, 13.0. HRMS calcd for C<sub>21</sub>H<sub>26</sub>N<sub>4</sub>O<sub>2</sub>Na m/z = 389.1953 (M + Na)<sup>+</sup>, found 389.1940.

***N,N*-diethyl-2-(2-(4-hydroxyphenyl)-5,7-dimethylpyrazolo[1,5-a]pyrimidin-3-yl)acetamide (6)**

To a solution of **5** (0.55 g, 1.5 mmol) in aqueous HBr (20 mL) was added HTPB (80.0 mg, 0.15 mmol). The reaction mixture was irradiated with a Biotage Initiator at 110°C for 40 min. The reaction was monitored with TLC (CH<sub>2</sub>Cl<sub>2</sub>/MeOH = 90/10, V:V). When completed, the mixture was then washed with saturated aqueous NaHCO<sub>3</sub> (50 mL) and extracted with CH<sub>2</sub>Cl<sub>2</sub> (50 mL x 2). The final product was purified with flash chromatography on silica gel (CH<sub>2</sub>Cl<sub>2</sub>/MeOH = 100/0 - 90/10, V:V) to afford **6** (0.48 g, 79%) as white crystals. [Found: C, 68.18; H, 7.28; N, 14.64. C<sub>20</sub>H<sub>24</sub>N<sub>4</sub>O<sub>2</sub> requires C, 68.16; H, 6.86; N, 15.90%]. <sup>1</sup>H-

NMR (CDCl<sub>3</sub>, 400 MHz) δ 7.66 (d, 2H, J = 8.8 Hz), 6.83 (d, 2H, J = 8.8 Hz), 6.50 (s, 1H), 3.96 (s, 2H), 3.51 (m, 2H), 3.39 (m, 2H), 2.74 (s, 3H), 2.54 (s, 3H), 1.16 (t, 3H, J = 7.2 Hz), 1.09 (t, 3H, J = 7.2 Hz). <sup>13</sup>C-NMR (CDCl<sub>3</sub>, 400 MHz) δ 170.5, 157.4, 156.9, 155.3, 147.4, 144.7, 129.9, 125.2, 115.6, 108.1, 100.3, 42.4, 40.7, 28.3, 24.5, 16.9, 14.1, 12.9. HRMS calcd for C<sub>20</sub>H<sub>24</sub>N<sub>4</sub>O<sub>2</sub>Na m/z = 375.1797 (M + Na)<sup>+</sup>, found 375.1793.

***N,N*-diethyl-2-(2-(4-(2-fluoroethoxy)phenyl)-5,7-dimethylpyrazolo[1,5-a]pyrimidin-3-yl)acetamide (7, DPA-714)**

To a suspension of NaH (7.4 mg, 0.305 mmol) in dry THF (4.0 mL) was added **6** (54.0 mg, 0.15 mmol). The reaction mixture was stirred for 10 min at 0 °C and then allowed to warm to room temperature before the addition of a solution of 2-fluoroethyl-4-methylbenzenesulfonate (100 mg, 0.46 mmol) in dry THF (1.0 mL). The mixture was irradiated at 120°C for 15 min with a Biotage Initiator. The reaction was monitored with TLC (CH<sub>2</sub>Cl<sub>2</sub>/MeOH = 95/5, V:V). When completed, reaction residue was partitioned with aqueous 1.0 M HCl (50 mL) and CH<sub>2</sub>Cl<sub>2</sub> (50 mL). The organic layer was then collected and concentrated *in vacuo*. Final purification of the residue with flash chromatography on silica gel (CH<sub>2</sub>Cl<sub>2</sub>/MeOH = 100/0 – 95/5, V:V) afforded **7** (48.2 mg, 79%) as white crystals. [Found: C, 66.56; H, 6.94. C<sub>22</sub>H<sub>27</sub>FN<sub>4</sub>O<sub>2</sub> requires C, 66.31; H, 6.83%]. <sup>1</sup>H-NMR (CDCl<sub>3</sub>, 400 MHz) δ 7.79 (d, 2H, J = 8.8 Hz), 7.01 (d, 2H, J = 8.8 Hz), 6.50 (s, 1H), 4.84 (t, 1H, 4.4Hz), 4.71(t, 1H, 4.4Hz) 4.30 (t, 1H, 4.4Hz), 4.23 (t, 1H, 4.4Hz), 3.91 (s, 2H), 3.51 (m, 2H), 3.41 (m, 2H), 2.73 (s, 3H), 2.54 (s, 3H), 1.20 (t, 3H, J = 7.2

Hz), 1.11 (t, 3H, J = 7.2 Hz). <sup>13</sup>C-NMR (CDCl<sub>3</sub>, 400 MHz) δ 170.0, 158.5, 157.4, 154.8, 130.0, 126.9, 114.6, 108.1, 100.8, 67.1, 40.5, 28.1, 24.5, 16.8, 14.3, 13.0. HRMS calcd for C<sub>22</sub>H<sub>27</sub>FN<sub>4</sub>O<sub>2</sub>Na m/z = 421.2016 (M + Na)<sup>+</sup>, found 421.2006.

**2-(4-(3-(2-(diethylamino)-2-oxoethyl)-5,7-dimethylpyrazolo[1,5-a]pyrimidin-2-yl)phenoxy)ethyl 4-methylbenzenesulfonate (8)**

To a suspension of NaH (1.7 mg, 0.34 mmol) in dry THF (5.0 mL) was added **6** (40 mg, 0.11 mmol). The reaction mixture was stirred for 10 min at 0 °C and then allowed to warm up to room temperature before addition of a solution of ethylene di(p-toluenesulfonate) (126 mg, 0.34 mmol). The mixture was irradiated with a Biotage Initiator at 120°C for 30 min. Reaction was monitored with TLC (CH<sub>2</sub>Cl<sub>2</sub>/MeOH = 95/5, V:V). When completed, reaction residue was partitioned with aqueous 1.0 M HCl (50 mL) and CH<sub>2</sub>Cl<sub>2</sub> (100 mL). The organic layer was then collected and concentrated *in vacuo*. Final purification of the residue with flash chromatography on silica gel (CH<sub>2</sub>Cl<sub>2</sub>/MeOH = 100/0 – 95/5, V:V) afforded **8** (40.5 mg, 65.1%) as white crystals. [Found: C, 63.25; H, 6.45; S, 5.69. C<sub>29</sub>H<sub>34</sub>N<sub>4</sub>O<sub>5</sub>S requires C, 63.25; H, 6.22; S, 5.82%]. <sup>1</sup>H-NMR (CDCl<sub>3</sub>, 400 MHz) δ 7.83 (d, 2H, 8.8 Hz), 7.75 (d, 2H, 8.8 Hz), 7.35 (d, 2H, J = 8.0 Hz), 6.86 (d, 2H, J = 8.8 Hz), 6.50 (s, 1H), 4.38 (t, 2H, J = 4.4 Hz), 4.18 (t, 2H, 4.4 Hz), 3.90 (s, 2H), 3.51 (m, 2H), 3.40 (m, 2H), 2.73 (s, 3H), 2.53 (s, 3H), 2.45 (s, 3H), 1.20 (t, 3H, J = 7.2 Hz), 1.11 (t, 3H, 7.2 Hz). <sup>13</sup>C-NMR (CDCl<sub>3</sub>, 400 MHz) δ 170.0, 158.1, 157.4, 154.7, 147.6, 144.9, 144.6, 132.8, 129.9, 129.8, 127.9, 127.1, 114.5, 108.2,

100.75, 68.04, 65.36, 42.24, 40.52, 28.04, 24.57, 21.58, 16.81, 14.28, 13.01.

HRMS calcd for C<sub>29</sub>H<sub>35</sub>N<sub>4</sub>O<sub>5</sub>S, m/z = 551.2328 (MH<sup>+</sup>), found 551.2318.

#### **4-(4-chlorophenyl)-3-cyano-*N,N*-diethyl-4-oxobutanamide (3a)**

To a solution of 3-(4-chlorophenyl)-3-oxopropanenitrile (240 mg, 1.30 mmol), 2-chloro-*N,N*-diethylacetamide (0.2 g, 1.30 mmol) in 80% EtOH (10 mL) were added NaOH (52 mg, 1.30 mmol) and KI (645 mg, 3.90 mmol). The mixture was irradiated in a Biotage Initiator at 80°C for 40 min. The reaction was monitored by TLC (Hexane/Ethyl acetate = 50/50, V:V). When completed, the mixture was filtered and extracted with CH<sub>2</sub>Cl<sub>2</sub>. The residue was concentrated and purified with flash chromatography on silica gel (Hexane/Ethyl acetate = 50/50, V:V) to afford **3a** (160 mg, 42%) as a dark oil. [Found: C, 60.09; H, 5.81; N, 9.57. C<sub>15</sub>H<sub>17</sub>ClN<sub>2</sub>O<sub>2</sub> requires C, 61.54; H, 5.85; N, 9.57%]. <sup>1</sup>H-NMR (CDCl<sub>3</sub>, 400 MHz) δ 8.00 (d, 2H, J = 8.7 Hz), 7.50 (d, 2H, J = 8.7 Hz), 4.97 (dd, 1H, J = 9.6 Hz, 4.4 Hz), 3.38 (m, 4H), 3.32 (m, 1H), 2.88 (m, 1H), 1.28 (t, 3H, J = 7.2 Hz), 1.09 (t, 3H, J = 7.2 Hz). <sup>13</sup>C-NMR (CDCl<sub>3</sub>, 400 MHz) δ 188.5, 166.9, 141.1, 130.3, 129.3, 116.8, 42.0, 40.6, 33.8, 29.6, 14.0, 12.9. HRMS calcd for C<sub>15</sub>H<sub>17</sub>ClN<sub>2</sub>O<sub>2</sub>Na m/z = 315.0876 (M + Na)<sup>+</sup>, found 315.0877.

#### **3-cyano-*N,N*-diethyl-4-oxo-4-*p*-tolylbutanamide (3b)**

To a solution of 3-oxo-3-*p*-tolylpropanenitrile (213 mg, 1.30 mmol), 2-chloro-*N,N*-diethylacetamide (0.2 g, 1.30 mmol) in 80% EtOH (10 mL) were added

NaOH (52 mg, 1.30 mmol) and KI (645 mg, 3.90 mmol). The mixture was irradiated in a Biotage Initiator at 80°C for 40 min. The reaction was monitored by TLC (Hexane/Ethyl acetate = 50/50, V:V). When completed, the mixture was filtered and extracted with CH<sub>2</sub>Cl<sub>2</sub>. The residue was concentrated and purified with flash chromatography on silica gel (Hexane/Ethyl acetate = 50/50, V:V) to afford **3b** (140 mg, 40%) as a dark oil. [Found: C, 69.92; H, 7.40; N, 9.90. C<sub>16</sub>H<sub>20</sub>N<sub>2</sub>O<sub>2</sub> requires C, 70.56; H, 7.40; N, 10.29%]. <sup>1</sup>H-NMR (CDCl<sub>3</sub>, 400 MHz) δ 7.94 (d, 2H, J = 8.3 Hz), 7.29 (d, 2H, J = 8.0 Hz), 5.01 (dd, 1H, J = 9.2 Hz, 4.4 Hz), 3.34 (m, 4H), 3.32 (m, 1H), 2.86 (m, 1H), 2.41 (s, 3H), 1.24 (t, 3H, J = 7.2 Hz), 1.06 (t, 3H, J = 7.2 Hz). <sup>13</sup>C-NMR (CDCl<sub>3</sub>, 400 MHz) δ 189.1, 167.0, 145.6, 131.7, 129.8, 129.0, 117.3, 41.9, 40.6, 33.8, 32.5, 21.7, 14.0, 12.9. HRMS calcd for C<sub>16</sub>H<sub>20</sub>N<sub>2</sub>O<sub>2</sub>Na m/z = 295.1413 (M + Na)<sup>+</sup>, found 295.1422.

***N,N*-diethyl-2-(2-(4-methoxyphenyl)-5,6,7-trimethylpyrazolo[1,5-a]pyrimidin-3-yl)acetamide (5a)**

To a solution of **4** (50 mg, 0.165 mmol) in EtOH (1 mL) was added 3-methylpentane-2,4-dione (18.8 mg, 0.165 mmol). The mixture was irradiated with a Biotage Initiator at 160°C for 30 min. Reaction was monitored with TLC (CH<sub>2</sub>Cl<sub>2</sub>/MeOH = 90/10, V:V). Following the reaction, the residue was purified with flash chromatography (CH<sub>2</sub>Cl<sub>2</sub>/MeOH = 100/0 - 90/10, V:V) to afford **5b** (48.1 mg, 77%) as brown crystals. [Found: C, 64.37; H, 7.18; N, 12.06. C<sub>22</sub>H<sub>28</sub>N<sub>4</sub>O<sub>2</sub> requires C, 69.45; H, 7.42; N, 14.73%]. <sup>1</sup>H-NMR (CDCl<sub>3</sub>, 400 MHz) δ 7.78 (d, 2H, J = 8.8 Hz), 6.98 (d, 2H, J = 8.8 Hz), 3.91 (s, 2H), 3.85 (s, 3H), 3.49

(m, 2H), 3.41(m, 2H), 2.79 (s, 3H), 2.55 (s, 3H), 2.28 (s, 3H), 1.19 (t, 3H, J = 7.2 Hz), 1.11 (t, 3H, J = 7.2 Hz). <sup>13</sup>C-NMR (CDCl<sub>3</sub>, 400 MHz) δ 170.2, 159.6, 157.4, 153.8, 145.9, 141.6, 129.9, 126.5, 113.8, 100.2, 55.2, 42.2, 40.5, 28.1, 24.1, 14.2, 13.9, 13.4, 13.0. HRMS calcd for C<sub>22</sub>H<sub>29</sub>N<sub>4</sub>O<sub>2</sub>, m/z = 381.2291 (MH<sup>+</sup>), found 381.2276.

***N,N*-diethyl-2-(6-ethyl-2-(4-methoxyphenyl)-5,7-dimethylpyrazolo[1,5-a]pyrimidin-3-yl)acetamide (5b)**

To a solution of **4** (50 mg, 0.165 mmol) in EtOH (1 mL) was added 3-ethylpentane-2,4-dione (21.15 mg, 0.165 mmol). The mixture was irradiated with a Biotage Initiator at 160°C for 30 min. Reaction was monitored with TLC (CH<sub>2</sub>Cl<sub>2</sub>/MeOH = 90/10, V:V). Following the reaction, the residue was purified with flash chromatography (CH<sub>2</sub>Cl<sub>2</sub>/MeOH = 100/0 - 90/10, V:V) to afford **5c** (15.7 mg, 24%) as brown crystals. [Found: C, 65.35; H, 7.30; N, 12.22. C<sub>23</sub>H<sub>30</sub>N<sub>4</sub>O<sub>2</sub> requires C, 70.02; H, 7.66; N, 14.20%] <sup>1</sup>H-NMR (CDCl<sub>3</sub>, 400 MHz) δ 7.78 (d, 2H, J = 8.8 Hz), 6.98 (d, 2H, J = 8.8 Hz), 3.91 (s, 2H), 3.85 (s, 3H), 3.51 (m, 2H), 3.41(m, 2H), 2.79 (s, 3H), 2.72 (m, 2H), 2.58 (s, 3H), 1.19 (m, 6H), 1.12 (t, 3H, J = 7.2 Hz). <sup>13</sup>C-NMR (CDCl<sub>3</sub>, 400 MHz) δ 170.3, 159.6, 156.9, 154.0, 145.9, 141.7, 129.9, 126.5, 119.9, 113.9, 100.3, 55.2, 42.2, 40.5, 28.0, 23.3, 21.3, 14.3, 14.1, 13.0, 12.9. HRMS calcd for C<sub>23</sub>H<sub>31</sub>N<sub>4</sub>O<sub>2</sub>, m/z = 385.2447 (MH<sup>+</sup>), found 395.2436.

**2-(5,7-diisopropyl-2-(4-methoxyphenyl)pyrazolo[1,5-a]pyrimidin-3-yl)-N,N-diethylacetamide (5c)**

To a solution of **4** (50 mg, 0.165 mmol) in EtOH (1 mL) was added 2,6-dimethylheptane-3,5-dione (25.7 mg, 0.165 mmol). The mixture was irradiated with a Biotage Initiator at 180°C for 45 min. Reaction was monitored with TLC (CH<sub>2</sub>Cl<sub>2</sub>/MeOH = 90/10, V:V). Following the reaction, the residue was purified with flash chromatography (CH<sub>2</sub>Cl<sub>2</sub>/MeOH = 100/0 - 90/10, V:V) to afford **5d** (4 mg, 6%) as yellow crystals. [Found: C, 68.76; H, 7.86; N, 12.55. C<sub>25</sub>H<sub>34</sub>N<sub>4</sub>O<sub>2</sub> requires C, 71.06; H, 8.11; N, 13.26%] <sup>1</sup>H-NMR (CDCl<sub>3</sub>, 400 MHz) δ 7.89 (d, 2H, J = 8.8 Hz), 7.00 (d, 2H, J = 8.8 Hz), 6.50 (s, 1H), 3.93 (s, 2H), 3.89 (m, 1H), 3.86 (s, 3H), 3.62 (m, 2H), 3.41(m, 2H), 3.04 (m, 1H), 1.44 (d, 6H, J = 6.8 Hz), 1.32 (d, 6H, J = 6.8 Hz), 1.22 (t, 3H, J = 7.2 Hz), 1.11 (t, 3H, J = 7.2 Hz). <sup>13</sup>C-NMR (CDCl<sub>3</sub>, 400 MHz) δ 170.60, 165.9, 159.7, 154.7, 154.1, 147.5, 126.5, 113.8, 101.7, 100.7, 55.2, 42.5, 40.7, 36.4, 28.1, 28.0, 20.0, 14.4, 13.1. HRMS calcd for C<sub>25</sub>H<sub>35</sub>N<sub>4</sub>O<sub>2</sub>, m/z = 423.2760 (MH<sup>+</sup>), found 423.2755.

**N,N-diethyl-2-(2-(4-methoxyphenyl)-5,7-diphenylpyrazolo[1,5-a]pyrimidin-3-yl)acetamide (5d)**

To a solution of **4** (50 mg, 0.165 mmol) in EtOH (1 mL) was added 1,3-diphenylpropane-1,3-dione (80 mg, 0.33 mmol). The mixture was irradiated with a Biotage Initiator at 180°C for 45 min. Reaction was monitored with TLC (CH<sub>2</sub>Cl<sub>2</sub>/MeOH = 90/10, V:V). Following the reaction, the residue was purified



with flash chromatography ( $\text{CH}_2\text{Cl}_2/\text{MeOH} = 100/0 - 90/10, \text{V:V}$ ) to afford **5e** (4 mg, 5%) as yellow crystals. [Found: C, 71.89; H, 6.13; N, 10.06.  $\text{C}_{31}\text{H}_{30}\text{N}_4\text{O}_2$  requires C, 75.89; H, 6.16; N, 11.42%]  $^1\text{H-NMR}$  ( $\text{CDCl}_3, 400 \text{ MHz}$ )  $\delta$  8.20 (m, 2H), 8.15 (m, 2H), 7.89 (d, 2H,  $J = 4.8 \text{ Hz}$ ), 7.58 (m, 3H), 7.51 (m, 3H), 7.33 (s, 1H), 6.99 (d, 2H,  $J = 4.8 \text{ Hz}$ ), 4.09 (s, 2H), 3.86 (s, 3H), 3.64 (m, 2H), 3.46 (m, 2H), 1.28 (d, 3H,  $J = 4.8 \text{ Hz}$ ), 1.15 (d, 3H,  $J = 4.8 \text{ Hz}$ ).  $^{13}\text{C-NMR}$  ( $\text{CDCl}_3, 400 \text{ MHz}$ )  $\delta$  170.2, 159.8, 155.7, 154.8, 148.8, 146.0, 137.8, 131.5, 130.7, 130.0, 129.9, 129.4, 128.7, 128.5, 127.1, 126.2, 113.8, 102.0, 55.2, 42.5, 40.7, 28.3, 14.4, 13.1. HRMS calcd for  $\text{C}_{31}\text{H}_{31}\text{N}_4\text{O}_2$ ,  $m/z = 491.2447$  ( $\text{MH}^+$ ), found 491.24

## CHAPTER 3

### QUANTITATIVE PRECLINICAL IMAGING OF TSPO EXPRESSION IN GLIOMA USING $^{18}\text{F}$ -DPA-714

#### 3.1 Abstract

There is a critical need to develop and rigorously validate molecular imaging biomarkers to aid diagnosis and characterization of primary brain tumors. Elevated expression of translocator protein (TSPO) has been shown to predict disease progression and aggressive, invasive behavior in a variety of solid tumors. Thus, noninvasive molecular imaging of TSPO expression could form the basis of a novel, predictive cancer imaging biomarker. In quantitative preclinical PET studies, we evaluated a high-affinity pyrazolopyrimidinyl-based TSPO imaging ligand, *N,N*-diethyl-2-(2-(4-(2-( $^{18}\text{F}$ )-fluoroethoxy)phenyl)-5,7-dimethylpyrazolo[1,5-*a*]pyrimidin-3-yl)acetamide ( $^{18}\text{F}$ ]DPA-714), as a translational probe for quantification of TSPO levels in glioma.

#### 3.2 Introduction

Malignant gliomas are the most common primary brain tumor and are characterized by invasive growth and recalcitrance to therapy. Currently, diagnosis and grading of gliomas are based upon the pathology of resected specimens with limitations inherent to sampling errors and heterogeneity. Given these limitations, clinical decisions are routinely guided by imaging<sup>50</sup>. The most common imaging metrics employed to detect and diagnose brain tumors are

computed tomography (CT) and magnetic resonance imaging (MRI). These modalities provide little, if any, molecular information attributable to the pathological status of the disease. Furthermore, numerous studies document the inherent difficulty associated with determination of brain tumor extent using CT and/or MRI, particularly with infiltrative disease. Positron emission tomography (PET) imaging using [<sup>18</sup>F]FDG is an important technique for brain tumor detection. However, high glucose uptake in normal brain results in modest tumor-to-background ratios with [<sup>18</sup>F]FDG, which can confound delineation of disease margins and subsequent grading. Therefore, there is a considerable need to develop and validate improved molecular imaging techniques suitable for detection and/or molecular profiling of brain tumors.<sup>51</sup>

Translocator protein (TSPO), also referred to as peripheral benzodiazepine receptor (PBR), is an 18 kDa protein typically localized to the outer mitochondrial membrane. TSPO participates in regulation of numerous cellular processes, including cholesterol metabolism, steroid biosynthesis, cellular proliferation, and apoptosis.<sup>1</sup> In normal tissues, TSPO expression tends to be highest in steroid-producing and mitochondrial-enriched tissues such as skeletal muscle, renal tissue, and myocardium, while tissues such as liver and brain exhibit comparatively modest expression<sup>1</sup>. Elevated TSPO expression is found in numerous disease states, including neuroinflammation<sup>2</sup> and neurological disorders such as Alzheimer's<sup>52</sup> and Huntington's disease,<sup>10</sup> as well as cancers of the breast,<sup>10, 11</sup> prostate,<sup>9</sup> oral cavity,<sup>53</sup> colon,<sup>20</sup> liver,<sup>15</sup> and brain.<sup>14, 54</sup> Elevated TSPO expression has also been linked with disease progression and diminished

survival in patients with oral,<sup>16, 53</sup> colorectal,<sup>20</sup> breast,<sup>5</sup> and brain cancer.<sup>55</sup> Additionally, elevated TSPO levels appear to be associated with aggressive, metastatic behavior in breast and colorectal cancer.<sup>10, 56</sup> Collectively, these data illuminate TSPO expression as a potentially important prognostic biomarker in oncology and suggest the utility of tumor-selective TSPO PET ligands for cancer imaging.

Recently, a variety of novel TSPO PET ligands have emerged from the literature, including aryloxyanilides, indoleacetamides, pyrazolopyrimidines, and imidazolepyridines.<sup>18</sup> We recently reported <sup>18</sup>F-*N*-fluoroacetyl-*N*-(2,5-dimethoxybenzyl)-2-phenoxyaniline ([<sup>18</sup>F]PBR06) as a high-affinity tracer for visualization of brain tumors, as well as quantification of TSPO expression in tumor and normal tissue.<sup>35</sup> The goal of the present study was to evaluate another high-affinity TSPO PET ligand, [<sup>18</sup>F]DPA-714, in cancer imaging studies. Our data illustrate the feasibility of using [<sup>18</sup>F]DPA-714 for visualization of TSPO-expressing brain tumors. Importantly, [<sup>18</sup>F]DPA-714 appears suitable for quantitative assay of tumor TSPO levels in vivo. Given the relationship between elevated TSPO levels and poor outcome in oncology, these studies suggest the potential of [<sup>18</sup>F]DPA-714 PET to serve as a novel and predictive cancer imaging modality.

### **3.3 Material and Methods**

## **Chemicals, Ligand and Radioligand Precursor Preparation**

[<sup>3</sup>H]PK 11195 was purchased from PerkinElmer. Phosphate buffered saline (PBS) and CytoScint ES Liquid Scintillation Cocktail were purchased from MP Biomedicals. All synthesis reagents were purchased from Sigma-Aldrich. [<sup>19</sup>F]DPA-714 (DPA-714) and radioligand precursor were prepared according to published methods.<sup>27</sup>

## ***In Vitro* Radioligand Binding Assay**

Radioligand binding experiments were conducted utilizing C6 glioma cell lysates as previously described, using DPA-714 as the cold ligand.<sup>35, 39</sup> All experiments were performed in triplicate.

## **Radioligand Preparation**

[<sup>18</sup>F]DPA-714 was prepared analogously to published methods.<sup>57</sup> In short, using a commercial apparatus (TRACERlab FXF-N, GE Medical Systems), aqueous [<sup>18</sup>F]fluoride ion (~ 111 GBq) was dried by iterative cycles of addition and evaporation of acetonitrile, followed by complexation with  $K^+ \cdot K^{+2.2.2}/K_2CO_3$ . The complex was reacted with 4-(3-(2-(diethylamino)-2-oxoethyl)-5,7-dimethylpyrazolo[1,5-a]pyrimidin-2-yl)phenethyl 4-methylbenzenesulfonate (3.0 mg) at 165°C for 5 min in dimethyl sulfoxide (0.6 mL). Purification of [<sup>18</sup>F]DPA-714 was carried out using reversed-phase HPLC (C18, Dynamax 250 × 21.4 mm; Varian) eluted at 6.0 mL/min with 10 mM NaH<sub>2</sub>PO<sub>4</sub> buffer (pH 6.7) and ethanol (47.5:52.5; v/v). [<sup>18</sup>F]DPA-714 was collected, washed with 120 mL water

(deionized), and eluted from a C18 Sep-Pak with ethanol (1.0 mL) into a sterile flask loaded with saline (9.0 mL). Typical specific activities were  $\geq 418$  TBq/mmol.

### **Rat Model**

All studies involving animals were conducted in compliance with federal and institutional guidelines. Two weeks prior to imaging, healthy male Wistar rats (n=14) were stereotactically inoculated in the right hemisphere with  $1.0 \times 10^5$  C6 glioma cells (American Type Tissue Collection, ATTC). Prior to imaging, all rats were affixed with venous and arterial catheters.

### **MR Imaging**

MRI was used to localize C6 tumors. Rats were secured in a prone position in a 38-mm inner diameter radiofrequency coil and placed in a Varian 4.7T horizontal bore imaging system (Varian Inc.). A constant body temperature of 37 °C was maintained using heated airflow. An initial multislice gradient echo imaging sequence [repetition time (TR) = 150 ms; echo time (TE) = 3.5 ms; 128 x 128 matrix, 40 x 40 mm<sup>2</sup> FOV; 2-mm slice thickness] was used to acquire seven slices in each imaging plane (axial, coronal, sagittal) for proper positioning of subsequent scans. A multislice T<sub>2</sub>-weighted fast-spin echo scan with eight echoes and 8.0 ms echo spacing (effective echo time of 32 ms) was then collected with TR = 2000 ms, 32 x 32 mm<sup>2</sup> FOV, 128 x 128 matrix, number of acquisitions = 16, and eight coronal slices of 2 mm thickness.

## **PET/CT Imaging**

PET/CT imaging was performed within 24 h of MR imaging in rats with confirmed tumors (n=14). Tumor-bearing rats were administered 130 – 200 MBq/0.2 mL [<sup>18</sup>F]DPA-714 via a jugular catheter while in a microPET Focus 220 (Siemens). Data were collected in list-mode format for 90 min, followed by a CT (microCAT II, Siemens) for attenuation correction. For displacement studies (n=4), DPA-714 (10 mg/kg) was injected at 30 min via jugular catheter.

The dynamic PET acquisition was divided into twelve, ten-second frames for the first two min, three, sixty-second frames for the following three minutes, followed by seventeen, three-hundred second frames for the duration of the scan. The raw data within each frame was then binned into 3D sinograms with a span of three and ring difference of 47. The sinograms were reconstructed into tomographic images (128 x 128 x 95) with voxel sizes of 0.095 x 0.095 x 0.08 cm<sup>3</sup>, after applying scatter and attenuation corrections, using an ordered-subsets expectation-maximization (OS-EM 2D) algorithm with 16 subsets and four iterations. Attenuation correction was accomplished by generating an attenuation map from the CT image. The CT image was first co-registered with the microPET image, segmented, and then projected into sinogram space with a span of 47 and ring difference of 23.

## **Measurement of [<sup>18</sup>F]DPA-714 in Plasma**

Immediately following administration of [<sup>18</sup>F]DPA-714, arterial blood samples (50 µL) were collected at 10-s intervals during the first minute of scanning,

followed by collection at 90 s, and 2, 8, 12, 20, 30, 45, 60, 75, and 90 min. Blood samples (50  $\mu$ L) were centrifuged at 14,000 RPM for 5 min in a microcentrifuge. The plasma (15  $\mu$ L) was then removed and the radioactivity measured in a NaI well counter (Capintec).

### **HPLC Radiometabolite Analysis**

Briefly, arterial blood (200  $\mu$ L) was collected at 2, 12, 30, 60, and 90 min. Following centrifugation, plasma was extracted with acetonitrile:water (340  $\mu$ L, 7:1, v/v). The mixture was centrifuged and the supernatant used for reversed phase HPLC analysis using 0.1 M aqueous ammonium acetate ( $\text{NH}_4$ )OAc (pH 10) and acetonitrile (30:70; v/v) at 1.0 mL/min on a C18 Dynamax 250 x 4.6 mm (Varian) column. Radiochromatographic data were recorded and collected using a radioisotope detector (Bioscan), decay-corrected to time zero of each radiochromatogram, and smoothed using a locally weighted scatter plot smoothing method.<sup>58</sup> The plasma time-activity curve was corrected according to the fraction of unchanged radioligand.

### **Histology**

Whole brains were harvested and fixed in 4% formalin for 48 h, followed by paraffin embedding for immunohistochemistry (IHC). Tissue sections of 5.0- $\mu$ m thickness were taken and TSPO immunoreactivity assessed using a TSPO-specific rabbit polyclonal antibody, a gift from Professor V. Papadopoulos of McGill University, Montreal, Canada. Immunoreactivity was assessed using an



HRP Detection Kit (Dako). Hematoxylin and eosin (H&E) staining was used to quantify cell density and tumor localization. For histology quantification, optical density measurements of multi-spectral image cubes were collected using a CRI Nuance camera and the total intensity of positive pixels was determined as reported previously.<sup>35</sup>

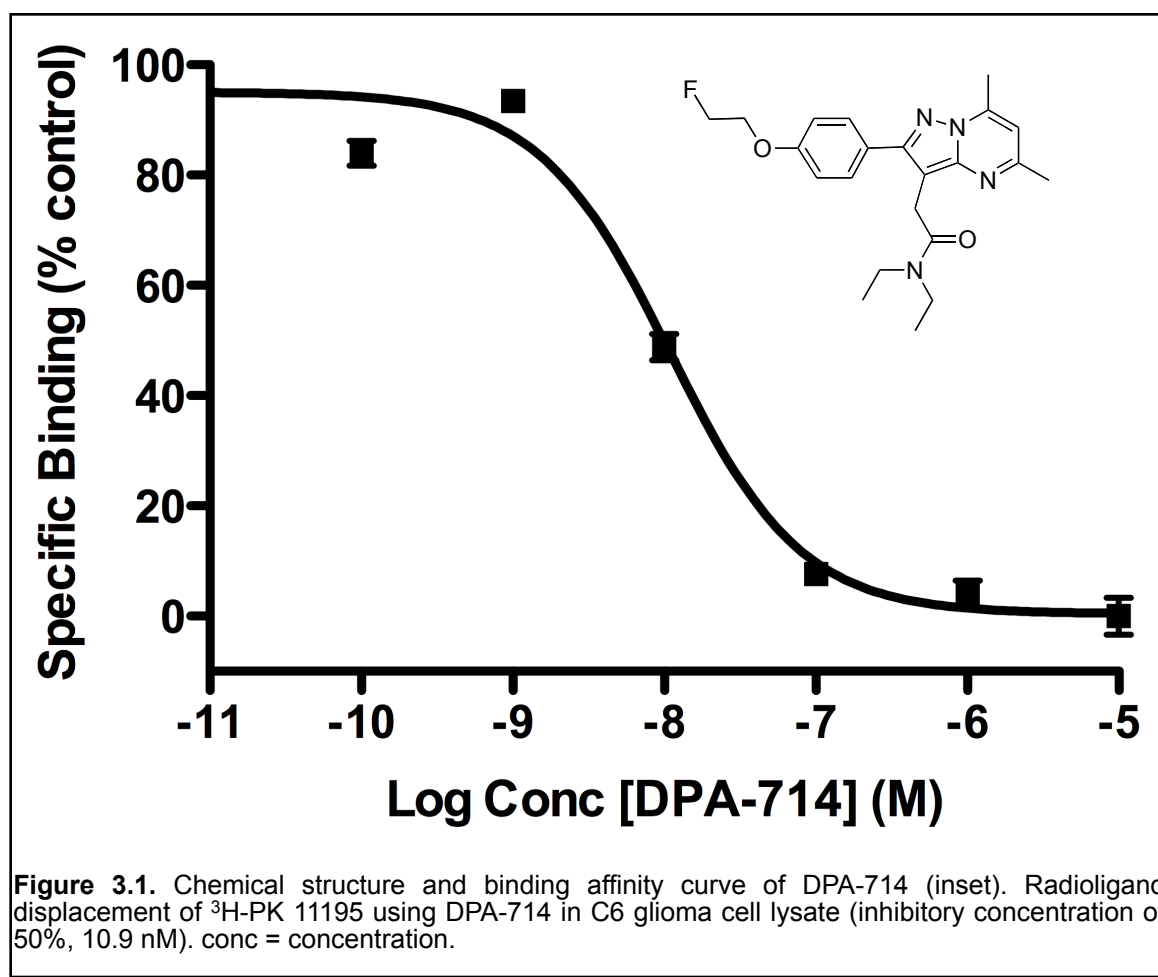
### **Image Analysis and Modeling**

Time-activity curves (TACs) were generated by manually drawing three-dimensional volumes of interest over tumor and contralateral brain using ASIPro (Siemens). The arterial input function (AIF) was computed from plasma sampling during imaging and corrected for metabolism of the parent ligand. Of the fourteen animals imaged in this study, data collected from three animals were excluded from modeling due to insufficient collection of arterial blood required for AIF determination. Both a 2-compartment, 2-rate constant kinetic model and a 3-compartment, 4-rate constant kinetic model were used to characterize [<sup>18</sup>F] DPA-714 pharmacokinetics with COMKAT software package. Model fit was determined by inspection. In the 2-compartment, 2-rate constant kinetic model, we determined model parameters for the influx ( $K_1$ ) and efflux ( $k_2$ ) rate constants of the radioligand diffusion between the plasma and tissue compartments. In the 3-compartment, 4-rate constant kinetic model, we determined model parameters for influx ( $K_1$ ) and efflux ( $k_2$ ) and exchange constants between specific binding ( $k_3$ ) and free ligand (including non-specific binding) ( $k_4$ ) compartments for both normal brain tissue and tumor. For the 3-compartment, 4-rate constant kinetic

model, the total volume of distribution ( $V_T$ ) was then calculated using the equation  $V_T = (K_1/k_2)(1+k_3/k_4)$  for the whole brain (excluding tumor) and for the tumor.<sup>59</sup> Additionally, using the first 60 minutes of data (beyond which, tracer was undetectable in blood), a graphical analysis method<sup>60</sup> was used to estimate the total distribution volume for the whole brain (excluding tumor) and tumor. Analysis of statistical significance utilized the Student's T-test (Prism 4.0).

### 3.4 Results

#### Specific Binding of DPA-714 to TSPO in C6 Glioma Cell Line Homogenates.



Previous studies explored [<sup>18</sup>F]DPA-714 within the context of neuroinflammation.<sup>46, 57</sup> Our interest in assaying TSPO expression in glioma led us to evaluate the specific binding of DPA-714 in glioma cell line homogenates (**Fig. 3.1**). We found DPA-714 to be highly specific for TSPO, exhibiting robust concentration dependent displacement of the isoquinoline carboxamide [<sup>3</sup>H]PK 11195 to near-background levels. Non-linear regression analysis of the binding data yielded an IC<sub>50</sub> for DPA-714 of approximately 10.9 nM, similar to our previous observations with the aryloxyanilide PBR06.<sup>35</sup>

#### ***In Vivo* Uptake of [<sup>18</sup>F]DPA-714 in C6 Glioma.**

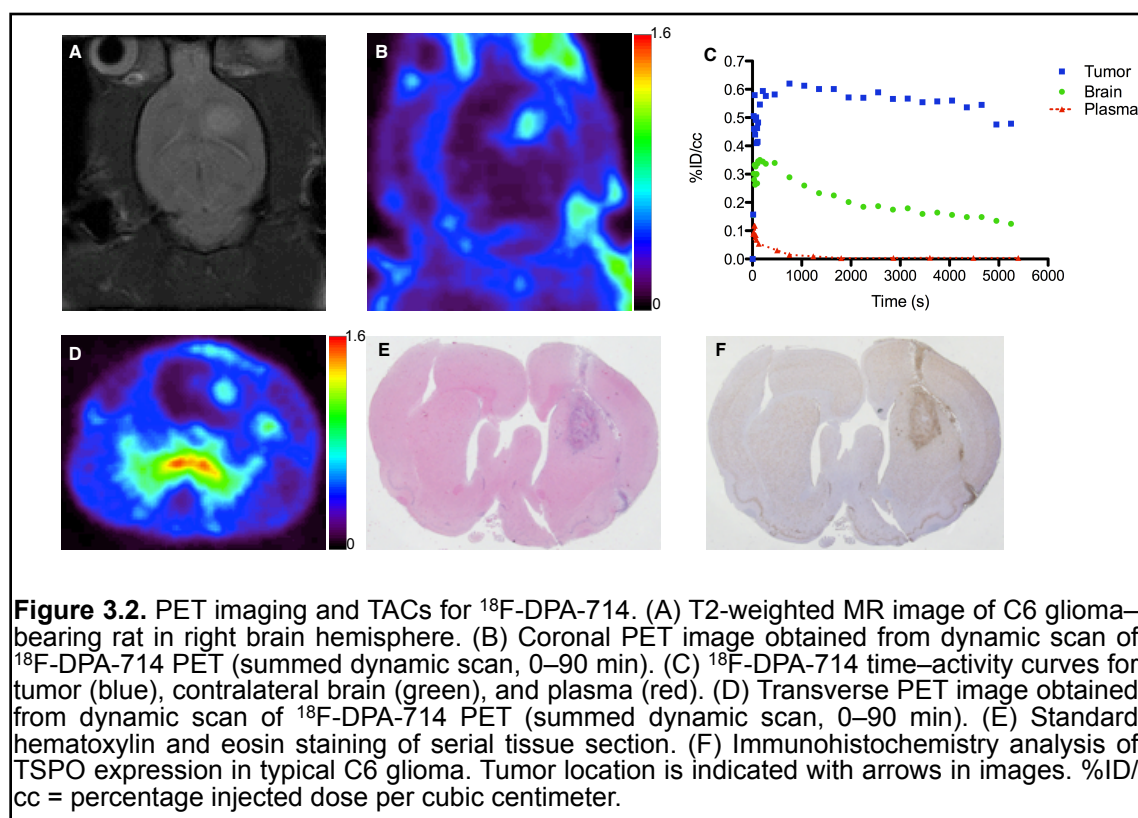
Prior to PET imaging with [<sup>18</sup>F]DPA-714, brain tumors were localized using T<sub>2</sub>-weighted MRI. Similar to previous observations, C6 tumors exhibited marked hyperintensity indicative of longer T<sub>2</sub> relaxation times compared to surrounding brain (**Fig. 3.2A**). Dynamic PET imaging of [<sup>18</sup>F]DPA-714 illustrated that the majority of the uptake in the brain was localized to tumor tissue, with only modest accumulation in adjacent, normal areas of the brain (**Fig. 3.2B, 3.2D**). Over the last 30 min of the PET scan, total radioactivity levels in tumor tissue were approximately four-fold higher than normal brain. Over the course of imaging, a modest level of radioactivity localized to the skull, indicating defluorination that was later confirmed by HPLC radiometabolite analysis (**Table 3.1**). Accumulation of [<sup>18</sup>F]DPA-714 was observed in the olfactory epithelium and Harderian glands, which had little impact on brain tumor imaging. **Figure 3.2C** illustrates a typical TAC for tumor, normal brain, and plasma activity for a typical 90 minute scan. We

**Table 3.1.** HPLC Radiometabolite Analysis of [<sup>18</sup>F]DPA-714 (mean ± SD).

P.I. Time <sup>1</sup>	% [ <sup>18</sup> F]DPA-714	% <sup>18</sup> F-	% Metabolite
2 (N=7)	95 ± 6.0	2 ± 3.3	3 ± 3.7
12 (N=7)	68 ± 7.4	13 ± 6.7	19 ± 5.8
30 (N=7)	44 ± 8.9	37 ± 5.4	19 ± 8.8
60 (N=7)	27 ± 6.2	50 ± 15.0	23 ± 7.3
90 (N=5)	22 ± 17.8	64 ± 12.1	14 ± 3.8

1. P.I. abbreviation for Post Injection.

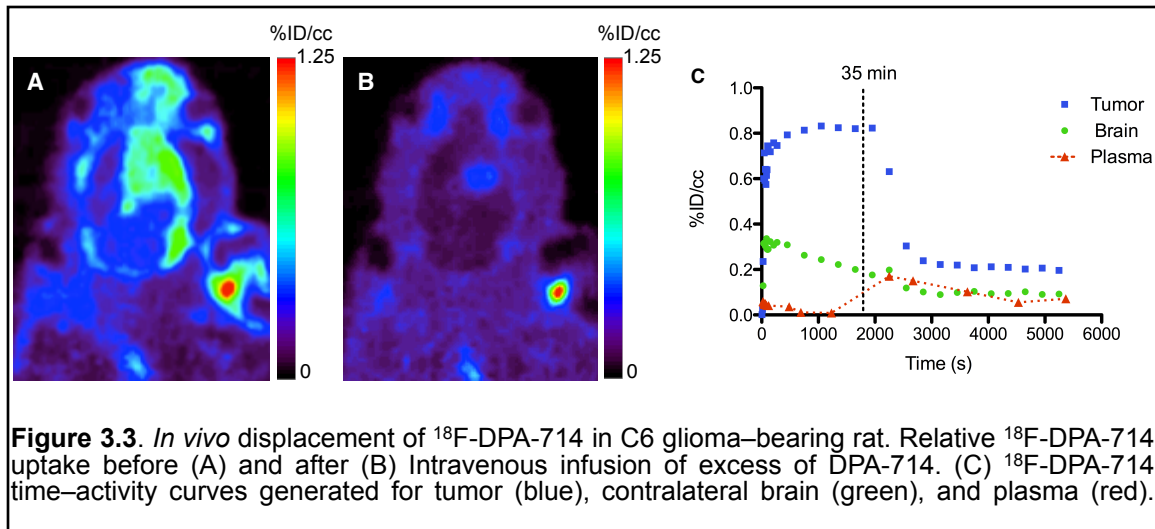
found that [<sup>18</sup>F]DPA-714 washed into both normal brain and tumor tissue rapidly, but washout from tumor tissue was much slower compared to normal brain. Following the initial spike in plasma activity consistent with tracer injection, [<sup>18</sup>F]



DPA-714 rapidly cleared the plasma. Imaging-matched brains were processed for staining and IHC. Using standard H&E staining to localize the tumor (**Fig. 3.2E**), we found that TSPO immunoreactivity was significantly higher in the tumor than in normal brain (**Fig. 3.2F**). Consistent with previous studies of TSPO expression in glioma, TSPO protein levels measured by IHC optical density were three- to four-fold higher in tumor relative to normal brain tissue.<sup>14, 35</sup> Overall, we found excellent agreement between [<sup>18</sup>F]DPA-714 accumulation and TSPO protein levels as measured by IHC.

#### ***In vivo* Displacement of [<sup>18</sup>F]DPA-714.**

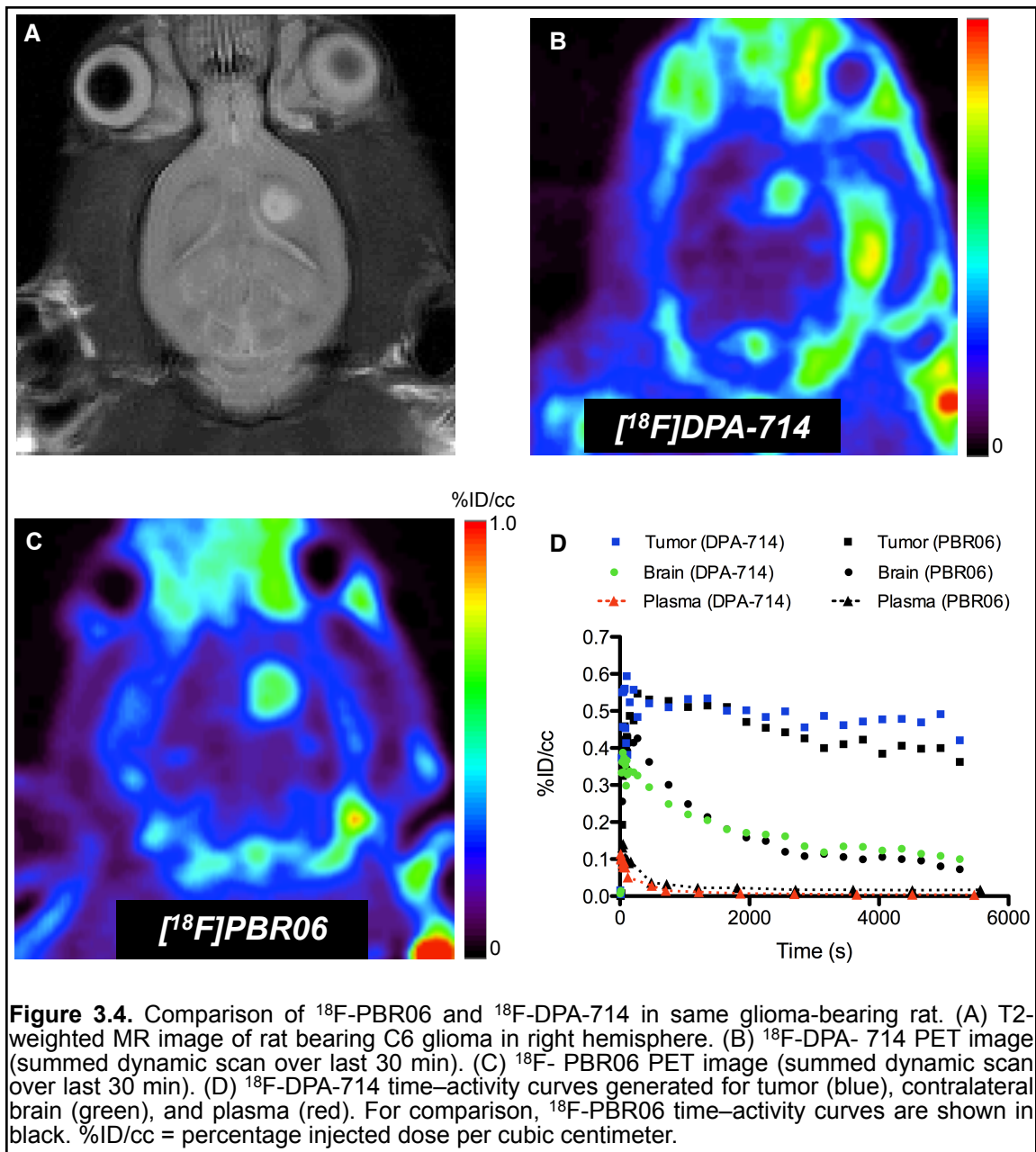
To evaluate the *in vivo* TSPO specificity of [<sup>18</sup>F]DPA-714, we carried out displacement studies in C6-bearing rats using DPA-714. During the dynamic PET study, excess (10 mg/kg) DPA-714 was administered intravenously 30 minutes following injection of [<sup>18</sup>F]DPA-714. Summation of the first 30 minutes of the PET scan prior to injection of DPA-714 (0 – 30 min) demonstrated typical uptake characteristics of [<sup>18</sup>F]DPA-714 (**Fig. 3.3A**). However, summation of the final 30 minutes of the PET scan (60 – 90 min) demonstrated significant displacement of [<sup>18</sup>F]DPA-714 in normal brain and tumor tissue (**Fig. 3.3B**). Accordingly, TAC analysis (**Fig. 3.3C**) demonstrated that following injection of DPA-714, tumor activity was reduced approximately 75% compared to the peak tumor uptake in the animal shown. Over multiple animals with comparatively larger and smaller tumors (n = 4), we observed a mean displacement of peak uptake of greater than 60%. Interestingly, in heterogeneous tumors featuring



central necrosis, tracer uptake and specificity appeared greatest in actively proliferating tumor regions. Furthermore, minor, non-displaceable pooling of [ $^{18}\text{F}$ ]DPA-714 was observed in regions of central necrosis, although levels pooling in these regions tended to be reduced or similar to uptake associated normal, healthy brain.

### Direct Comparison of [ $^{18}\text{F}$ ]DPA-714 and [ $^{18}\text{F}$ ]PBR06.

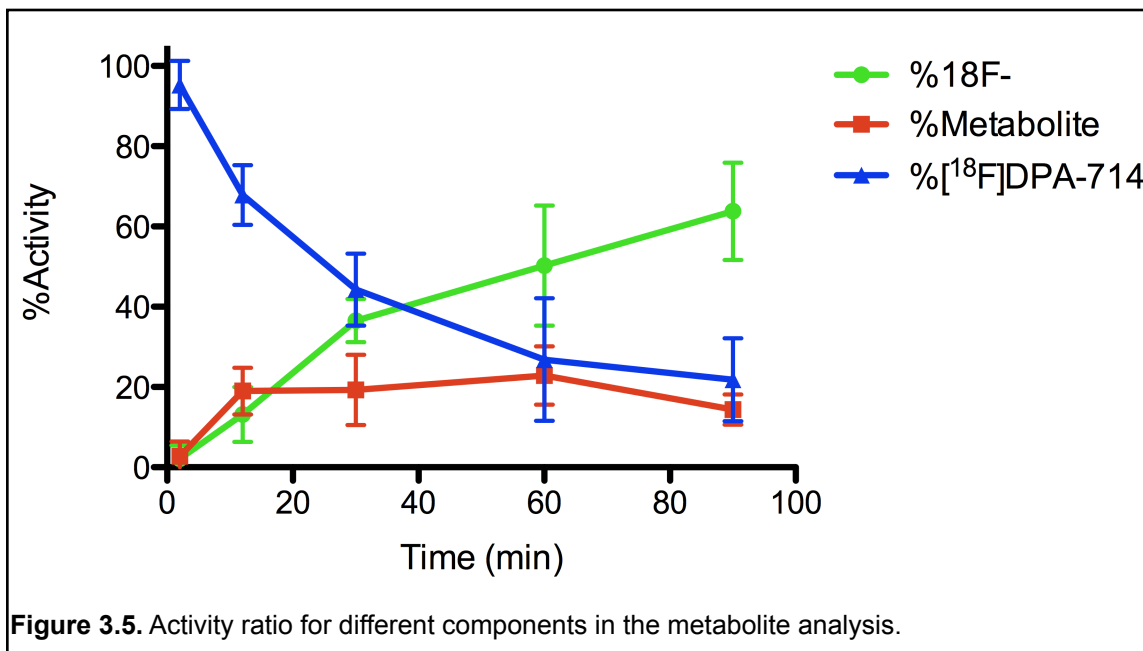
To further evaluate the *in vivo* performance of [ $^{18}\text{F}$ ]DPA-714 in tumor studies, we directly compared the localization and relative tissue uptake of this tracer in C6 glioma-bearing cohorts (n=2) to an aryloxyanilide TSPO PET ligand [ $^{18}\text{F}$ ]PBR06. A representative study is shown in **Fig. 3.4**. Tumors were initially localized with T<sub>2</sub>-weighted MRI (**Fig. 3.4A**). Subsequently, serial dynamic PET imaging studies utilizing [ $^{18}\text{F}$ ]PBR06 (**Fig. 3.4B**) or [ $^{18}\text{F}$ ]DPA-714 (**Fig. 3.4C**) were carried out approximately 24 hours apart. As shown in **Fig. 3.4**, both tracers exhibited similar localization to tumor tissue, with only modest retention in the normal brain. Both



tracers exhibited similar rapid clearance from plasma and normal brain. However, TAC analysis illustrated that  $^{18}\text{F}$ -DPA-714 was retained in tumor tissue to a somewhat greater extent than  $^{18}\text{F}$ -PBR06, which manifested as a modestly higher signal-to-noise ratio (tumor/normal) for  $^{18}\text{F}$ -DPA-714 over the last 30 minutes of the PET scan.

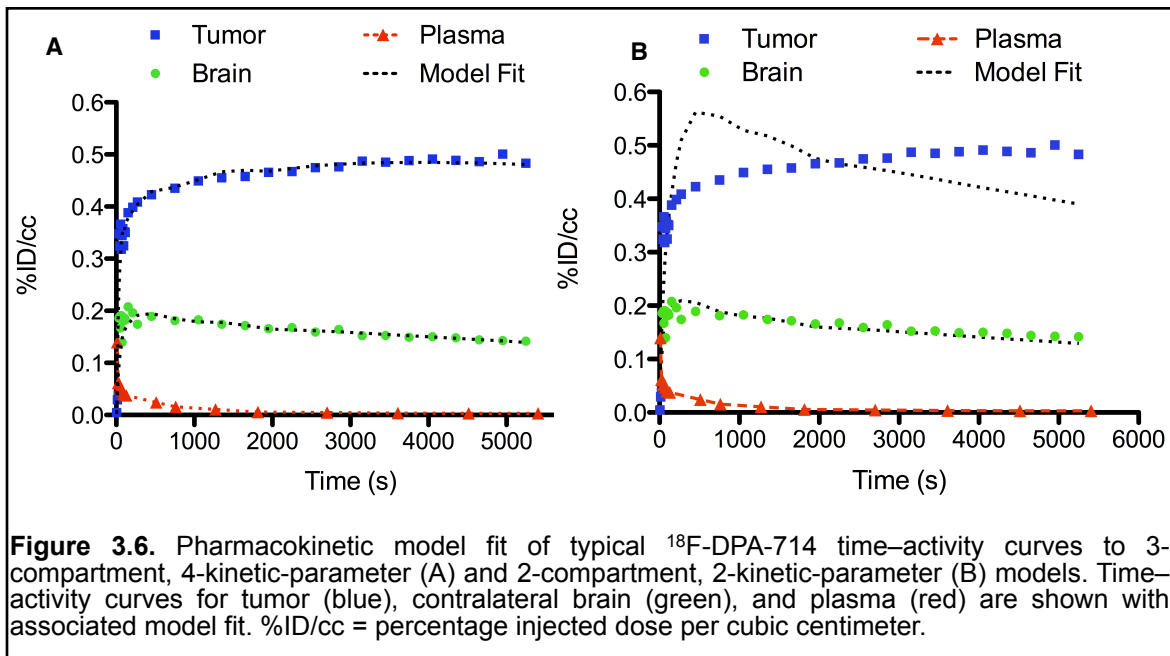
### Characterization of [<sup>18</sup>F]DPA-714 Radiometabolites.

Detectable [<sup>18</sup>F]DPA-714 radiometabolites included free [<sup>18</sup>F]fluoride (retention time 2.5 min) and a single radiometabolite more hydrophilic than DPA-714



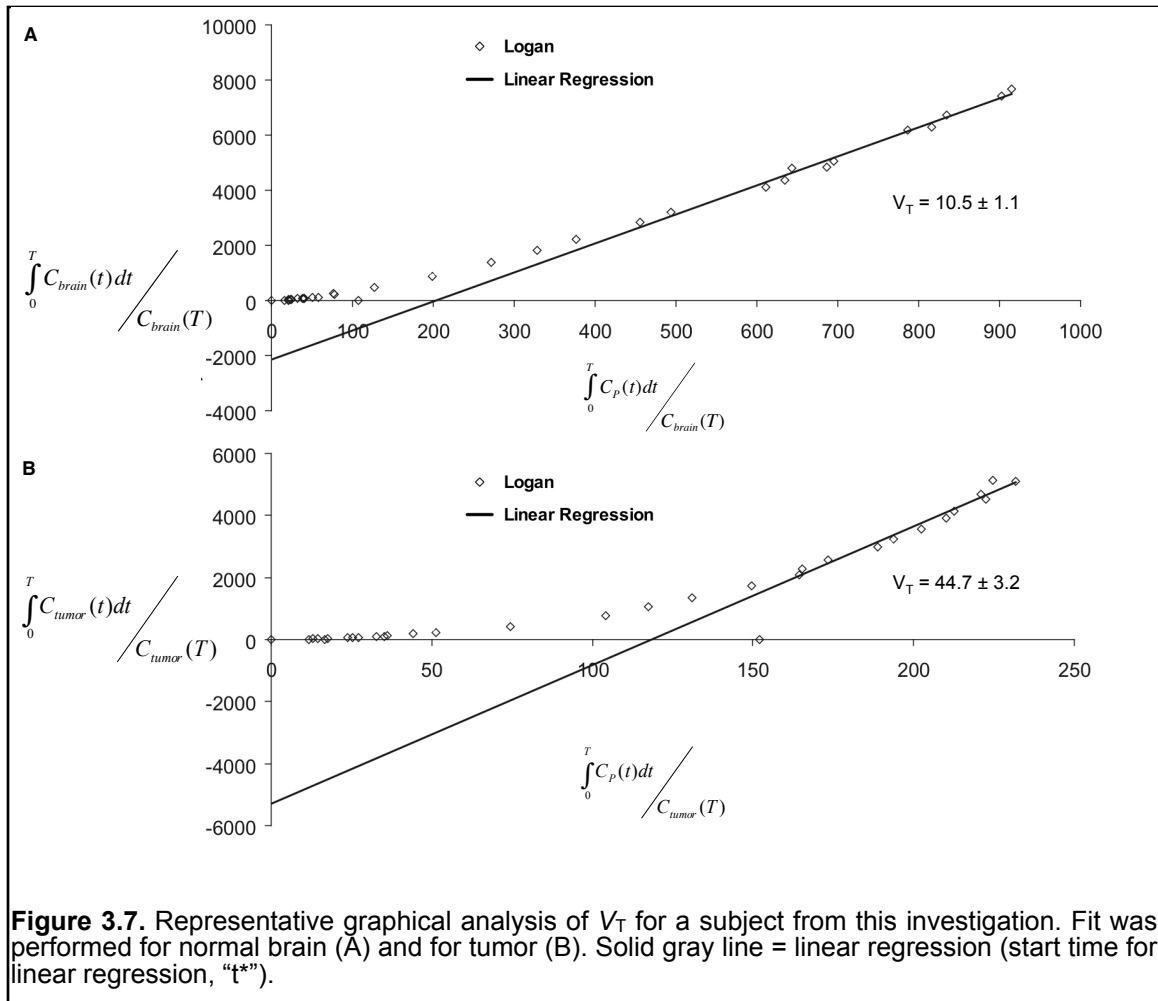
(retention time, 4.0 min; parent tracer retention time, 5.0 min). As shown in **Table 3.1**, immediately following intravenous injection of [<sup>18</sup>F]DPA-714, the parent tracer accounted for approximately 95% of the whole plasma radioactivity. Subsequently, we observed a steady decrease of parent ligand in the plasma that was roughly equivalent to the increase in free <sup>18</sup>F-fluoride over the course of a given imaging study (**Figure 3.5**), suggesting the primary metabolism observed in these studies was defluorination. Levels of the observed hydrophilic radiometabolite were relatively constant beyond the first 10 minutes of the scan, suggesting that appearance of this species was offset by further metabolism and/or subsequent clearance.





### Compartmental Modeling

To describe the pharmacokinetics of  $^{18}\text{F}$ -DPA-714, we evaluated 2-compartment, 2-kinetic parameter and 3-compartment, 4-kinetic parameter models. As determined by inspection, fit of the  $^{18}\text{F}$ -DPA-714 PET data was superior in the 3-compartment, 4-kinetic parameter model and the 2-compartment model was not considered further (**Fig. 3.6A** and **3.6B**). Utilizing the 3-compartment, 4-kinetic parameter model and the metabolite-corrected AIF,  $K_1/k_2$  and  $k_3/k_4$  were determined for tumor tissue and normal brain (**Table 3.2**). Compared with normal brain, tumor tissues tended to exhibit a higher  $K_1/k_2$  and  $k_3/k_4$ . Estimation of  $V_T$  derived from kinetic parameters and graphical estimation (**Fig. 3.7**) was performed both in brain and tumor. Ratios of  $V_T$  and %ID/cc between tumor and brain obtained from both methods of estimation were highly



similar and yielded statistically significant values that closely mirrored TSPO expression as measured by immunohistochemistry (**Table 3.2**).

### 3.5 Discussion

A considerable body of research suggests that TSPO can serve as an important biomarker in oncology. Numerous preclinical and clinical studies have demonstrated prognostic implications associated with elevated TSPO expression in multiple tumor types, including the breast,<sup>10, 11</sup> prostate,<sup>9</sup> oral cavity,<sup>53</sup> colon,<sup>6, 7,</sup>

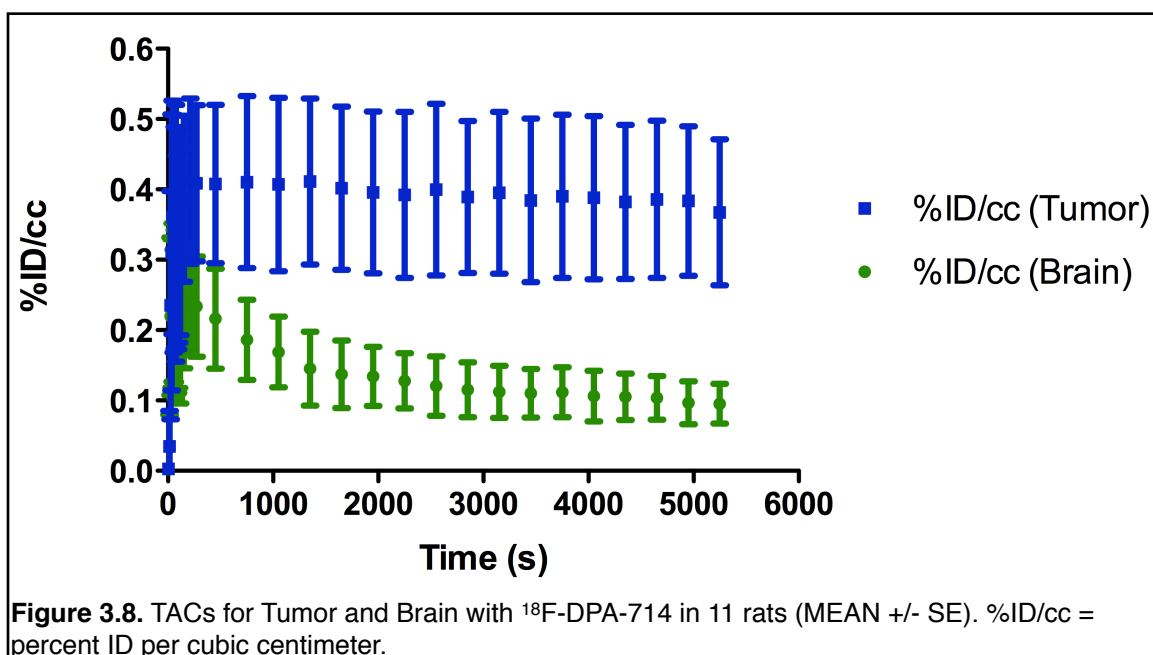
<b>Table 3.2.</b> Parameter Estimations for [ <sup>18</sup> F]DPA-714 Uptake ( <i>mean ± SEM</i> ).				
	$K_1/k_2$ (mL/g)	$k_3/k_4$	$V_T$ (mL/g) <sup>†</sup>	$V_T$ (mL/g) <sup>‡</sup>
Tumor (N=11)	6.867 ± 1.226	8.913 ± 1.155	70.033 ± 14.729	57.440 ± 11.742
Brain (N=11)	3.619 ± 0.551	4.024 ± 0.842	15.963 ± 3.566	14.570 ± 2.823
P value	0.0762	0.0021	0.0017	0.0029
From kinetic parameters <sup>†</sup> .				
From graphical analysis <sup>‡</sup> .				

<sup>20</sup> liver,<sup>15</sup> and brain.<sup>14, 54</sup> The first evidence supporting the hypothesis that TSPO ligands could be used for detection and grading of human brain tumors emerged more than twenty years ago,<sup>14, 28, 29</sup> where autoradiographical ([<sup>3</sup>H]PK 11195) and PET ([<sup>11</sup>C]PK 11195) studies evaluated TSPO expression in experimental models of glioma, post-mortem human brain section<sup>14, 29, 34, 54</sup> and patients with glioma.<sup>33</sup> While these early studies established the potential utility of TSPO ligands for brain tumor imaging, the most prominent TSPO-selective ligand available at the time, PK 11195, suffered from relatively modest *in vivo* uptake and attendant contrast in tumor tissue compared to normal brain. Furthermore, PK 11195 previously demonstrated considerable levels of non-displaceable ligand binding *in vivo*.<sup>33</sup> Both of these conditions led to ligand uptake that marginally reflected actual TSPO expression levels. These issues recently led us to explore novel

TSPO ligands with potentially improved pharmacokinetic properties and *in vivo* specificity in cancer imaging studies.

For example, we recently reported the first preclinical utilization of an aryloxyanilide-based TSPO ligand, [<sup>18</sup>F]PBR06, for quantitative assessment of TSPO expression in glioma.<sup>35</sup> These studies demonstrated that [<sup>18</sup>F]PBR06 is a highly promising tracer for visualization of brain tumors, as well as quantification of TSPO expression in tumor and surrounding normal tissue. Compared with previous reports using [<sup>11</sup>C]PK 11195 in brain tumors, [<sup>18</sup>F]PBR06 demonstrated superior TSPO specificity *in vivo*, resulting in close agreement between tracer accumulation and TSPO protein levels.

In this study, we evaluated the pyrazolopyrimidine [<sup>18</sup>F]DPA-714 in analogous preclinical studies. Like [<sup>18</sup>F]PBR06, [<sup>18</sup>F]DPA-714 exhibited uptake that closely mirrored TSPO expression in tumor and normal tissues. Indeed, both tracers exhibited similar accumulation and clearance when compared in the same glioma-bearing animals. Furthermore, [<sup>18</sup>F]DPA-714 was highly displaceable from normal and tumor tissues. We observed a modest degree of non-displaceable pooling of [<sup>18</sup>F]DPA-714 in regions of the tumor that appeared to correlate with central necrosis, although uptake in necrosis was significantly lower than that observed in actively growing portions of the tumor. Analogous to our studies with [<sup>18</sup>F]PBR06, [<sup>18</sup>F]DPA-714 time-activity curves derived from tumor and normal brain could be fit to a 3-compartment, 4-kinetic parameter compartmental model, enabling tracer quantitation (e.g.  $V_T$ ) in tumor tissue and normal brain. In general, TACs for [<sup>18</sup>F]DPA-714 uptake in both tumor and normal



tissue were remarkably consistent across numerous animals (**Figure 3.8**), suggesting the robustness and reproducibility of this imaging approach. Though the aryloxyanilide  $^{18}\text{F}$ PBR06 and pyrazolopyrimidine  $^{18}\text{F}$ DPA-714 both appear to be promising tracers in this preclinical setting, further studies to better characterize determinants such as *in vivo* metabolism and tissue pharmacodynamics will likely reveal important differences between these two unique scaffolds. We envision that evaluation of these and similar agents within the context of other solid tumors such as colorectal<sup>6, 7, 20</sup> and breast<sup>10, 11</sup> cancer may shed further light upon the rational selection of TSPO ligands for cancer imaging.

### 3.6 Conclusion

These preclinical studies illustrate the feasibility of using  $^{18}\text{F}$ DPA-714 for visualization of TSPO-expressing brain tumors. Importantly,  $^{18}\text{F}$ DPA-714

appears suitable for quantitative assay of tumor TSPO levels in vivo. Given the relationship between elevated TSPO levels and poor outcome in oncology, these studies suggest the potential of [<sup>18</sup>F]DPA-714 PET to serve as a novel predictive cancer imaging modality.

## CHAPTER 4

### AN EFFICIENT STRATEGY TO GENERATE PYRAZOLOPRIMIDINE LIBRARIES: POTENTIAL MOLECULAR IMAGING LIGANDS FOR TRANSLOCATOR PROTEIN

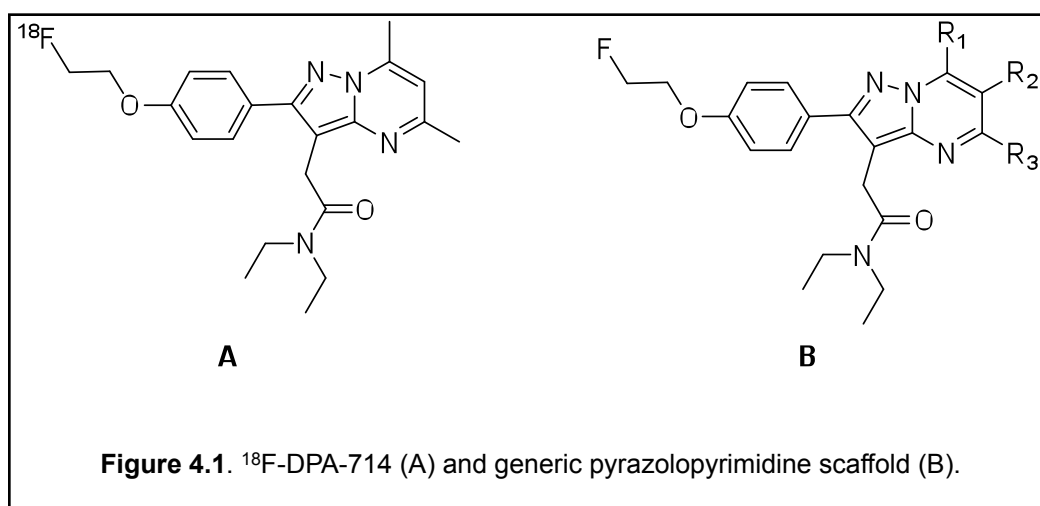
#### 4.1 Abstract

A novel and highly efficient approach for generating libraries of structurally diverse 5,6,7-substituted pyrazolopyrimidines containing a 2-fluoroethoxy prosthesis is reported. Pyrazolopyrimidines are an important class of small-molecule ligands of the translocator protein (TSPO). The reported methodology allows facile preparation and subsequent optimization of candidate TSPO ligands, thereby accelerating discovery and prioritization of novel compounds for molecular imaging with positron emission tomography (PET) and potential therapeutic leads.

#### 4.2 Introduction

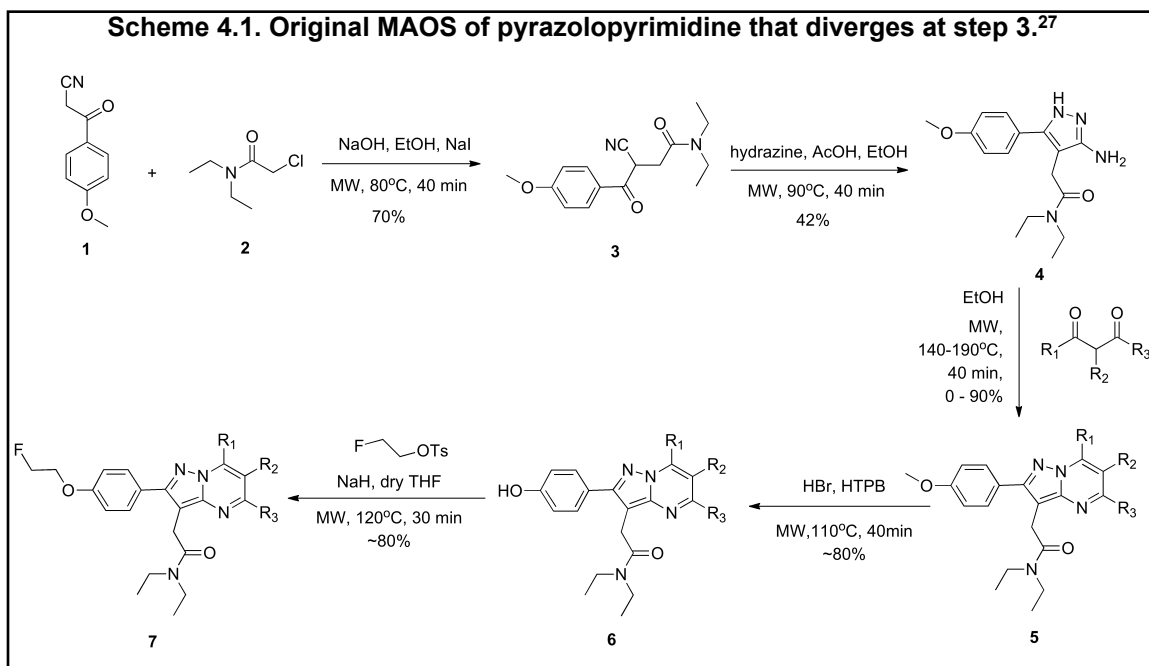
Translocator protein (TSPO) is an 18 kDa outer-mitochondria membrane protein involved in a variety of cellular processes, including steroid hormone synthesis, cholesterol metabolism, proliferation, and apoptosis<sup>1</sup>. In healthy tissue, TSPO expression is primarily confined to steroid-producing tissues. Elevated TSPO expression is also observed in a variety of disease states, including neuroinflammation<sup>1, 2, 61</sup> and cancer.<sup>6, 7, 9-11, 15, 20, 53, 54</sup> In cancer, TSPO expression appears to be a prognostic indicator, where elevated levels correlate with tumor aggressiveness and metastasis.<sup>5, 20, 53, 55</sup> For this reason, non-invasive imaging

measures of TSPO levels may form the basis of important cancer imaging.<sup>35</sup> Recently, TSPO-targeted molecular imaging probes have been developed and radiolabeled with carbon-11/<sup>11</sup>C and fluorine-18/<sup>18</sup>F for positron emission tomography (PET).<sup>18, 57, 62, 63</sup> One such compound, <sup>18</sup>F-DPA-714 (N,N-diethyl-2-(2-(4-(2-[<sup>18</sup>F])fluoroethoxy)phenyl)-5,7-dimethylpyrazolo[1,5-a]pyrimidin-3-yl)acetamide) (**Figure 4.1A**), is a high-affinity TSPO PET ligand based upon the



pyrazolopyrimidine scaffold that was first reported by James et al. for PET imaging of neuroinflammation.<sup>36</sup> Recently, our laboratory was the first to report utilization of this agent to quantify TSPO levels in cancer.<sup>37</sup> These efforts lead to an optimized total synthesis of DPA-714 and similar compounds through strategic application of microwave-assisted organic synthesis (MAOS).<sup>27</sup> That strategy dramatically reduced overall reaction time with nominal effects upon yield (**Scheme 4.1**).<sup>27</sup> However, to date there have been no reports of broadly applicable methods that facilitate rapid assembly of libraries of novel pyrazolopyrimidines, where target compounds directly mimic their analogous <sup>18</sup>F-





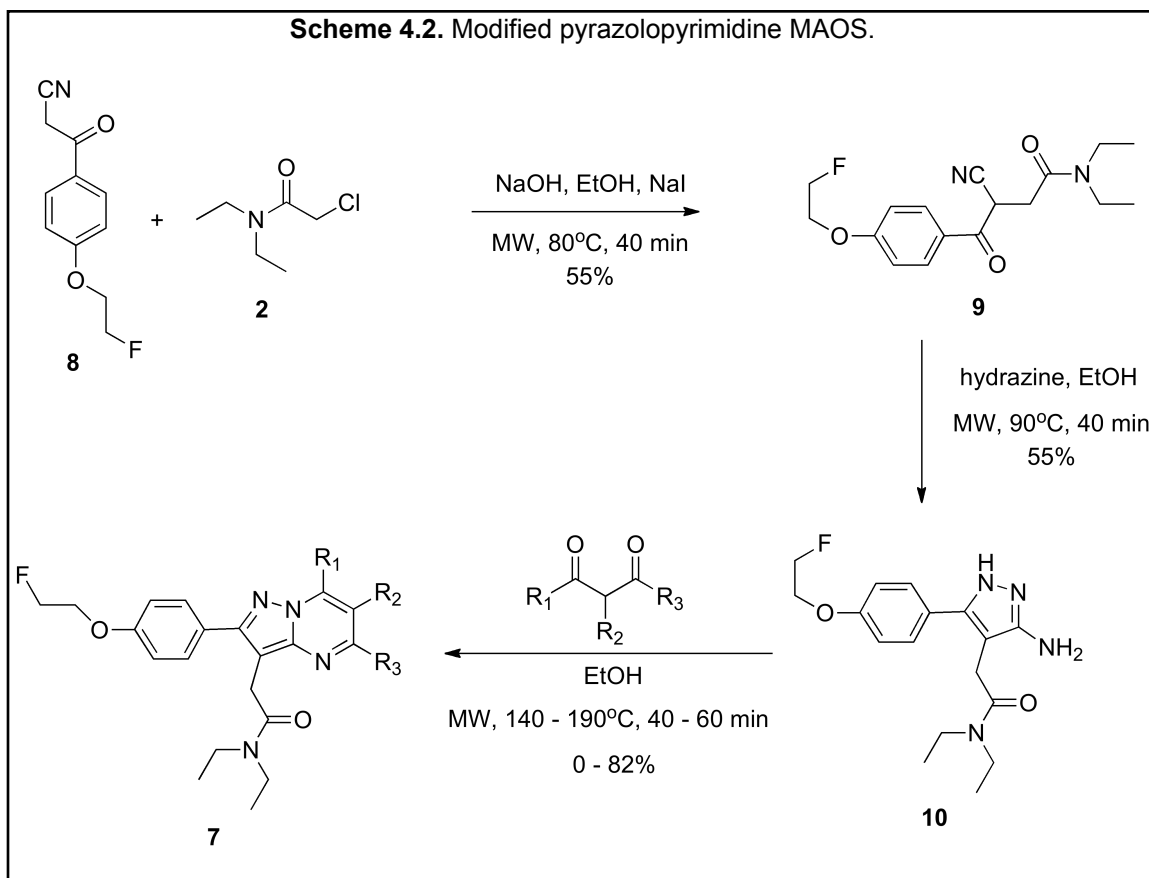
based PET counterparts, thus saving considerable time in future optimization of potential imaging leads.

### 4.3 Results and Discussion

The new synthetic strategy reported herein (**Scheme 4.2**) fills this void and was inspired by our earlier MAOS approach (**Scheme 4.1**). In this method, our primary aim was to incorporate diversity at the 7- $R_1$ , 6- $R_2$ , and 5- $R_3$  positions on the pyrazolopyrimidine scaffold (**Figure 4.1B**), while maintaining the 4-methoxy and 4-(2-fluoroethoxy) imaging prostheses on the pendant phenyl ring. Previously, the key 3-amino-1H-pyrazole core (**4**) was prepared in two steps and chosen as a point of divergence. Treatment of **4** with a variety of structurally diverse diones, followed by selective demethylation and final coupling, generated a focused library of pyrazolopyrimidines featuring potentially unique  $R_1$ ,  $R_2$ , and  $R_3$  groups. Using this method, DPA-714 and four analogs thereof were

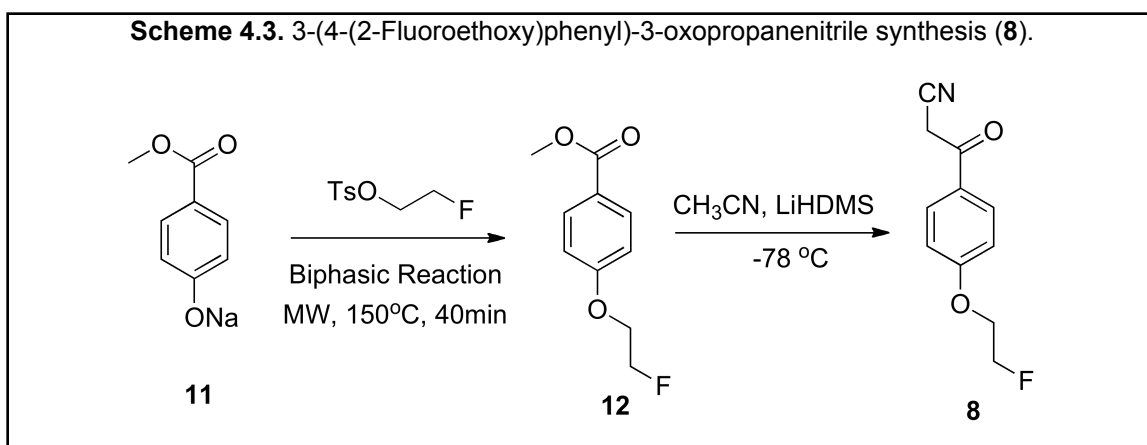
synthesized with overall reaction times reduced from days to three hours when compared with previously published methods.<sup>27</sup> While effective towards preparation of a focused group of analogs, this method was cumbersome when applied to library/high-throughput synthesis of pyrazolopyrimidines because the point of divergence was three steps removed from the final compound.

To address these shortcomings, we developed the modified approach



reported here which diverges at the final step (**Scheme 4.2**). Importantly, the method reported here enables parallel synthesis of analogs that faithfully recapitulate the structure of the analogous PET agent. This seemingly minor alteration from our previous strategy significantly reduces time required for subsequent lead optimization and vetting of prospective screening hits. Our first

step towards this goal was to install the 2-fluoroethoxy prosthesis at the 4-position of the phenyl group prior to synthetic divergence, in effect, making the final step of the original synthesis the first step in the new synthesis. This ostensibly required preparation of novel compound **8**, which was possible via a two-step sequence (**Scheme 4.3**). Of these two reactions, the first is a biphasic reaction of sodium 4-(methoxycarbonyl)phenolate (**11**) with 2-fluoroethyl tosylate, under microwave irradiation at 150 °C for 40 min to give **12** in a yield of 66%. The second features a substitution of the methoxy group of **12** with acetonitrile to form **8**, in the presence of LiHMDS at -78°C. In the following steps, **8** was then reacted with chloroacetamide **2** to give intermediate **9**, which was then subsequently treated with hydrazine to give **10** as the key precursor for the final diversification step (**Scheme 4.2**). For these transformations, we used the same conditions as those of our previously published MAOS method (**Scheme 4.1**) and



achieved comparable yields.

Compound **10** features the same 3-amino-1H-pyrazole core and 4-(2-fluoroethoxy) group on the phenyl ring as **4**. With **10** as the key precursor, we

successfully prepared a novel series of pyrazolopyrimidines by coupling with a variety of diones (**Table 4.1**). The final coupling reactions were achieved by microwave irradiation at temperatures ranging from 140-190°C and in less than one hour of reaction time. Yields for the conversion of **10** to **7** ranged from 8–82%, with entries **7i** and **7j** failing to produce any desired product. For the parent DPA-714 (entry **7a**), we achieved a modest yield (54%) using acetylacetone. Interestingly, we observed that R<sub>2</sub> substitution appeared to play a pivotal role in the dione condensation to give the final product (**7**). For example, we observed that substitution of hydrogen with chlorine at R<sub>2</sub> (entry **7d**, 82%) increased the yield dramatically. However, substitution of the same hydrogen with a methyl group, using 3-methyl-2,4-pentanedione (entry **7e**, 45%), resulted in comparable yields with **7a**. Diones bearing ethyl and acetyl groups at the R<sub>2</sub> position (entries **7e** and **7f**), however, suffered significantly decreased yields compared to **7a**. Furthermore, R<sub>1</sub> and R<sub>3</sub> substitution also affected cyclization yields. For example, in entry **7c**, coupling with hexafluoroacetylacetone furnished the corresponding product in 8% yield. We rationalize that this was due to the nascent electronegativity of the trifluoromethyl group.

Sterically bulky diones such as 2,6-dimethyl-3,5-heptanedione (entry **7h**), 2,2,6,6-tetramethyl-3,5-heptanedione (entry **7i**), and dibenzoylmethane (entry **7j**), were poorly reactive compared to entry **7a**, despite the use of higher temperatures and longer reaction times. We envision that the low yields obtained with these substituents stem from the geometric constraints given the added bulk at the R<sub>1</sub> and R<sub>3</sub> positions of these diones. Nevertheless, despite the variable

yields, when product was generated, the library method furnished entirely sufficient quantities of purified product for biological testing.

#### 4.4 Conclusion

In conclusion, we have developed a novel synthetic strategy to generate libraries of diverse pyrazolopyrimidines. This methodology leverages use of 3-(4-(2-fluoroethoxy)phenyl)-3-oxopropanenitrile (**8**) in the synthetic sequence, as well as the advantages inherent to MAOS, to reduce labor, time, and resources

Entry	Diones	R <sub>1</sub>	R <sub>2</sub>	R <sub>3</sub>	Temperature (°C)	Time <sup>26</sup>	Yield <sup>a</sup> (%)
7a	acetylacetone	-CH <sub>3</sub>	-H	-CH <sub>3</sub>	180	40	54
7b	3,5-heptanedione	-CH <sub>2</sub> CH <sub>3</sub>	-H	-CH <sub>2</sub> CH <sub>3</sub>	180	40	33
7c	hexafluoroacetylacetone	-CF <sub>3</sub>	-H	-CF <sub>3</sub>	190	60	8
7d	3-chloro-2,4-pentanedione	-CH <sub>3</sub>	-Cl	-CH <sub>3</sub>	180	40	82
7e	3-methyl-2,4-pentanedione	-CH <sub>3</sub>	-CH <sub>3</sub>	-CH <sub>3</sub>	180	40	45
7f	3-ethyl-2,4-pentanedione	-CH <sub>3</sub>	-CH <sub>2</sub> CH <sub>3</sub>	-CH <sub>3</sub>	180	40	17
7g	triacetyl methane	-CH <sub>3</sub>	-(C=O)CH <sub>3</sub>	-CH <sub>3</sub>	140	30	13
7h	2,6-dimethyl-3,5-heptanedione	-CH(CH <sub>3</sub> ) <sub>2</sub>	-H	-CH(CH <sub>3</sub> ) <sub>2</sub>	195	40	9
7i	2,2,6,6-tetramethyl-3,5-heptanedione	-C(CH <sub>3</sub> ) <sub>3</sub>	-H	-C(CH <sub>3</sub> ) <sub>3</sub>	195	60	0
7j	dibenzoyl methane	-Ph	-H	-Ph	195	60	0

a. Isolated yield.

required for library syntheses. Applying this approach, we synthesized a diverse and demonstrative library of pyrazolopyrimidines by introducing diones at the final, divergent step of the synthesis. In the case of TSPO ligand design, we anticipate this methodology will allow rapid exploration of structure-activity relationships at the 5-, 6-, and 7-positions, which may be important determinants of ligand binding.<sup>38, 64</sup> Thus, we envision this strategy will further the development

of novel PET probes for use in oncology and other TSPO-expressing diseases, as well as other potential therapeutic applications.

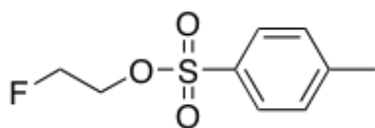
## 4.5 Results and Methods

### General Experimental.

All commercially available reagents were used without further purification. Reactions with microwave were carried out with a Biotage Initiator™ Sixty microwave system (Uppsala, Sweden) in the sealed vials. Reaction residues were purified by CombiFlash purification system (TELEDYNE ISCO) with silica cartridges. HPLC purification for the library was performed with Gilson preparative HPLC system (Gilson Inc., WI). <sup>1</sup>H- and <sup>13</sup>C-NMR spectra were recorded on a Bruker 400 MHz spectrometer in Vanderbilt Small Molecule NMR Facility Core. Chemical shifts were reported in ppm using the residual of chloroform as the internal standard (7.26 ppm for <sup>1</sup>H and 77.160 ppm for <sup>13</sup>C, respectively). Following abbreviations are used: s = singlet, d = doublet, t = triplet, q = quartet and m = multiplet. High resolution mass spectrum was performed with Waters Synapt hybrid quadrupole/oa-QT of mass spectrometer equipped with a dual channel ES-CI source.

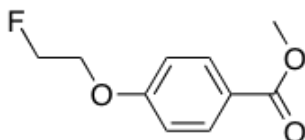
### General Procedure for Compound Synthesis

#### 2-fluoroethyl 4-methylbenzenesulfonate



To a solution of 2-fluoroethanol (2g, 31.22 mmol) in dry dichloromethane (40 mL) were successively added p-toluenesulfonyl chloride (8.93 g, 46.83 mmol), triethylamine (4.74 g, 46.83 mmol) and a catalytic amount of DMAP (0.38 g, 3.12 mmol). The reaction mixture was stirred at RT for 40 min. The reaction was monitored with LCMS. When completed, the reaction mixture was partitioned between 1M aqueous HCl (100mL) and dichloromethane (100mL × 2). Organic layer was collected and dried over MgSO<sub>4</sub>, filtered and evaporated to dryness. The residue was finally purified with flash chromatography on silica gel (hexanes/ethyl acetate = 9:1 (V/V)) to afford 5.1g 2-fluoroethyl 4-methylbenzenesulfonate as colorless oil. The yield is 75%. <sup>1</sup>H-NMR (CDCl<sub>3</sub>, 400 MHz) δ 7.82 (d, 2H, J = 8.2 Hz), 7.37 (d, 2H, J = 8.2 Hz), 4.64 (t, 1H, J = 4.2 Hz), 4.52 (t, 1H, J = 4.2 Hz), 4.30 (t, 1H, J = 4.0 Hz), 4.24 (t, 1H, J = 4.0 Hz), 2.46 (s, 3H). <sup>13</sup>C-NMR (CDCl<sub>3</sub>, 400 MHz) δ 145.1, 132.6, 129.9, 127.9, 81.3, 79.6, 68.5, 68.3, 21.6. HRMS calcd for C<sub>9</sub>H<sub>11</sub>FN<sub>3</sub>OS, m/z = 241.0311 [M+ Na]<sup>+</sup>, found 241.0311.

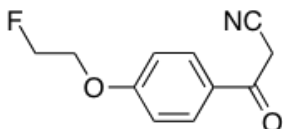
### Methyl 4-(2-fluoroethoxy)benzoate (12)



To a mixture of sodium 4-(methoxycarbonyl)phenolate (6.1g, 35.1 mmol) in 5 mL dichloromethane and 30 mL water were added 2-fluoroethyl 4-methylbenzenesulfonate (5.1g, 23.4 mmol) and a catalytic amount of hexadecyltrimethylammonium bromide (0.41g, 1.2 mmol). The reaction mixture

was then irradiated with microwave at 150°C for 40 min. Reaction was monitored with LCMS. When completed, the reaction mixture was washed with 100 mL water and then extracted with dichloromethane (100mL × 2). The organic layer was collected, dried over MgSO<sub>4</sub> and then concentrated in vacuo. The residue was then purified with flash chromatography on silica gel (ethyl acetate/ hexanes = 5 /95 (V/V)) to give 3.07 g product **12** as white crystal. The yield is 66.2%. <sup>1</sup>H-NMR (CDCl<sub>3</sub>, 400 MHz) δ 8.00 (d, 2H, J = 8.9 Hz), 6.94 (d, 2H, J = 8.9 Hz), 4.84 (t, 1H, J = 4.2 Hz), 4.72 (t, 1H, J = 4.2 Hz), 4.30 (t, 1H, J = 4.1 Hz), 4.23 (t, 1H, J = 4.1 Hz), 3.89 (s, 3H). <sup>13</sup>C-NMR (CDCl<sub>3</sub>, 400 MHz) δ 166.7, 162.0, 131.6, 123.1, 114.1, 82.4, 80.7, 67.2, 67.0, 51.8.

### 3-(4-(2-fluoroethoxy)phenyl)-3-oxopropanenitrile (**8**)

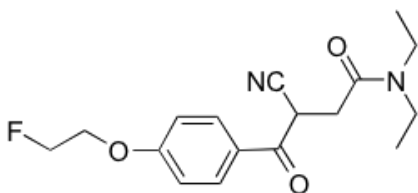


To a solution of acetonitrile (3.21g, 78.2 mmol) in 60 mL anhydrous THF at -78 °C under nitrogen was added a solution of LiHDMS (47.0 mmol) in dry THF dropwise. The mixture was then stirred at -78°C for 20 min, followed by the addition of **1** (3.1g, 15.6mmol). The reaction was then allowed to reach room temperature slowly and stirred at room temperature overnight. The reaction was monitored with LCMS. When completed, the reaction mixture was cooled down to 0 °C and acidified with HCl (2N) to pH 2.0. Crude product was then extracted with dichloromethane (150 mL × 2). The organic layer was then collected and concentrated in vacuo. The crude product was used without further purification.



$^1\text{H-NMR}$  ( $\text{CDCl}_3$ , 400 MHz)  $\delta$  7.91 (d, 2H,  $J = 8.9$  Hz), 7.02 (d, 2H,  $J = 8.9$  Hz), 4.86 (t, 1H,  $J = 4.2$  Hz), 4.73 (t, 1H,  $J = 4.2$  Hz), 4.35 (t, 1H,  $J = 4.1$  Hz), 4.28 (t, 1H,  $J = 4.1$  Hz).  $^{13}\text{C-NMR}$  ( $\text{CDCl}_3$ , 400 MHz)  $\delta$  185.3, 163.4, 130.9, 127.7, 114.8, 113.9, 82.3, 80.5, 67.4, 67.2, 29.0. HRMS calcd for  $\text{C}_{11}\text{H}_{10}\text{FNO}_2$ ,  $m/z = 208.0774$   $[\text{M} + \text{H}]^+$ , found 208.0768.

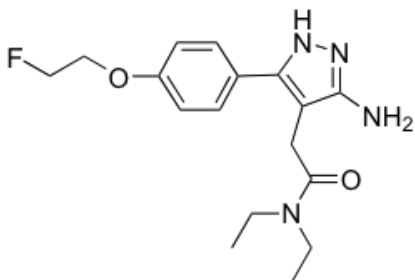
### 3-cyano-*N,N*-diethyl-4-(4-(2-fluoroethoxy)phenyl)-4-oxobutanamide (9)



To a solution of **8** (0.8 g, 3.86 mmol) in 40 mL 80% EtOH in water, were added 2-chloro-*N,N*-diethylacetamide (0.58g, 3.86 mmol), NaOH (0.23 g, 5.8 mmol) and NaI (1.74g, 5.79 mmol). The reaction mixture was irradiated with microwave at 80°C for 40 min. The reaction was monitored with LCMS. When completed, reaction mixture was concentrated *in vacuo*. The residue was purified with flash chromatography (Ethyl acetate/ Hexanes = 1:1 (V/V)), which afforded 0.67 g desired product as brown oil. The yield is 55%.  $^1\text{H-NMR}$  ( $\text{CDCl}_3$ , 400 MHz)  $\delta$  8.05 (d, 2H,  $J = 8.9$  Hz), 7.02 (d, 2H,  $J = 8.9$  Hz), 5.00 (t, 1H,  $J = 4.2$  Hz), 4.84 (t, 1H,  $J = 4.2$  Hz), 4.72 (t, 1H,  $J = 4.1$  Hz), 4.33 (t, 1H,  $J = 4.1$  Hz), 4.26 (t, 1H,  $J = 4.1$  Hz), 3.38 (q, 4H,  $J = 7.0$  Hz), 3.31 (m, 1H), 2.86 (dd, 1H,  $J_1 = 16.2$  Hz,  $J_2 = 4.5$  Hz), 1.28 (t, 3H,  $J = 4.1$  Hz), 1.09 (t, 3H,  $J = 4.1$  Hz).  $^{13}\text{C-NMR}$  ( $\text{CDCl}_3$ , 400

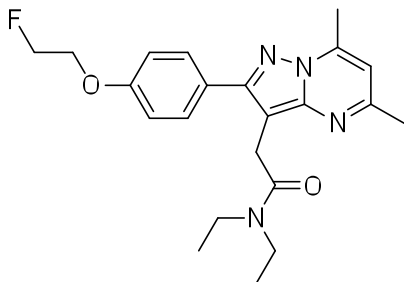
MHz)  $\delta$  187.8, 167.1, 163.3, 131.4, 127.6, 117.4, 114.7 82.3, 80.6, 67.4, 67.2, 60.3, 42.0. HRMS calcd for C<sub>17</sub>H<sub>21</sub>FN<sub>2</sub>O<sub>3</sub>, m/z = 319.1458, found 319.1454.

**2-(3-amino-5-(4-(2-fluoroethoxy)phenyl)-1H-pyrazol-4-yl)-N,N-diethylacetamide (10)**



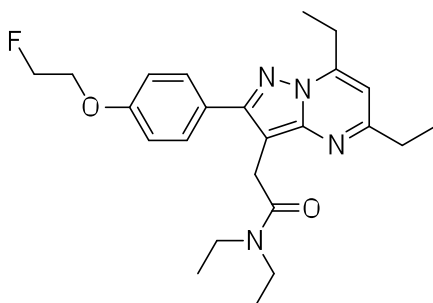
To a solution of **9** (0.67g, 2.09mmol) in 40 mL EtOH were added hydrazine (0.13 g, 4.18 mmol) and AcOH (0.13 mL). The reaction was irradiated with microwave at 90°C for 40 min while monitored with LCMS. When completed, the reaction mixture was concentrated *in vacuo*. The residue was purified with flash chromatography (CH<sub>2</sub>Cl<sub>2</sub>/MeOH = 9 :1 (V/V)), which afforded 0.38g **10** as yellow crystal. The yield is 55%. . <sup>1</sup>H-NMR (CDCl<sub>3</sub>, 400 MHz)  $\delta$  7.33 (d, 2H, J = 8.7 Hz), 6.99 (d, 2H, J = 8.7 Hz), 4.84 (t, 1H, J = 4.2 Hz), 4.73 (t, 1H, J = 4.2 Hz), 4.28 (t, 1H, J = 4.1 Hz), 4.22 (t, 1H, J = 4.1 Hz), 3.50 (s, 2H), 3.33 (q, 2H, J = 7.2 Hz), 3.06 (q, 2H, J = 7.2 Hz), 1.08 (t, 3H, J = 7.1 Hz), 0.93 (t, 3H, J = 7.2 Hz). <sup>13</sup>C-NMR (CDCl<sub>3</sub>, 400 MHz)  $\delta$  170.2, 158.6, 154.8, 142.1, 129.1, 123.6, 115.0, 97.8, 82.6, 80.9, 67.2, 67.0, 42.3, 40.5, 28.4, 14.0, 13.0. HRMS calcd for C<sub>17</sub>H<sub>23</sub>FN<sub>4</sub>O<sub>2</sub>, m/z = 357.1703 [M+ Na]<sup>+</sup>, found 357.1692.

***N,N*-diethyl-2-(2-(4-(2-fluoroethoxy)phenyl)-5,7-dimethylpyrazolo[1,5-*a*]pyrimidin-3-yl)acetamide (7a, DPA-714)**



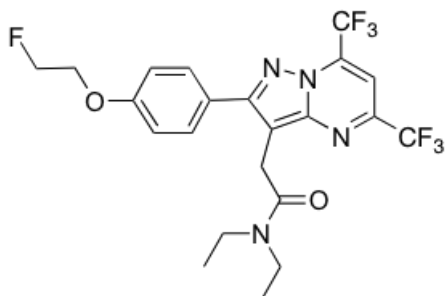
To a solution of **10** (20 mg, 0.06 mmol) in 4 mL EtOH was added acetylacetone (6 mg, 0.06 mmol). The reaction mixture was irradiated with microwave at 180°C for 40 min. The reaction was monitored with LCMS. When completed, the reaction was concentrated in vacuo and the residue was purified with HPLC, which afforded 12.5 mg **7a** (53.7%). [Found: C, 66.56; H, 6.94. C<sub>22</sub>H<sub>27</sub>FN<sub>4</sub>O<sub>2</sub> requires C, 66.31; H, 6.83%]. <sup>1</sup>H-NMR (CDCl<sub>3</sub>, 400 MHz) δ 7.68 (d, 2H, J = 8.8 Hz), 7.02 (d, 2H, J = 8.8 Hz), 6.58 (s, 1H), 4.85 (t, 1H, 4.2Hz), 4.73 (t, 1H, 4.2Hz) 4.30 (t, 1H, 4.4Hz), 4.23 (t, 1H, 4.4Hz), 3.98 (s, 2H), 3.47 (q, 2H, J = 7.2 Hz), 3.42 (q, 2H, J = 7.2 Hz), 2.79 (s, 3H), 2.62 (s, 3H), 1.21 (t, 3H, J = 7.2 Hz), 1.12 (t, 3H, J = 7.2 Hz). <sup>13</sup>C-NMR (CDCl<sub>3</sub>, 400 MHz) δ 170.1, 158.9, 157.8, 155.8, 147.0, 145.70, 130.0, 126.0, 114.7, 108.1, 100.2, 82.6, 80.9, 67.2, 67.0, 42.3, 40.9, 27.9, 23.3, 17.0, 14.0, 12.8. HRMS calcd for C<sub>22</sub>H<sub>27</sub>FN<sub>4</sub>O<sub>2</sub>Na m/z = 421.2016 [M + Na]<sup>+</sup>, found 421.2006.

**2-(5,7-diethyl-2-(4-(2-fluoroethoxy)phenyl)pyrazolo[1,5-*a*]pyrimidin-3-yl)-*N,N*-diethylacetamide (7b, VUIIS1008)**



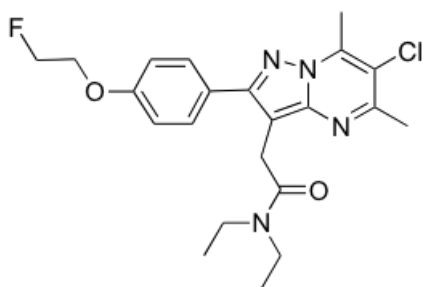
To a solution of **10** (20 mg, 0.06 mmol) in 4 mL EtOH was added 3,5-heptanedione (7.7 mg, 0.06 mmol). The reaction mixture was irradiated with microwave at 180°C for 40 min. The reaction was monitored with LCMS. When completed, the reaction was concentrated in vacuo and the residue was purified with HPLC, which afforded 8.4 mg **7b** (32.96%). <sup>1</sup>H-NMR (CDCl<sub>3</sub>, 400 MHz) δ 7.80 (d, 2H, J = 8.8 Hz), 7.02 (d, 2H, J = 8.8 Hz), 6.54 (s, 1H), 4.85 (t, 1H, 4.2 Hz), 4.73 (t, 1H, J = 4.3 Hz) 4.31 (t, 1H, J = 4.2 Hz), 4.23 (t, 1H, J = 4.2 Hz), 3.95 (s, 2H), 3.54 (q, 2H, J = 7.2 Hz), 3.41 (q, 2H, J = 7.2 Hz), 3.21 (q, 2H, J = 7.2 Hz), 2.86 (q, 2H, J = 7.2 Hz), 1.45 (t, 3H, J = 7.2 Hz), 1.34 (t, 3H, J = 7.2 Hz), 1.20 (t, 3H, J = 7.2 Hz), 1.11 (t, 3H, J = 7.2 Hz). <sup>13</sup>C-NMR (CDCl<sub>3</sub>, 400 MHz) δ 170.40, 162.40, 158.60, 154.91, 150.36, 146.97, 130.05, 126.76, 114.61, 104.80, 100.55, 82.69, 80.99, 67.17, 66.96, 42.40, 40.74, 31.01, 27.98, 23.30, 14.22, 12.94, 12.84, 10.21. HRMS calcd for C<sub>24</sub>H<sub>31</sub>FN<sub>4</sub>O<sub>2</sub> m/z = 427.2509 (M+H)<sup>+</sup>, found 427.2500.

***N,N*-diethyl-2-(2-(4-(2-fluoroethoxy)phenyl)-5,7-bis(trifluoromethyl)pyrazolo [1,5-a]pyrimidin-3-yl)acetamide (7c)**



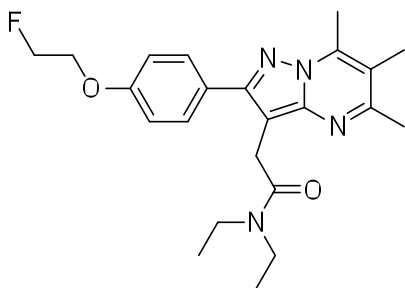
To a solution of **10** (20 mg, 0.06 mmol) in 4 mL EtOH was added hexafluoroacetylacetone (12.4 mg, 0.06 mmol). The reaction mixture was irradiated with microwave at 190°C for 40 min. The reaction was monitored with LCMS. When completed, the reaction was concentrated in vacuo and the residue was purified with HPLC, which will give 2.5 mg **7c** (8.26%). <sup>1</sup>H-NMR (CDCl<sub>3</sub>, 400 MHz) δ 7.89 (d, 2H, J = 8.8 Hz), 7.39 (s, 1H), 7.05 (d, 2H, J = 8.8 Hz), 4.86 (t, 1H, J = 4.2 Hz), 4.74 (t, 1H, J = 4.2 Hz), 4.32 (t, 1H, J = 4.2 Hz), 4.25 (t, 1H, J = 4.2 Hz), 4.04 (s, 2H), 3.59 (q, 2H, J = 7.2 Hz), 3.45 (q, 2H, J = 7.2 Hz), 1.33 (t, 3H, J = 7.2 Hz), 1.15 (t, 3H, J = 7.2 Hz). HRMS calcd for C<sub>22</sub>H<sub>21</sub>F<sub>7</sub>N<sub>4</sub>O<sub>2</sub> m/z = 507.1631 (MH<sup>+</sup>), found 507.1622.

**2-(6-chloro-2-(4-(2-fluoroethoxy)phenyl)-5,7-dimethylpyrazolo[1,5-a]pyrimidin-3-yl)-N,N-diethylacetamide (7d)**



To a solution of **10** (20 mg, 0.06 mmol) in 4 mL EtOH was added 3-chloro-2,4-pentanedione (8 mg, 0.06 mmol). The reaction mixture was irradiated with microwave at 180°C for 40 min. The reaction was monitored with LCMS. When completed, the reaction was concentrated in vacuo and the residue was purified with HPLC, which afforded 21.1 mg **7d** (81.64%). <sup>1</sup>H-NMR (CDCl<sub>3</sub>, 400 MHz) δ 7.79 (d, 2H, J = 8.8 Hz), 7.02 (d, 2H, J = 8.8 Hz), 4.84 (t, 1H, J = 4.2 Hz), 4.72 (t, 1H, J = 4.2 Hz), 4.30 (t, 1H, J = 4.2 Hz), 4.23 (t, 1H, J = 4.1 Hz), 3.90 (s, 2H), 3.51 (q, 2H, J = 7.2 Hz), 3.42 (q, 2H, J = 7.2 Hz), 2.91 (s, 3H), 2.65 (s, 3H), 1.23 (t, 3H, J = 7.2 Hz), 1.12 (t, 3H, J = 7.2 Hz). HRMS calcd for C<sub>22</sub>H<sub>26</sub>ClFN<sub>4</sub>O<sub>2</sub> m/z = 433.1807(MH<sup>+</sup>), found 433.1790.

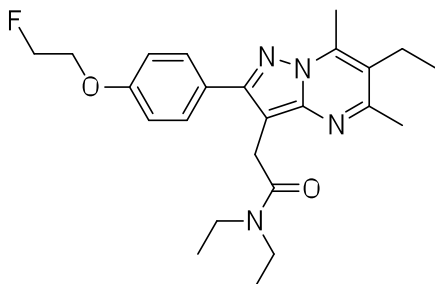
***N,N*-diethyl-2-(2-(4-(2-fluoroethoxy)phenyl)-5,6,7-trimethylpyrazolo[1,5-a]pyrimidin-3-yl)acetamide (7e)**



To a solution of **10** (20 mg, 0.06 mmol) in 4 mL EtOH was added 3-methyl-2,4-pentanedione (6.8 mg, 0.06 mmol). The reaction mixture was irradiated with microwave at 180°C for 40 min. The reaction was monitored with LCMS. When completed, the reaction was concentrated in vacuo and the residue was purified with HPLC, which afforded 11.2 mg **7e** (45.43%). <sup>1</sup>H-NMR (CDCl<sub>3</sub>,

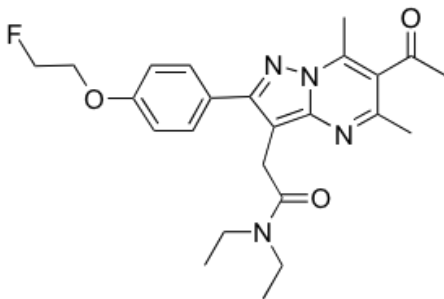
400 MHz)  $\delta$  7.66 (d, 2H, J = 8.8 Hz), 7.02 (d, 2H, J = 8.8 Hz), 4.85 (t, 1H, J = 4.2 Hz), 4.73 (t, 1H, J = 4.3 Hz), 4.31 (t, 1H, J = 4.2 Hz), 4.23 (t, 1H, J = 4.2 Hz), 4.00 (s, 2H), 3.44 (q, 4H, J = 7.2 Hz), 2.87 (s, 3H), 2.67 (s, 3H), 2.34 (s, 3H), 1.20 (t, 3H, J = 7.2 Hz), 1.12 (t, 3H, J = 7.2 Hz). HRMS calcd for C<sub>23</sub>H<sub>29</sub>FN<sub>4</sub>O<sub>2</sub> m/z = 413.2353 (MH<sup>+</sup>), found 413.2349.

***N,N*-diethyl-2-(6-ethyl-2-(4-(2-fluoroethoxy)phenyl)-5,7-dimethylpyrazolo [1,5-a]pyrimidin-3-yl)acetamide (7f)**



To a solution of **10** (20 mg, 0.06 mmol) in 4 mL EtOH was added 3-ethyl-2,4-pentanedione (7.7 mg, 0.06 mmol). The reaction mixture was irradiated with microwave at 180°C for 40 min. The reaction was monitored with LCMS. When completed, the reaction was concentrated in vacuo and the residue was purified with HPLC, which afforded 4.2 mg **7f** (16.47%). <sup>1</sup>H-NMR (CDCl<sub>3</sub>, 400 MHz)  $\delta$  7.78 (d, 2H, J = 8.8 Hz), 7.01 (d, 2H, J = 8.8 Hz), 4.84 (t, 1H, J = 4.2 Hz), 4.72 (t, 1H, J = 4.2 Hz), 4.30 (t, 1H, J = 4.2 Hz), 4.23 (t, 1H, J = 4.2 Hz), 3.92 (s, 2H), 3.51 (q, 2H, J = 7.2 Hz), 3.41 (q, 2H, J = 7.2 Hz), 2.79 (s, 3H), 2.73 (q, 2H, J = 7.2 Hz), 2.60 (s, 3H), 1.20 (m, 6H), 1.12 (t, 3H, J = 8.5 Hz). HRMS calcd for C<sub>24</sub>H<sub>31</sub>FN<sub>4</sub>O<sub>2</sub> m/z = 427.2509 (M + H)<sup>+</sup>, found 427.2496.

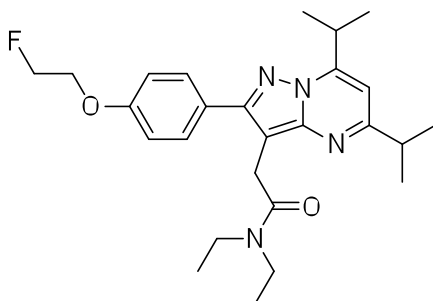
**2-(6-acetyl-2-(4-(2-fluoroethoxy)phenyl)-5,7-dimethylpyrazolo[1,5-a]pyrimidin-3-yl)-*N,N*-diethylacetamide (7g)**



To a solution of **10** (20 mg, 0.06 mmol) in 4.0 mL EtOH was added triacetylmethane (8.5 mg, 0.06 mmol). The reaction mixture was irradiated with microwave at 140°C for 30 min. The reaction was monitored with LCMS. When completed, the reaction was concentrated in vacuo and the residue was purified with HPLC, which afforded 3.4 mg **7g** (12.91%). <sup>1</sup>H-NMR (CDCl<sub>3</sub>, 400 MHz) δ 7.77 (d, 2H, J = 8.8 Hz), 7.02 (d, 2H, J = 8.8 Hz), 4.85 (t, 1H, J = 4.2 Hz), 4.73 (t, 1H, J = 4.2 Hz), 4.31 (t, 1H, J = 4.2 Hz), 4.24 (t, 1H, J = 4.2 Hz), 3.92 (s, 2H), 3.52 (q, 2H, J = 7.2 Hz), 3.43 (q, 2H, J = 7.2 Hz), 2.76 (s, 3H), 2.59 (s, 3H), 2.53 (s, 3H), 1.25 (t, 3H, J = 7.2 Hz), 1.13 (t, 3H, J = 7.2 Hz). HRMS calcd for C<sub>24</sub>H<sub>29</sub>FN<sub>4</sub>O<sub>3</sub> m/z = 441.2302 (MH<sup>+</sup>), found 441.2295.

***N,N*-diethyl-2-(2-(4-(2-fluoroethoxy)phenyl)-5,7-diisopropylpyrazolo[1,5-a]pyrimidin-3-yl)acetamide (7h)**





To a solution of **10** (20 mg, 0.06 mmol) in 4 mL EtOH was added 2,6-dimethyl-3,5-heptanedione (9.3 mg, 0.06 mmol). The reaction mixture was irradiated with microwave at 195°C for 40 min. The reaction was monitored with LCMS. When completed, the reaction was concentrated in vacuo and the residue was purified with HPLC, which afforded 2.4 mg **7h** (8.83%). <sup>1</sup>H-NMR (CDCl<sub>3</sub>, 400 MHz) δ 7.91 (d, 2H, J = 8.8 Hz), 7.02 (d, 2H, J = 8.8 Hz), 6.50 (s, 1H), 4.85 (t, 1H, J = 4.3 Hz), 4.73 (t, 1H, J = 4.3 Hz), 4.31 (t, 1H, J = 4.2 Hz), 4.23 (t, 1H, J = 4.2 Hz), 3.93 (s, 2H), 3.88 (m, 1H), 3.63 (q, 2H, J = 7.2 Hz), 3.41 (q, 2H, J = 7.2 Hz), 3.05 (m, 1H), 1.44 (d, 6H, J = 5.6 Hz), 1.33 (d, 6H, J = 5.6 Hz), 1.23 (t, 3H, J = 7.1 Hz), 1.11 (t, 3H, J = 7.1 Hz). HRMS calcd for C<sub>26</sub>H<sub>35</sub>FN<sub>4</sub>O<sub>2</sub> m/z = 455.2822 (MH<sup>+</sup>), found 455.2815.

## CHAPTER 5

### SYNTHESIS AND STRUCTURE-ACTIVITY RELATIONSHIPS OF 5,6,7-SUBSTITUTED PYRAZOLOPYRIMIDINES: DISCOVERY OF A NOVEL TSPO PET LIGAND FOR CANCER IMAGING

#### 5.1. Abstract

Focused library synthesis and structure-activity relationship development of 5,6,7-substituted pyrazolopyrimidines led to the discovery of VUUIS1008 (**6b**), a translocator protein (TSPO) ligand exhibiting a 36-fold enhancement in affinity compared to the previously reported pyrazolopyrimidine-based TSPO ligand, DPA-714 (**6a**). Radiolabeling of precursor **7** with fluorine-18 ( $^{18}\text{F}$ ) facilitated the production of  $^{18}\text{F}$ -VUUIS1008 ( $^{18}\text{F}$ -**6b**) in high radiochemical yield and specific activity. Several *in vivo* studies of  $^{18}\text{F}$ -**6b** were performed, including microPET imaging of preclinical gliomas, radiometabolite analysis, and biodistribution, which illuminated this agent as an improved probe for molecular imaging of TSPO-expressing cancers and potentially other diseases.

#### 5.2 Introduction

There remains a critical need to develop and rigorously validate molecular imaging biomarkers that aid tumor diagnosis, predict clinical outcome, and quantify response to therapeutic interventions. Imaging techniques routinely used in clinical oncology include magnetic resonance imaging (MRI), X-ray computed

tomography (CT), ultrasound imaging (US), and positron emission tomography (PET). Of these, the sensitivity and quantitative nature of PET, coupled with the ability to readily produce biologically active compounds bearing positron-emitting isotopes (e.g.,  $^{11}\text{C}$ ,  $^{18}\text{F}$ ), renders PET imaging as one of the most attractive techniques for detecting tumors and profiling their molecular features. By far, the most widely used PET tracer in clinical oncology is 2-deoxy-2- $^{18}\text{F}$ fluoro-D-glucose ( $^{18}\text{F}$ -FDG), a probe that accumulates in tissue as a function of glucose utilization. PET using  $^{18}\text{F}$ -FDG is a powerful approach for tumor detection in many organ sites. However, not all tumors exhibit elevated glucose avidity, and  $^{18}\text{F}$ -FDG uptake can be affected by a plethora of normal metabolic processes. Furthermore, tumor imaging can be confounded by  $^{18}\text{F}$ -FDG uptake in normal tissues such as healthy brain. These issues highlight an unmet need to explore and validate additional molecular targets for cancer imaging.

Our laboratory has explored translocator protein (TSPO) expression as a target for molecular imaging of cancer.<sup>7, 25, 26, 35, 37</sup> Formerly referred to as peripheral benzodiazepine receptor (PBR), TSPO is an 18-kDa protein typically localized to the outer mitochondria membrane. TSPO participates in the regulation of numerous cellular processes, including steroid biosynthesis, cholesterol metabolism, apoptosis, and cellular proliferation.<sup>1</sup> In normal tissues, TSPO tends to be expressed in those that produce steroids and those which are mitochondrial-enriched such as myocardium, skeletal muscle, and renal tissue. Tissues such as liver and brain exhibit comparatively modest expression.<sup>1</sup> While classically exploited as a target in neuroscience, elevated TSPO expression is

also observed in cancers of the breast,<sup>10, 11</sup> prostate,<sup>8, 9</sup> oral cavity,<sup>16</sup> colon,<sup>6, 7, 20</sup> liver,<sup>15, 65</sup> and brain.<sup>14, 54</sup> In oncology, TSPO expression is typically linked with disease progression and diminished survival<sup>5, 16, 20, 53, 55</sup> and is a hallmark of aggressive and potentially metastatic tumors.<sup>8, 10, 56</sup> For this reason, our laboratory has explored the use of TSPO imaging ligands within the context of colon cancer,<sup>7</sup> breast cancer,<sup>25</sup> and glioma,<sup>35, 37</sup> as these agents could potentially serve as useful cancer imaging biomarkers. We recently reported the first utilization of the PET agents <sup>18</sup>F-PBR06<sup>35</sup> and <sup>18</sup>F-DPA-714<sup>37</sup> for quantitative assessment of TSPO expression in preclinical glioma. In these proof-of-principle PET imaging studies, tumors were detectable among surrounding normal brain and, importantly, TSPO levels could be quantitatively assayed in tumors using compartmental analysis of the PET data.<sup>35, 37</sup> However, drawbacks were observed with both agents in this context, including tracer accumulation in normal brain that reached levels potentially sufficient to prevent detection of gliomas with modest TSPO expression. Both tracers also exhibited significant metabolism *in vivo*, which required correction of plasma input functions for quantitative analysis. While illustrating the potential of TSPO PET to detect tumors in brain, these studies prompted our desire to develop novel TSPO PET ligands with improved properties for cancer imaging.

The goal of this study was to determine whether optimization of the pyrazolopyrimidine scaffold, specifically at the 5-, 6-, and 7-positions, would yield TSPO ligands with greater affinity and potentially serve as more robust PET imaging ligands *in vivo*. These experiments led to the discovery of VUIIS1008

**(6b)**, a TSPO-selective ligand that exhibits a surprising 36-fold enhancement in affinity compared to another pyrazolopyrimidine, DPA-714 (**6a**). VUUIS1008 analog **7** could be radiolabeled with fluorine-18 ( $^{18}\text{F}$ ) to yield  $^{18}\text{F}$ -VUUIS1008 ( **$^{18}\text{F}$ -6b**), which was subsequently evaluated in vivo in healthy rats and a preclinical model of glioma.  **$^{18}\text{F}$ -6b** exhibited negligible accumulation in normal brain, yet robust accumulation in tumor tissue, which facilitated excellent imaging contrast. Furthermore, we observed improved in vivo stability of  **$^{18}\text{F}$ -6b** compared to  $^{18}\text{F}$ -DPA-714.<sup>37</sup> Overall, these studies illuminate  **$^{18}\text{F}$ -6b** as a promising, novel PET ligand for evaluating TSPO expression in tumors and potentially other diseases.

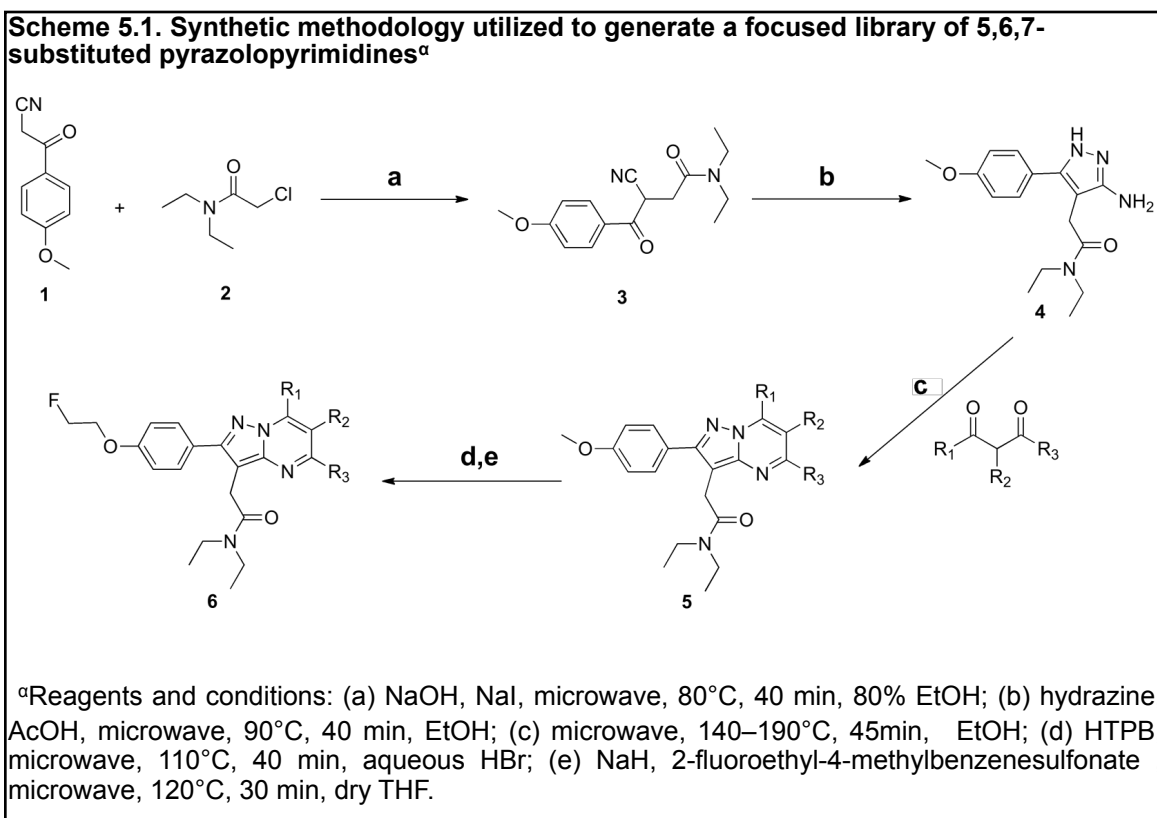
### 5.3 Results and Discussion

#### Chemistry

MAOS of 5,6,7-substituted Pyrazolopyrimidine Library. A library of structurally diverse pyrazolopyrimidines (**Table 5.1**) was assembled using a microwave-assisted organic synthesis (MAOS) method that prioritized points of divergence at the 5- $\text{R}_3$ , 6- $\text{R}_2$ , and 7- $\text{R}_1$  positions on the core pyrazolopyrimidine scaffold. Members of this library were formed through condensation of a pyrazole core (**4**) with various substituted diones.<sup>27</sup> Entries in **Table 5.1** fall into two distinct series (**5** and **6**), with seven compounds (**a-g**) per series. Each compound within the series results from one of seven diones utilized, while each series is differentiated by the installation of a unique surrogate imaging handle at the 4-

position ( $R_4$ ) of the 2-phenyl group pendant to the core scaffold. Series **5** entries (**5a-5g**) feature a methoxy group at  $R_4$  and include a previously reported pyrazolopyrimidine, DPA-713 (**5a**), while series **6** entries (**6a-6g**) feature a 2-fluoroethoxy group at  $R_4$  and include DPA-714 (**6a**). Given our ultimate goal of developing novel PET imaging ligands, coupled with an interest in expanding structure-activity relationships (SAR) around the 5,6,7-substituted pyrazolopyrimidine core, we rationalized that maintaining the surrogate imaging handles of future representative imaging probes would accelerate the development of novel agents.

The overall synthetic methodology is presented in **Scheme 5.1**.<sup>27</sup> Here, compound **4**, bearing a 3-amino-1H-pyrazole core, was accessible in two steps



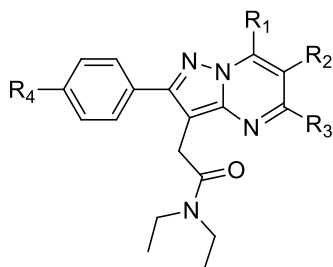
using MAOS from commercially available phenylpropanenitrile **1** and chloroacetamide **2**. From **4**, the synthesis diverges at the condensation step with a series of unique diones to yield the “five” series of pyrazolopyrimidines (**5a-5g**) that mimic analogous <sup>11</sup>C-based PET probes with an R<sub>4</sub>-OMe. Subsequently, compounds **6a-6g** were achieved by cleavage of methoxy group followed by microwave-assisted ether synthesis with 2-fluoroethyl-4-methylbenzenesulfonate which yielded an R<sub>4</sub>-2-fluoroethoxy surrogate imaging handle to mimic <sup>18</sup>F-labeled PET probes (**Table 5.1**). The library developed primarily explored the effects of R<sub>1</sub>, R<sub>2</sub>, and R<sub>3</sub> substituents that varied in steric bulk. Generally, substituents at R<sub>1</sub> and R<sub>3</sub> mirrored one other and consisted of linear and branched alkyl substituents such as methyl, ethyl, and isopropyl moieties. These substituents were cross-matched with similar groups at the R<sub>2</sub> position, which included hydrogen, methyl, ethyl, chloro, and 2-propanone.

### Lipophilicity

Lipophilicity of series **5** and **6** were evaluated at pH = 7.5 (log P<sub>7.5</sub>) using reversed phase HPLC<sup>66</sup> and is tabulated in **Table 5.1**. The values for library entries varied from 2.0 to 3.0 for both series and correlated predictably with dione structure, where polarity and hydrocarbon content of the R<sub>1</sub>-R<sub>3</sub> substituents appeared to be key determinants. In both series, analogs **a**, **d**, and **f**, with R<sub>1</sub>-R<sub>3</sub> combinations of hydrogen, methyl, and 2-propanone, proved the least lipophilic. Introduction of ethyl groups at R<sub>1</sub>, R<sub>2</sub>, or R<sub>3</sub> increased log P<sub>7.5</sub> values accordingly,

as with analogs **b** and **e**, which ranged from 2.50-2.84. The most lipophilic analogs proved to be **c** and **g** ( $\log P_{7.5} = 2.55$ -2.99), with isopropyl groups at the  $R_1$  and  $R_3$  positions or chlorine at  $R_2$ . Interestingly, of the two series, series **5** ( $R_4 = \text{OMe}$ ), tended to be more lipophilic than series **6** ( $R_4 = \text{OCH}_2\text{CH}_2\text{F}$ ). Overall, the library entries exhibited lipophilicities (2.07–2.99) suitable for *in vivo* imaging<sup>67</sup>, where potential agents must be sufficiently membrane penetrant to bind intracellular targets such as TSPO.

**Table 5.1.** Affinity, lipophilicity, and molecular weight of pyrazolopyrimidines



Compd	$R_1$	$R_2$	$R_3$	$R_4$	MW	$\text{Log}P_{7.5}$	$K_i$ (nM) <sup>4</sup>
5a <sup>1</sup>	-Me	-H	-Me	-OMe	366.21	2.40	12.23
5b	-Et	-H	-Et	-OMe	394.51	2.84	0.18
5c	-iPr	-H	-iPr	-OMe	422.56	2.98	>500
5d	-Me	-Me	-Me	-OMe	380.48	2.45	93.75
5e	-Me	-Et	-Me	-OMe	394.51	2.78	157.14
5f	-Me	$-\text{CH}_2\text{C}(\text{O})\text{CH}_3$	-Me	-OMe	408.49	2.57	200.89
5g	-Me	-Cl	-Me	-OMe	400.9	2.99	55.36
6a <sup>2</sup>	-Me	-H	-Me	$-\text{OCH}_2\text{CH}_2\text{F}$	398.47	2.12	9.73
6b <sup>3</sup>	-Et	-H	-Et	$-\text{OCH}_2\text{CH}_2\text{F}$	426.53	2.50	0.27 <sup>5</sup>
6c	-iPr	-H	-iPr	$-\text{OCH}_2\text{CH}_2\text{F}$	454.58	2.73	>500
6d	-Me	-Me	-Me	$-\text{OCH}_2\text{CH}_2\text{F}$	412.5	2.47	83.04
6e	-Me	-Et	-Me	$-\text{OCH}_2\text{CH}_2\text{F}$	426.53	2.53	276.79
6f	-Me	$-\text{CH}_2\text{C}(\text{O})\text{CH}_3$	-Me	$-\text{OCH}_2\text{CH}_2\text{F}$	440.51	2.07	251.79
6g	-Me	-Cl	-Me	$-\text{OCH}_2\text{CH}_2\text{F}$	432.92	2.55	67.86

<sup>1</sup>DPA-713. <sup>2</sup>DPA-714. <sup>3</sup>VUIIS-1008. <sup>4</sup>Competitive binding against <sup>3</sup>H-PK 11195 in C6 glioma cell lysate. <sup>5</sup>  $K_i$  versus <sup>3</sup>H-flunitrazepam > 10,000 nM.



## Biologic Testing

Binding Affinity in Cancer Cell Lysate and SAR Analysis. To evaluate binding of the library entries to TSPO, radioligand displacement was carried out in rat glioma cell lysate (C6) using  $^3\text{H}$ -PK 11195.<sup>35, 37</sup> Affinities of library members are expressed as  $K_i$  (nM) values in **Table 5.1**. Encompassing modifications at R<sub>1</sub>-R<sub>4</sub>, both series exhibited a spectrum of  $K_i$  values that spanned micromolar to sub-nanomolar affinity. As expected, replacing the 4-methoxy with 4-(2-fluoroethoxy) at the R<sub>4</sub> position had minimal impact upon TSPO affinity, as similar SAR trends emerged within series **5** and **6**. In contrast, R<sub>1</sub>, R<sub>2</sub>, and R<sub>3</sub> modification led to major impacts upon affinity. Though the R<sub>1</sub> and R<sub>3</sub> positions showed intolerance to steric bulk beyond ethyl, a surprising level of improvement in affinity could be realized by replacing methyl with ethyl at the R<sub>1</sub> and R<sub>3</sub> positions. For example, subnanomolar affinities were observed for analogs **5b** (0.18 nM) and **6b** (VUIIS1008, 0.27 nM), which represent major improvements over their respective leads, DPA-713 (**5a**, 12.23 nM) and DPA-714 (**6a**, 9.73 nM) (**Table 5.1**). Increasing the R<sub>1</sub> and R<sub>3</sub> to a bulkier isopropyl group proved detrimental, with  $K_i$  values for both **5c** and **6c** greater than 500 nM. Overall, the R<sub>2</sub> position was less tolerant to steric or electron density deviations from hydrogen in these studies. Substitution of the nascent R<sub>2</sub> hydrogen (**5a**, **6a**) with methyl (**5d**, 93.75 nM; **6d**, 83.04 nM) decreased affinity approximately 10-fold with respect to their parent compounds, DPA-713 and DPA-714, respectively; this trend was more dramatic

with ethyl substitution (**5e**, 157.14 nM; **6e**, 276.79 nM). Introduction of polarity at the R<sub>2</sub> position with 2-propanone (**5f**, 200.89 nM; **6f**, 251.79 nM) bore similar adverse effects upon affinity. Somewhat less dramatic decreases in affinity were observed upon halogen substitution at R<sub>2</sub> with chlorine (**5g**, 55.36 nM; **6g**, 67.86 nM). Given the size of chlorine atom, lying between methyl and ethyl, it is reasonable that the K<sub>i</sub> of entries **5g** and **6g** are only slightly worse than those with alkyl substituents at the R<sub>2</sub> position (**Table 5.1**). Overall, these experiments illuminated 5,7-diethyl, 6-hydrogen substitution as the optimal pattern in this series to impart improved affinity. Additionally, the studies also suggested that an analog could be produced for PET imaging using either fluorine-18 (**6b**) or carbon-11 (**5a**) substitution on the R<sub>4</sub> position with minimal effect on TSPO affinity and only minor effect on lipophilicity. Since fluorine-18 has a significantly longer half-life than carbon-11 (109.7 min vs. 20.4 min), we elected to carry compound **6b** forward for further characterization. The selectivity of compound **6b** for TSPO over the central benzodiazepine receptor (CBR) was evaluated using radioligand displacement of the CBR ligand <sup>3</sup>H-flunitrazepam in rat cerebral cortex membranes (**Table 5.1**). Unlike the displacement studies with <sup>3</sup>H-PK 11195, compound **6b** demonstrated poor affinity for CBR (K<sub>i</sub> > 10,000 nM), indicating TSPO selectivity.

## **Radioligand Precursor Preparation and Radiosynthesis**

To produce **<sup>18</sup>F-6b**, we synthesized precursor (**7**), a tosylated intermediate prepared from **5b** in two steps with an overall yield of approximately 45% (**Scheme 5.2**). Nucleophilic fluorination of **7** with <sup>18</sup>F-fluoride was then performed (**Scheme 5.3**) in anhydrous dimethyl sulfoxide at 165 °C for 5 minutes. Purification of **<sup>18</sup>F-6b** was carried out with preparative HPLC using 10 mM sodium phosphate buffer (pH 6.7) in ethanol (47.5/52.5, v/v). The retention time of **<sup>18</sup>F-6b** was 12 minutes according to gamma detection and corresponded to the UV retention time of non-radioactive **6b**. Radiochemical purity was consistently greater than 99%, with specific activity consistently greater than 4203 Ci/mmol (156 TBq/mmol) (n = 33).

### **Uptake of <sup>18</sup>F-VUIIS1008 in C6 Glioma**

The in vivo performance of **<sup>18</sup>F-6b** was evaluated in glioma-bearing Wistar rats using microPET imaging, with a typical study shown in **Figure 5.1**. MRI (T<sub>2</sub>-weighted) was used to localize tumors and for registration of anatomical features with PET<sup>35, 37</sup> (**Figure 5.1A**). Dynamic PET imaging with **<sup>18</sup>F-6b** illustrated that the majority of tracer uptake in the brain was localized to the tumor, with very modest accumulation in the adjacent, normal brain (**Figure 5.1B** and **5.1C**). The tumor-selective uptake characteristics of **<sup>18</sup>F-6b** afforded excellent imaging contrast between tumor and normal tissue. In addition to the tumor, accumulation of **<sup>18</sup>F-6b** was observed outside of the brain in olfactory epithelium and the Harderian glands, as well as the tongue, where TSPO expression is elevated.<sup>68</sup>

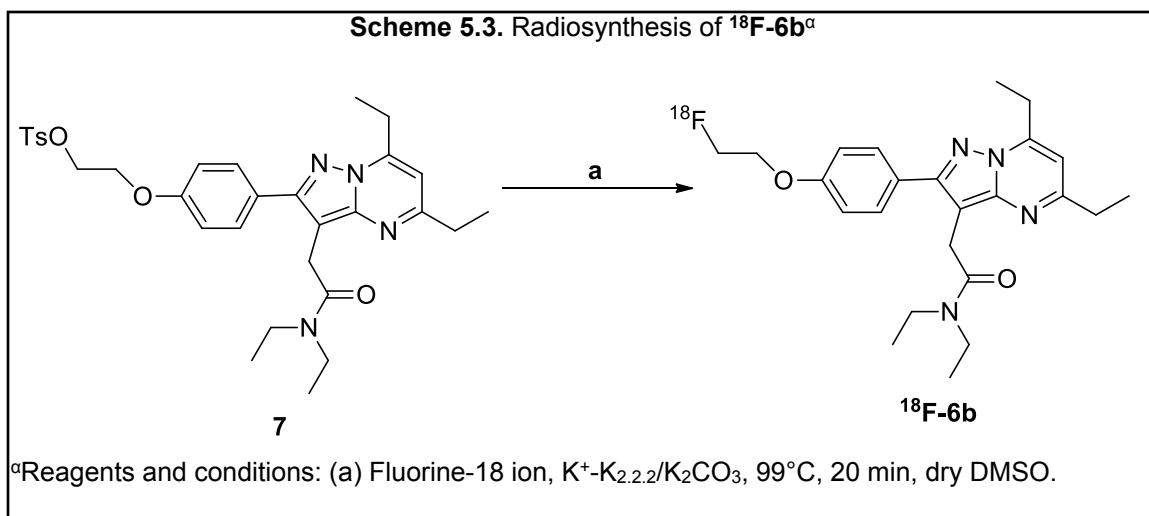
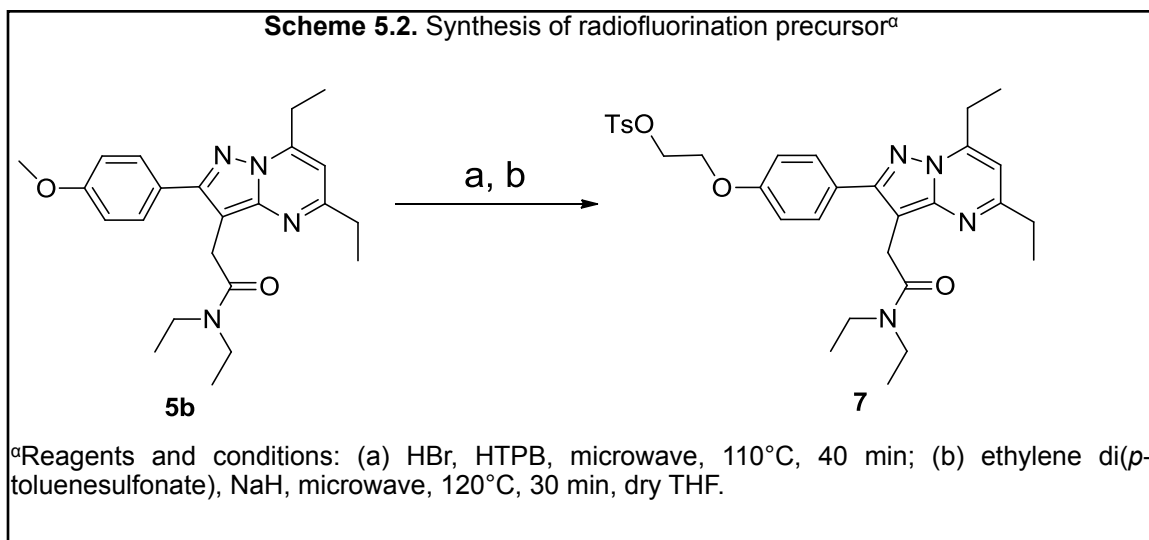
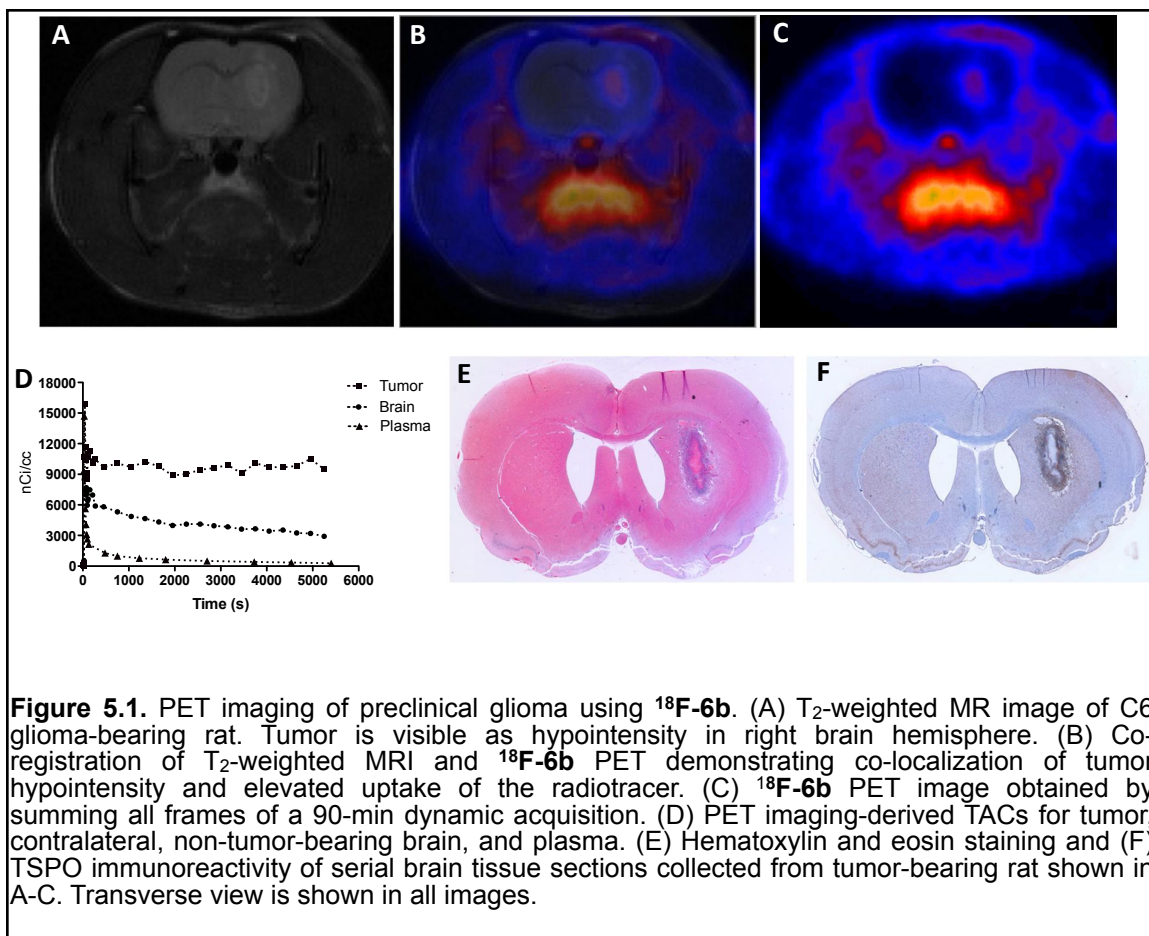


**Figure 5.1D** illustrates time-activity curves (TACs) that were typical of eight representative studies for tumor, normal brain, and plasma over a 90-minute dynamic acquisition. We found that <sup>18</sup>F-6b was rapidly delivered to tumor and normal brain, but cleared tumor tissues at a much slower rate than normal brain. After an initial spike in radioactivity consistent with tracer injection and rapid distribution, <sup>18</sup>F-6b quickly cleared from the plasma. To validate the PET, imaging-matched brains were processed for post mortem staining and immunohistochemistry. We observed close agreement between tumor tissue

(H&E, **Figure 5.1E**), elevated TSPO expression by immunohistochemistry (**Figure 5.1F**), and tumor accumulation of  $^{18}\text{F}$ -**6b** accumulation (**Figure 5.1C**). Potentially, the apparent improved stability of  $^{18}\text{F}$ -**6b** over  $^{18}\text{F}$ -**6a** may stem from the rapid clearance of  $^{18}\text{F}$ -**6b** from plasma, rendering detection of low levels of metabolites challenging with HPLC.



### Characterization of $^{18}\text{F}$ -VUIIS1008 ( $^{18}\text{F}$ -**6b**) Radiometabolites in Plasma

Analogous to our previous work,<sup>37</sup> radio-HPLC was used to evaluate metabolism of  $^{18}\text{F}$ -**6b** in plasma at multiple time points during the PET scanning

period (2, 12, 30, 60, 90 min) (**Figure 5.2**). Parent compound ( **$^{18}\text{F}$ -6b**) was the only radioactive species detected in plasma at all time points, suggesting a lack of circulating  **$^{18}\text{F}$ -6b** metabolites observed over a 90-minute period. This behavior contrasted the *in vivo* performance of  $^{18}\text{F}$ -DPA-714, where we previously observed up to 30% metabolism within the first 12 minutes post-administration.<sup>37</sup> The apparent improved stability of  **$^{18}\text{F}$ -6b** over  $^{18}\text{F}$ -DPA-714 confers several advantages, given the simplification of future quantitative analyses, as well as potentially improved biodistribution and bioavailability.

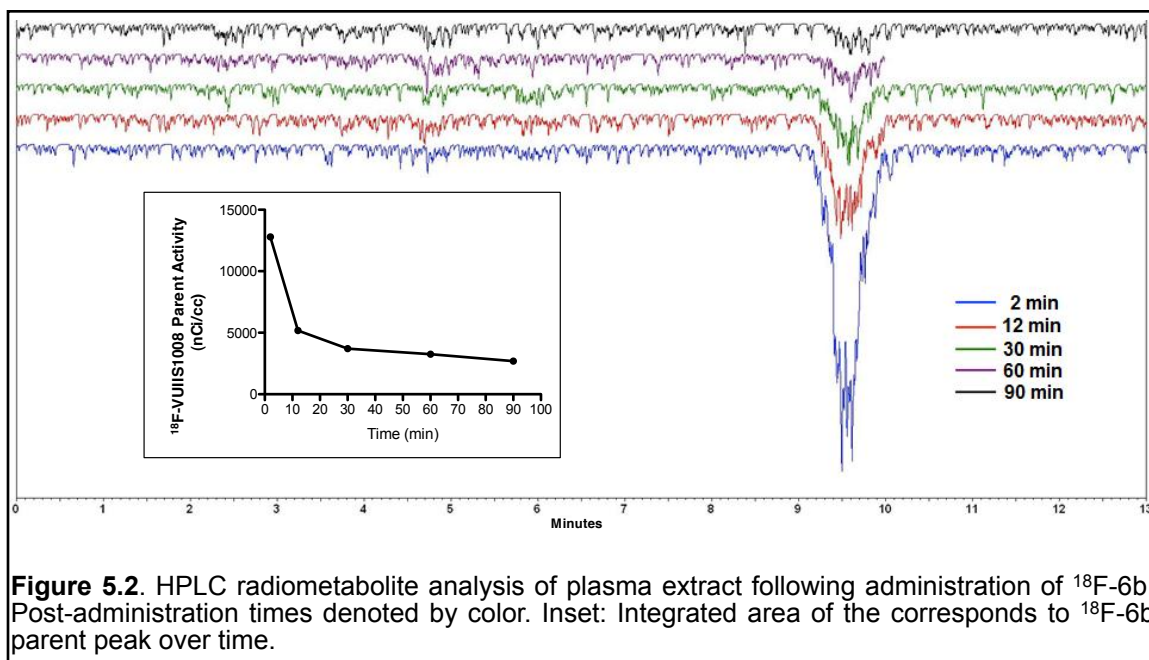


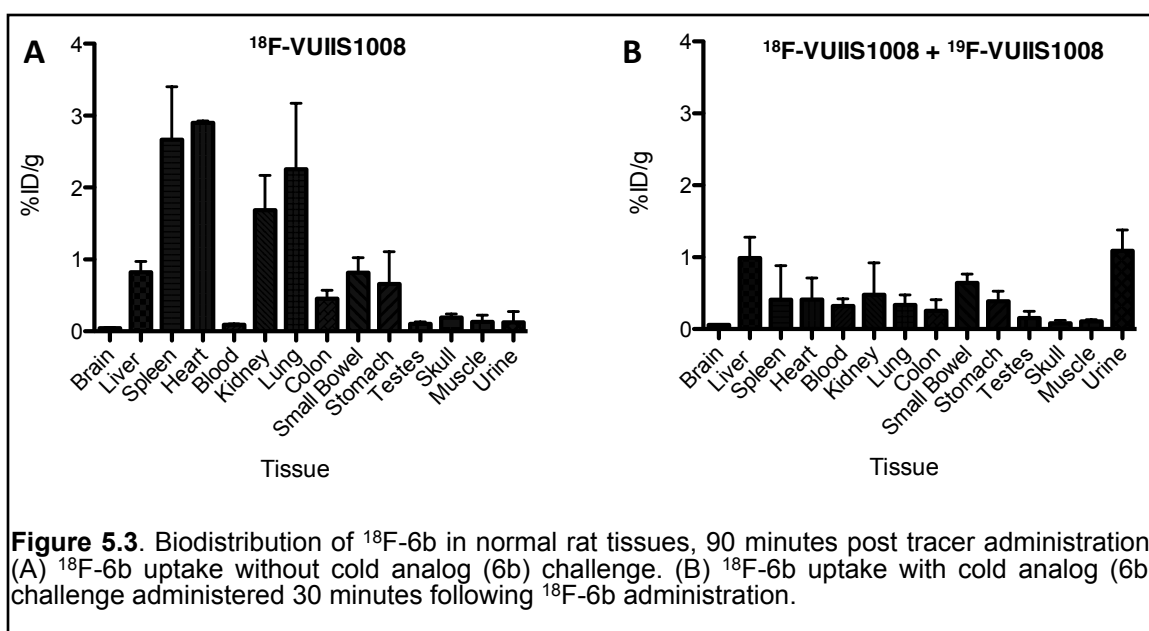
**Figure 5.2.** HPLC radiometabolite analysis of plasma extract following administration of  $^{18}\text{F}$ -6b. Post-administration times denoted by color. Inset: Integrated area of the corresponds to  $^{18}\text{F}$ -6b parent peak over time.

### Biodistribution and Specific Binding of $^{18}\text{F}$ -6b in Rats

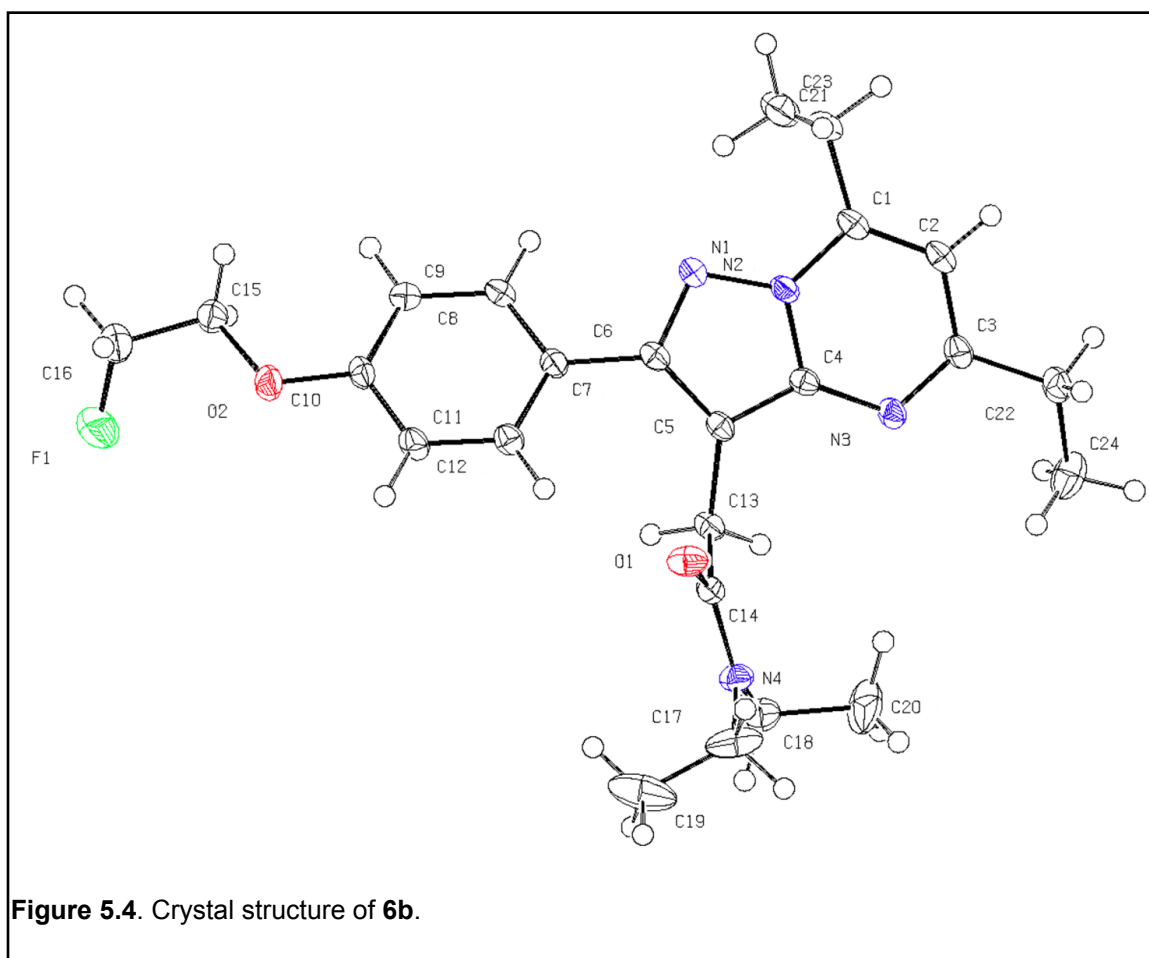
The biodistribution and TSPO-specificity of  **$^{18}\text{F}$ -6b** was evaluated in normal tissues. Tissue samples were harvested 60 minutes after infusion of the  **$^{18}\text{F}$ -6b**. The radioactivity of harvested tissue was measured using standard analytical

methods and recorded as percentage of the injected dose per gram of tissue (%ID/g) (**Figure 5.3A**). Consistent with known TSPO densities,<sup>22</sup> we observed elevated accumulation of <sup>18</sup>F-**6b** in spleen, heart, kidney, and lung.<sup>69</sup> Moderate uptake was also observed in liver, colon, small bowel, and stomach. Very minor accumulation was observed in the brain, testes, skull, and skeletal muscle. At 60 minutes post-administration of tracer, very little radioactivity was observed in biological fluids, such as whole blood or urine.

To evaluate the specific binding of <sup>18</sup>F-**6b** in normal tissue, we carried out a similar 60-minute biodistribution assay that included a bolus infusion of non-radioactive **6b** (10 mg/kg) at 30 minutes (**Figure 5.3B**). With displacement, we observed that activity in the organs exhibiting the greatest accumulation of <sup>18</sup>F-**6b**, such as spleen, heart, kidney, and lung, was reduced to background levels, indicating near complete displacement and reversible binding in healthy



tissue. Organs that exhibited low to moderate accumulation of  $^{18}\text{F}$ -**6b** without displacement, such as muscle or liver, were essentially unchanged with displacement, suggesting that the low to moderate tracer accumulation in these tissues may reflect non-specificity. Interestingly, activity found in the urine did not follow this trend and was elevated with displacement, suggesting that blocking TSPO with non-radioactive **6b** altered the excretion profile of the agent. Overall, the results indicate a high degree of specific binding and reversibility of  $^{18}\text{F}$ -**6b** to TSPO in healthy tissues.



## Crystallography



**6b** was recrystallized from hot acetonitrile and ethanol (95%) by slow evaporation at room temperature and characterized by diffractometry. **6b** demonstrated two ethyl branches at the 5- and 7-positions of the pyrazolopyrimidine ring, corresponding to the structure elucidated from NMR spectroscopy. The crystal structure also revealed three distinct planar entities, the pyrazolopyrimidine ring, the phenyl ring, and the amide group (**Figure 5.4**).

#### 5.4 Conclusion

In this study, we found that the 5,6,7-substitution pattern is a critical determinant of TSPO affinity among pyrazolopyrimidines. Experiments shown here led to the discovery of VUIIS1008 (**6b**), a TSPO ligand exhibiting significantly increased affinity compared to DPA-714 (**6a**) and TSPO ligands derived from other chemical entities.<sup>70</sup> Furthermore, in addition to improved TSPO affinity, compound **6b** was TSPO-selective, exhibiting negligible binding affinity to CBR. VUIIS1008 analog **7** could be radiolabeled with 18-fluorine to yield <sup>18</sup>F-VUIIS1008 (**<sup>18</sup>F-6b**). Suggesting its potential as a probe for cancer imaging, preclinical imaging studies demonstrated robust accumulation of **<sup>18</sup>F-6b** in tumor tissue and negligible accumulation in normal brain. Furthermore, we observed improved *in vivo* stability of **<sup>18</sup>F-6b** compared to <sup>18</sup>F-DPA-714.<sup>37</sup> Overall, these studies illuminate **<sup>18</sup>F-6b** as a promising, novel PET ligand for evaluating TSPO expression in tumors and potentially other diseases.

## 5.5 Results and Methods

**General information** All commercially available reagents were used without further purification. Microwave reactions were carried out with a Biotage Initiator™ Sixty microwave system (Uppsala, Sweden). Reaction residues were purified using a CombiFlash purification system (TELEDYNE ISCO) with silica cartridges. <sup>1</sup>H- and <sup>13</sup>C-NMR spectra were recorded on a Bruker 400 MHz spectrometer in the Vanderbilt Small Molecule NMR Facility. Chemical shifts are reported in ppm using the residual of chloroform as the internal standard (7.26 ppm for <sup>1</sup>H and 77.160 ppm for <sup>13</sup>C, respectively). The following abbreviations are used: s = singlet, d = doublet, t = triplet, q = quartet and m = multiplet. All CH/CHN elemental analyses were performed by Atlantic Microlab, INC (Norcross, GA, USA). High-resolution mass spectra were acquired with a Waters Synapt hybrid quadrupole/oa-QToF mass spectrometer equipped with a dual channel ES-Cl source.

### **3-Cyano-*N,N*-diethyl-4-(4-methoxyphenyl)-4-oxobutanamide (3)**

To a solution of 3-(4-methoxyphenyl)-3-oxopropanenitrile (1.0 g, 5.71 mmol, 1) and 2-chloro-*N,N*-diethylacetamide (0.854 g, 5.71 mmol, 2) in 80% EtOH (40 mL) were added NaOH (0.22 g, 5.71 mmol) and KI (2.84 g, 17.1 mmol). The mixture was microwaved at 80 °C for 40 min. The reaction was monitored by TLC (hexane/ethyl acetate = 50/50, v/v). When completed, the mixture was filtered and extracted with CH<sub>2</sub>Cl<sub>2</sub>. The residue was concentrated and purified by flash

chromatography on silica gel (hexane/ethyl acetate = 50/50, v/v) to afford **3** (1.14 g, 70%) as a brown oil. [Found: C, 62.06; H, 6.59; N, 8.56. C<sub>16</sub>H<sub>20</sub>N<sub>2</sub>NaO<sub>3</sub> requires C, 61.73; H, 6.48; N, 9.00%]. <sup>1</sup>H-NMR (CDCl<sub>3</sub>, 400 MHz) δ 8.05 (d, 2H, J = 8.8 Hz), 6.85 (d, 2H, J = 8.8 Hz), 5.00 (dd, 1H, J = 9.2 Hz, 4.5 Hz), 3.89 (s, 3H), 3.39 (m, 4H), 3.33 (m, 1H), 2.86 (m, 1H), 1.28 (t, 3H, J = 7.2 Hz), 1.09 (t, 3H, J = 7.2 Hz). <sup>13</sup>C-NMR (CDCl<sub>3</sub>, 400 MHz) δ 187.7, 167.1, 164.5, 131.4, 127.1, 117.5, 114.2, 55.5, 41.9, 40.6, 33.6, 32.5, 14.05, 12.9. HRMS calcd for C<sub>16</sub>H<sub>20</sub>N<sub>2</sub>O<sub>3</sub>Na m/z = 311.1372 (M + Na)<sup>+</sup>, found 311.1381.

#### **2-(3-amino-5-(4-methoxyphenyl)-1H-pyrazol-4-yl)-N,N-diethylacetamide (4)**

To a solution of **3** (1.14 g, 3.95 mmol) in EtOH (18 mL) were added hydrazine (0.126 g, 3.95 mmol) and AcOH (0.13 mL). The mixture was irradiated at 90 °C for 40 min in a Biotage Initiator. The reaction was monitored with TLC (CH<sub>2</sub>Cl<sub>2</sub>/MeOH = 90/10, v/v). When completed, the residue was washed with saturated aqueous Na<sub>2</sub>CO<sub>3</sub> (50 mL) and extracted with CH<sub>2</sub>Cl<sub>2</sub> (50 mL). The organic layer was collected and concentrated *in vacuo*. Purification of the residue with flash chromatography on silica gel (CH<sub>2</sub>Cl<sub>2</sub>/MeOH = 100/0-90/10, v/v) afforded **4** (0.5 g, 42%) as yellow crystals. [Found: C, 58.60; H, 6.59; N, 16.90. C<sub>16</sub>H<sub>22</sub>N<sub>4</sub>NaO<sub>2</sub> requires C, 59.06, H, 6.82, N, 17.22%]. <sup>1</sup>H-NMR (CDCl<sub>3</sub>, 400 MHz) δ 7.32 (d, 2H, J = 8.8 Hz), 6.97 (d, 2H, J = 8.8 Hz), 3.85 (s, 3H), 3.51 (s, 2H), 3.32 (m, 2H), 3.06 (m, 2H), 1.08 (t, 3H, J = 7.2 Hz), 0.93 (t, 3H, J = 7.2 Hz). <sup>13</sup>C-NMR (CDCl<sub>3</sub>, 400 MHz) δ 170.2, 159.8, 129.0, 126.6, 122.8, 114.3, 55.3,

42.3, 40.4, 28.5, 14.0, 13.0. HRMS calcd for C<sub>16</sub>H<sub>23</sub>N<sub>2</sub>O<sub>2</sub> m/z = 303.1821 (MH<sup>+</sup>), found 303.1814.

***N,N*-diethyl-2-(2-(4-methoxyphenyl)-5,7-dimethylpyrazolo[1,5-*a*]pyrimidin-3-yl)acetamide (5a, DPA-713)**

To a solution of **4** (0.05 g, 0.165 mmol) in EtOH (8.0 mL) was added 2,4-pentanedione (0.0165 g, 0.165 mmol). The mixture was irradiated with a Biotage Initiator at 180 °C for 45 min. The reaction was monitored by TLC (CH<sub>2</sub>Cl<sub>2</sub>/MeOH = 90/10, v/v). Following the reaction, the residue was concentrated in vacuo and purified with flash chromatography (CH<sub>2</sub>Cl<sub>2</sub>/MeOH = 100/0-90/10, v/v) to afford **5** (0.055 g, 91%) as brown crystals. [Found: C, 68.61; H, 6.98; N, 15.11. C<sub>21</sub>H<sub>26</sub>N<sub>4</sub>O<sub>2</sub> requires C, 68.83; H, 7.15; N, 15.29%] <sup>1</sup>H-NMR (CDCl<sub>3</sub>, 400 MHz) δ 7.78 (d, 2H, J = 8.8 Hz), 6.99 (d, 2H, J = 8.8 Hz), 6.50 (s, 1H), 3.92 (s, 2H), 3.85 (s, 3H), 3.50 (m, 2H), 3.41 (m, 2H), 2.74 (s, 3H), 2.54 (s, 3H), 1.20 (t, 3H, J = 7.2 Hz), 1.12 (t, 3H, J = 7.2 Hz). <sup>13</sup>C-NMR (CDCl<sub>3</sub>, 400 MHz) δ 170.0, 159.7, 157.3, 154.9, 147.6, 144.6, 129.9, 126.3, 113.8, 108.0, 100.7, 55.2, 42.2, 40.5, 28.1, 24.6, 16.8, 14.3, 13.0. HRMS calcd for C<sub>21</sub>H<sub>26</sub>N<sub>4</sub>O<sub>2</sub>Na m/z = 389.1953 (M + Na)<sup>+</sup>, found 389.1940.

**2-(5,7-diethyl-2-(4-methoxyphenyl)pyrazolo[1,5-*a*]pyrimidin-3-yl)-*N,N*-diethylacetamide (5b)**

This compound was prepared from **4** with 3,5-hexanedione using the same method as **5a**. [Found: C, 65.35; H, 7.30; N, 12.22. C<sub>23</sub>H<sub>30</sub>N<sub>4</sub>O<sub>2</sub> requires C, 70.02; H, 7.66; N, 14.20%] <sup>1</sup>H-NMR (CDCl<sub>3</sub>, 400 MHz) δ 7.68 (d, 2H, J = 8.8 Hz), 7.00 (d, 2H, J = 8.8 Hz), 6.61 (s, 1H), 4.01 (s, 2H), 3.86 (s, 3H), 3.50 (m, 2H), 3.42 (m, 2H), 3.26 (m, 2H), 2.94 (m, 2H), 1.47 (t, 3H, J = 7.48 Hz), 1.37 (t, 3H, J = 7.6 Hz), 1.21 (t, 3H, J = 7.2 Hz), 1.13 (t, 3H, J = 7.08). <sup>13</sup>C-NMR (CDCl<sub>3</sub>, 400 MHz) δ 170.3, 159.6, 156.9, 154.0, 145.9, 141.7, 129.9, 126.5, 119.9, 113.9, 100.3, 55.2, 42.2, 40.5, 28.0, 23.3, 21.3, 14.3, 14.1, 13.0, 12.9. HRMS calcd for C<sub>23</sub>H<sub>30</sub>N<sub>4</sub>O<sub>2</sub>, m/z = 385.2447 (MH<sup>+</sup>), found 385.2436.

**2-(5,7-diisopropyl-2-(4-methoxyphenyl)pyrazolo[1,5-a]pyrimidin-3-yl)-N,N-diethylacetamide (5c)**

This compound was prepared from **4** with 2,6-dimethyl-3,5-heptanedione using the same method as **5a**. <sup>1</sup>H-NMR (CDCl<sub>3</sub>, 400 MHz) δ 7.89 (d, 2H, J = 8.8 Hz), 7.00 (d, 2H, J = 8.8 Hz), 6.50 (s, 1H), 3.93 (s, 2H), 3.89 (m, 1H), 3.86 (s, 3H), 3.62 (m, 2H), 3.41 (m, 2H), 3.04 (m, 1H), 1.44 (d, 6H, J = 6.8 Hz), 1.32 (d, 6H, J = 6.8 Hz), 1.22 (t, 3H, J = 7.2 Hz), 1.11 (t, 3H, J = 7.2 Hz). <sup>13</sup>C-NMR (CDCl<sub>3</sub>, 400 MHz) δ 170.6, 165.9, 159.7, 154.7, 154.1, 147.5, 126.5, 113.8, 101.7, 100.7, 55.2, 42.5, 40.7, 36.4, 28.1, 28.0, 20.0, 14.4, 13.1. HRMS calcd for C<sub>25</sub>H<sub>34</sub>N<sub>4</sub>O<sub>2</sub>, m/z = 423.2760 (MH<sup>+</sup>), found 423.2762.

***N,N*-diethyl-2-(2-(4-methoxyphenyl)-5,6,7-trimethylpyrazolo[1,5-a]pyrimidin-3-yl)acetamide (5d)**

This compound was prepared with **4** and 3-methyl-2,4-pentanedione using the same method as **5a**. <sup>1</sup>H-NMR (CDCl<sub>3</sub>, 400 MHz) δ 7.56 (d, 2H, J = 7.2 Hz), 7.01 (d, 2H, J = 7.2 Hz), 4.08 (s, 2H), 3.87 (s, 3H), 3.44 (m, 4H), 2.96 (s, 3H), 2.78 (s, 3H), 2.39 (s, 3H), 1.33 (t, 3H, J = 7.2 Hz), 1.16 (t, 3H, J = 7.1 Hz). HRMS calcd for C<sub>22</sub>H<sub>28</sub>N<sub>4</sub>O<sub>2</sub>, m/z = 381.2291 (MH<sup>+</sup>), found 381.2295.

***N,N*-diethyl-2-(6-ethyl-2-(4-methoxyphenyl)-5,7-dimethylpyrazolo[1,5-a]pyrimidin-3-yl)acetamide (5e)**

This compound was prepared with **4** and 3-ethyl-2,4-pentanedione using the same method as **5a**. <sup>1</sup>H-NMR (CDCl<sub>3</sub>, 400 MHz) δ 7.56 (d, 2H, J = 8.8 Hz), 7.01 (d, 2H, J = 8.8 Hz), 4.07 (s, 2H), 3.87 (s, 3H), 3.44 (m, 4H), 2.95 (s, 3H), 2.82 (m, 2H), 2.81 (s, 3H), 1.25 (m, 6H), 1.15 (t, 3H, 7.1 Hz). HRMS calcd for C<sub>23</sub>H<sub>30</sub>N<sub>4</sub>O<sub>2</sub>, m/z = 395.2447 (MH<sup>+</sup>), found 395.2448.

**2-(6-acetyl-2-(4-methoxyphenyl)-5,7-dimethylpyrazolo[1,5-a]pyrimidin-3-yl)-*N,N*-diethylacetamide (5f)**

This compound was prepared with **4** and triacetylmethane using the same method as **5a**. <sup>1</sup>H-NMR (CDCl<sub>3</sub>, 400 MHz) δ 7.67 (d, 2H, J = 8.8 Hz), 7.00 (d, 2H, J = 8.8 Hz), 3.98 (s, 2H), 3.87 (s, 3H), 3.49 (m, 2H), 3.43 (m, 2H), 2.78 (s, 3H),

2.60 (s, 3H), 2.55 (s, 3H), 1.23 (t, 3H, J = 7.16), 1.13 (t, 3H, 7.1 Hz). HRMS calcd for C<sub>23</sub>H<sub>28</sub>N<sub>4</sub>O<sub>2</sub>, m/z = 409.2240 (MH<sup>+</sup>), found 409.2241.

**2-(6-chloro-2-(4-methoxyphenyl)-5,7-dimethylpyrazolo[1,5-a]pyrimidin-3-yl)-N,N-diethylacetamide (5g)**

This compound was prepared with **4** and 3-chloro-2,4-pentanedione via the same method as **5a**. <sup>1</sup>H-NMR (CDCl<sub>3</sub>, 400 MHz) δ 7.72 (d, 2H, J = 8.8 Hz), 7.00 (d, 2H, J = 8.8 Hz), 3.94 (s, 2H), 3.87 (s, 3H), 3.49 (m, 2H), 3.43 (m, 2H), 2.91 (s, 3H), 2.66 (s, 3H), 1.23 (t, 3H, J = 7.16), 1.13 (t, 3H, 7.1 Hz). HRMS calcd for C<sub>21</sub>H<sub>25</sub>ClN<sub>4</sub>O<sub>2</sub>, m/z = 401.1744 (MH<sup>+</sup>), found 401.1747.

**N,N-diethyl-2-(2-(4-(2-fluoroethoxy)phenyl)-5,7-dimethylpyrazolo[1,5-a]pyrimidin-3-yl)acetamide (6a, DPA-714)**

To a solution of **5** (55 mg, 0.15 mmol) in aqueous HBr (4 mL) was added HTPB (8.0 mg, 0.015 mmol). The reaction mixture was irradiated with a Biotage Initiator at 110 °C for 40 min. The reaction was monitored by TLC (CH<sub>2</sub>Cl<sub>2</sub>/MeOH = 90/10, v/v). When completed, the mixture was washed with saturated aqueous NaHCO<sub>3</sub> (50 mL) and extracted with CH<sub>2</sub>Cl<sub>2</sub> (50 mL x 2). The organic layer was collected and concentrated in vacuo. The crude product was then added to a suspension of NaH (7.4 mg, 0.30 mmol) in dry THF (4.0 mL). The reaction mixture was stirred for 10 min at 0 °C and then allowed to warm to room temperature before addition of a solution of 2-fluoroethyl-4-

methylbenzenesulfonate (100 mg, 0.46 mmol) in dry THF (2.0 mL). The mixture was irradiated at 120 °C for 30 min with a Biotage Initiator. The reaction was monitored with TLC (CH<sub>2</sub>Cl<sub>2</sub>/MeOH = 95/5, v/v). When complete, the reaction residue was partitioned between aqueous 1.0 M HCl (50 mL) and CH<sub>2</sub>Cl<sub>2</sub> (50 mL). The organic layer was collected and concentrated in vacuo. Final purification of the residue using a Gilson HPLC afforded **6** (40 mg, 64%) as white crystals. [Found: C, 66.56; H, 6.94. C<sub>22</sub>H<sub>27</sub>FN<sub>4</sub>O<sub>2</sub> requires C, 66.31; H, 6.83%]. <sup>1</sup>H-NMR (CDCl<sub>3</sub>, 400 MHz) δ 7.68 (d, 2H, J = 8.8 Hz), 7.02 (d, 2H, J = 8.8 Hz), 6.58 (s, 1H), 4.85 (t, 1H, 4.2Hz), 4.73 (t, 1H, 4.2Hz) 4.30 (t, 1H, 4.4Hz), 4.23 (t, 1H, 4.4Hz), 3.98 (s, 2H), 3.47 (m, 2H), 3.42 (m, 2H), 2.79 (s, 3H), 2.62 (s, 3H), 1.21 (t, 3H, J = 7.2 Hz), 1.12 (t, 3H, J = 7.2 Hz). <sup>13</sup>C-NMR (CDCl<sub>3</sub>, 400 MHz) δ 170.1, 158.9, 157.8, 155.8, 147.04, 145.70, 130.0, 126.0, 114.7, 108.1, 100.2, 82.64, 80.95, 67.2, 67.0, 42.31, 40.91, 27.9, 23.3, 17.0, 14.0, 12.8. HRMS calcd for C<sub>22</sub>H<sub>27</sub>FN<sub>4</sub>O<sub>2</sub>Na m/z = 421.2016 (M + Na)<sup>+</sup>, found 421.2006.

**2-(5,7-diethyl-2-(4-(2-fluoroethoxy)phenyl)pyrazolo[1,5-a]pyrimidin-3-yl)-*N,N*-diethylacetamide (6b, VUIIS1008)**

This compound was prepared with **5b** via the same method as **6a**. <sup>1</sup>H-NMR (CDCl<sub>3</sub>, 400 MHz) δ 7.80 (d, 2H, J = 8.8 Hz), 7.02 (d, 2H, J = 8.8 Hz), 6.54 (s, 1H), 4.85 (t, 1H, 4.2 Hz), 4.73 (t, 1H, J = 4.3 Hz) 4.31 (t, 1H, J = 4.2 Hz), 4.23 (t, 1H, J = 4.2 Hz), 3.95 (s, 2H), 3.54 (m, 2H), 3.41 (m, 2H), 3.21 (m, 2H), 2.86 (m, 2H), 1.45 (t, 3H, J = 7.2 Hz), 1.34 (t, 3H, J = 7.2 Hz), 1.20 (t, 3H, J = 7.2 Hz), 1.11 (t, 3H, J = 7.2 Hz). <sup>13</sup>C-NMR (CDCl<sub>3</sub>, 400 MHz) δ 170.40, 162.40, 158.60,



154.91, 150.36, 146.97, 130.05, 126.76, 114.61, 104.80, 100.55, 82.69, 80.99, 67.17, 66.96, 42.40, 40.74, 31.01, 27.98, 23.30, 14.22, 12.94, 12.84, 10.21. HRMS calcd for C<sub>24</sub>H<sub>31</sub>FN<sub>4</sub>O<sub>2</sub> m/z = 427.2509 (MH<sup>+</sup>), found 427.2500.

***N,N*-diethyl-2-(2-(4-(2-fluoroethoxy)phenyl)-5,7-diisopropylpyrazolo[1,5-a]pyrimidin-3-yl)acetamide (6c)**

This compound was prepared with **5c** via the same method as **6a**. <sup>1</sup>H-NMR (CDCl<sub>3</sub>, 400 MHz) δ 7.91 (d, 2H, J = 8.8 Hz), 7.02 (d, 2H, J = 8.8 Hz), 6.50 (s, 1H), 4.85 (t, 1H, J = 4.3 Hz), 4.73 (t, 1H, J = 4.3 Hz), 4.31 (t, 1H, J = 4.2 Hz), 4.23 (t, 1H, J = 4.2 Hz), 3.93 (s, 2H), 3.88 (m, 1H), 3.63 (m, 2H), 3.41 (m, 2H), 3.05 (m, 1H), 1.44 (d, 6H, J = 5.6 Hz), 1.33 (d, 6H, J = 5.6 Hz), 1.23 (t, 3H, J = 7.1 Hz), 1.11 (t, 3H, J = 7.1 Hz). HRMS calcd for C<sub>26</sub>H<sub>35</sub>FN<sub>4</sub>O<sub>2</sub> m/z = 455.2822 (MH<sup>+</sup>), found 455.2815.

***N,N*-diethyl-2-(2-(4-(2-fluoroethoxy)phenyl)-5,6,7-trimethylpyrazolo[1,5-a]pyrimidin-3-yl)acetamide (6d)**

This compound was prepared with **5e** via the same method as **6a**. <sup>1</sup>H-NMR (CDCl<sub>3</sub>, 400 MHz) δ 7.66 (d, 2H, J = 8.8 Hz), 7.02 (d, 2H, J = 8.8 Hz), 4.85 (t, 1H, J = 4.2 Hz), 4.73 (t, 1H, J = 4.3 Hz), 4.31 (t, 1H, J = 4.2 Hz), 4.23 (t, 1H, J = 4.1 Hz), 4.00 (s, 2H), 3.44 (m, 4H), 2.87 (s, 3H), 2.67 (s, 3H), 2.34 (s, 3H), 1.20 (s, 3H), 1.12 (t, 3H, J = 7.2 Hz). HRMS calcd for C<sub>23</sub>H<sub>29</sub>FN<sub>4</sub>O<sub>2</sub> m/z = 413.2353 (MH<sup>+</sup>), found 413.2349.

***N,N*-diethyl-2-(6-ethyl-2-(4-(2-fluoroethoxy)phenyl)-5,7-dimethylpyrazolo[1,5-a]pyrimidin-3-yl)acetamide (6e)**

This compound was prepared with **5f** via the same method as **6a**. <sup>1</sup>H-NMR (CDCl<sub>3</sub>, 400 MHz) δ 7.78 (d, 2H, J = 8.8 Hz), 7.01 (d, 2H, J = 8.8 Hz), 4.84 (t, 1H, J = 4.2 Hz), 4.72 (t, 1H, J = 4.2 Hz), 4.30 (t, 1H, J = 4.2 Hz), 4.23 (t, 1H, J = 4.2 Hz), 3.92 (s, 2H), 3.51 (m, 2H), 3.41 (m, 2H), 2.79 (s, 3H), 2.73 (m, 2H), 2.60 (s, 3H), 1.20 (m, 6H), 1.12 (d, 3H, J = 8.5 Hz). HRMS calcd for C<sub>24</sub>H<sub>31</sub>FN<sub>4</sub>O<sub>2</sub> m/z = 427.2509 (MH<sup>+</sup>), found 427.2496.

**2-(6-acetyl-2-(4-(2-fluoroethoxy)phenyl)-5,7-dimethylpyrazolo[1,5-a]pyrimidin-3-yl)-*N,N*-diethylacetamide (6f)**

This compound was prepared with **5g** via the same method as **6a**. <sup>1</sup>H-NMR (CDCl<sub>3</sub>, 400 MHz) δ 7.77 (d, 2H, J = 8.8 Hz), 7.02 (d, 2H, J = 8.8 Hz), 4.85 (t, 1H, J = 4.2 Hz), 4.73 (t, 1H, J = 4.2 Hz), 4.31 (t, 1H, J = 4.2 Hz), 4.24 (t, 1H, J = 4.2 Hz), 3.92 (s, 2H), 3.52 (m, 2H), 3.43 (m, 2H), 2.76 (s, 3H), 2.59 (s, 3H), 2.53 (s, 3H), 1.25 (t, 3H, J = 7.2 Hz), 1.13 (t, 3H, J = 7.2 Hz). HRMS calcd for C<sub>24</sub>H<sub>29</sub>FN<sub>4</sub>O<sub>3</sub> m/z = 441.2302 (MH<sup>+</sup>), found 441.2295.

**2-(6-chloro-2-(4-(2-fluoroethoxy)phenyl)-5,7-dimethylpyrazolo[1,5-a]pyrimidin-3-yl)-*N,N*-diethylacetamide (6g)**

This compound was prepared with **5h** via the same method as **6a**. <sup>1</sup>H-NMR (CDCl<sub>3</sub>, 400 MHz) δ 7.79 (d, 2H, J = 8.8 Hz), 7.02 (d, 2H, J = 8.8 Hz), 4.84 (t, 1H, J = 4.2 Hz), 4.72 (t, 1H, J = 4.2 Hz), 4.30 (t, 1H, J = 4.2 Hz), 4.23 (t, 1H, J = 4.1 Hz), 3.90 (s, 2H), 3.51 (m, 2H), 3.42 (m, 2H), 2.91 (s, 3H), 2.65 (s, 3H), 1.23 (t, 3H, J = 7.2 Hz), 1.12 (t, 3H, J = 7.2 Hz). HRMS calcd for C<sub>22</sub>H<sub>26</sub>ClFN<sub>4</sub>O<sub>2</sub> m/z = 433.1807(MH<sup>+</sup>), found 433.1790.

**2-(4-(3-(2-(diethylamino)-2-oxoethyl)-5,7-diethylpyrazolo[1,5-a]pyrimidin-2-yl)phenoxy)ethyl 4-methylbenzenesulfonate (7)**

To a solution of **5** (260 mg, 0.66 mmol) in aqueous HBr (20 mL) was added hydroxyl-terminated polybutadiene (HTPB) (35.5 mg, 0.07 mmol). The reaction mixture was irradiated with microwaves at 110 °C for 40 min. The reaction was monitored by TLC (CH<sub>2</sub>Cl<sub>2</sub>/MeOH = 90/10, v/v). When complete, the mixture was washed with saturated aqueous NaHCO<sub>3</sub> (100 mL) and extracted with CH<sub>2</sub>Cl<sub>2</sub> (50 mL x 3). The organic layer was collected and concentrated in vacuo. The crude product was then added to a suspension of NaH (17 mg, 0.71 mmol) in dry THF (10.0 mL). The reaction mixture was stirred for 10 min at 0 °C and then allowed to warm to room temperature before addition of a solution of 2-fluoroethyl-4-methylbenzenesulfonate (366 mg, 0.99 mmol) in dry THF (5.0 mL). The mixture was irradiated at 120 °C for 30 min with a Biotage Initiator. The reaction was monitored with TLC (CH<sub>2</sub>Cl<sub>2</sub>/MeOH = 95/5, v/v). When complete, the reaction residue was partitioned between aqueous 1.0 M HCl (50 mL) and

CH<sub>2</sub>Cl<sub>2</sub> (50 mL). The organic layer was collected, dried over MgSO<sub>4</sub> and concentrated in vacuo. Final purification of the residue on a CombiFlash (TELEDYNE ISO) afforded **7** (170 mg, 45%) as yellow crystals. <sup>1</sup>H-NMR (CDCl<sub>3</sub>, 400 MHz) δ 7.83 (d, 4H, 8.5 Hz), 7.36 (d, 2H, J = 8.0 Hz), 6.86 (d, 2H, J = 8.8 Hz), 6.50 (s, 1H), 4.40 (t, 2H, J = 5.0 Hz), 4.19 (t, 2H, 4.6 Hz), 3.91 (s, 2H), 3.57 (m, 2H), 3.41 (m, 2H), 3.19 (m, 2H), 2.83 (m, 2H), 2.45 (s, 3H), 1.44 (t, 3H, J = 7.5 Hz), 1.34 (t, 3H, 7.6 Hz), 1.22 (t, 3H, 7.1 Hz), 1.11 (t, 3H, 7.1 Hz). <sup>13</sup>C-NMR (CDCl<sub>3</sub>, 400 MHz) δ 170.27, 162.20, 158.05, 154.54, 149.62, 147.52, 144.91, 132.81, 129.99, 129.81, 127.96, 127.19, 114.47, 104.87, 100.77, 68.04, 65.34, 42.38, 40.60, 31.33, 27.99, 23.22, 21.59, 14.34, 13.04, 12.76, 10.25.

### Measurement of Log P<sub>7.5</sub>

The lipophilicity of each library entrant was examined by determination of the log P<sub>7.5</sub> value using a HPLC method previously described.<sup>66</sup> Samples were analyzed using a C18 Dynamax column (Varian, 250 x 4.6 mm) and a mobile phase of MeOH and phosphate buffer (85/15, v/v, pH = 7.5) with a flow rate of 1.0 mL/min. The lipophilicity of each ligand was estimated by comparison of retention time to that of standards having known log P values. The standards used were catechol, aniline, benzene, bromobenzene, ethyl benzene, trimethylbenzene, and hexachlorobenzene, each dissolved in an appropriate solvent. All sample injections were done in triplicate and the results averaged to provide the final values. Relative retention times, RRT (to catechol), were

calculated, and a calibration curve of log P versus log RRT was generated. The calibration equations were polynomial with an  $r^2$  of 0.994 or greater.

### **X-Ray Crystallography**

A crystal of VUIIS1008 (**6b**) was mounted on a glass fiber and maintained at 100 K during data collection. Data collection was done using an Agilent Technologies Xcalibur PX2 Ultra with a sealed-tube copper X-ray source and an ONYX CCD area detector. Data reduction was done using Chrysalis software (Agilent Technologies). The data were phased using SIR2011.

### **Radiosynthesis**

$^{18}\text{F}$ -VUIIS1008 ( **$^{18}\text{F}$ -6b**) and radioligand precursor (**7**) were prepared according to our published methods.<sup>22</sup> In brief, using a commercial apparatus (TRACERlab FX F-N; GE Healthcare), we dried aqueous  $^{18}\text{F}$ -fluoride ion (~3 Ci/111 GBq) by iterative cycles of addition and evaporation of acetonitrile, followed by complexation with  $\text{K}^+ \text{-K}_{2.2.2}/\text{K}_2\text{CO}_3$ . The complex was then reacted with 2-(4-(3-(2-(diethylamino)-2-oxoethyl)-5,7-diethylpyrazolo[1,5-a]pyrimidin-2-yl)phenoxy)ethyl 4-methylbenzenesulfonate (**7**) (4.0 mg) at 99 °C for 20 min in anhydrous dimethyl sulfoxide (0.6 mL).  **$^{18}\text{F}$ -6b** was purified using reversed-phase high-performance liquid chromatography (C18, Dynamax 250 x 21.4 mm; Varian), eluting at 6.0 mL/min with 10 mM  $\text{NaH}_2\text{PO}_4$  buffer (pH 6.7) and ethanol

(47.5/52.5, v/v). **<sup>18</sup>F-6b** was collected directly into 140 mL of water (deionized), passed through a C-18 Sep-Pak (Waters) followed by sequential elution with 200 proof ethanol (1.0 mL) and saline (9.0 mL) into a sterile vial. Typical specific activities were 4203 Ci/mmol (156 TBq/mmol) or greater.

The radiotracer preparation was visually inspected for clarity, absence of color, and particulates. Specific activity of the radiotracer was calculated from 33 individual radiolabeling processes based on HPLC chromatography. The specific radioactivity was determined as follows: a known amount of radioactive product was injected and the area of the UV absorbance peak corresponding to the radiolabelled product was determined (integration value) from the HPLC chromatogram. This value was then compared with a standard curve, generated from nonradioactive **6b**, relating mass to UV absorbance. The quotient of activity injected and mass gave the specific activity value.

### ***In vitro* TSPO-Binding Assay**

C6 cells were collected and washed with PBS buffer three times, and then frozen and thawed three times in lysis buffer (5.0 mM HEPES, 0.21 M D-mannitol, 0.07 M sucrose, 2.0 mM benzamidine, 2.0 mM toluenesulfonyl fluoride, 4.0 mM MgCl<sub>2</sub>, pH 7.4) to produce C6 cell lysate (0.5 mg/mL). The obtained C6 cell lysate (0.3 mL) was then incubated with <sup>3</sup>H-PK 11195 (final concentration 0.6 nM) (Perkin Elmer, Waltham, MA, USA) and TSPO ligands (**Table 5.1**) (10<sup>-5</sup> to 10<sup>-12</sup> M) in a total volume of 1.0 mL for 2 h at 25 °C. The reaction was

terminated by rapid filtration through a Brandel harvester (Gaithersburg, MD, USA) and collection onto a filter presoaked with 0.3% polyethyleneimine. Filters were then punched out into scintillation vials and bound radioactivity measured on a Beckman LS 6000 Scintillation Counter (Brea, California, USA). Binding affinity ( $K_i$ ) was calculated using Prism GraphPad (La Jolla, CA, USA) using 5 nM as the  $K_d$  for PK 111 95 and a radioligand concentration of 0.6 nM.

### ***In vitro* CBR-Binding Assay**

Male Wistar rats were decapitated and the cerebral cortex collected and dissected. The cerebral cortex was homogenized in 20 volumes of ice-cold PBS buffer (pH 7.4) with a Brinkmann microhomogenizer (Kinematica AG, Luzern, SW). The homogenate was collected at a protein concentration of 5.0 mg/mL and stored at -80 °C. The crude cerebral cortex preparation (0.3 mL) was incubated with  $^3\text{H}$ -flunitrazepam (final concentration 0.6 nM) (Perkin Elmer) and VUHS1008 (**6b**) ( $10^{-5}$  to  $10^{-7}\text{M}$ ) in a total volume of 1.0 mL for 2 h at 25 °C. The reaction was terminated by rapid filtration through a Brandel harvester and collection onto a filter presoaked with 0.3% polyethyleneimine. Filters were then punched out into scintillation vials and bound radioactivity measured on a Beckman LS 6000 Scintillation Counter.

### **Rat Model**

All studies involving animals were conducted in compliance with federal and institutional guidelines. Two weeks before imaging, healthy male Wistar rats were stereotactically inoculated in the right hemisphere with  $1.0 \times 10^5$  C6 glioma cells (American Type Tissue Collection). Prior to imaging, all rats were affixed with venous and arterial catheters.

## **MRI**

MRI was used to localize C6 tumors. Rats were secured prone in a radiofrequency coil (38-mm inner diameter) and placed in a 4.7-T horizontal bore imaging system (Varian Inc., Palo Alto, CA, USA). A constant body temperature of 37 °C was maintained using heated airflow. An initial multislice gradient-echo imaging sequence (repetition time, 150 ms; echo time, 3.5 ms; matrix, 128 x 128; field of view, 40 x 40 mm<sup>2</sup>; slice thickness, 2 mm) was used to acquire 7 slices in each imaging plane (axial, coronal, sagittal) for proper positioning of subsequent scans. A multislice T<sub>2</sub>-weighted fast spin-echo scan with 8 echoes and 8.0-ms echo spacing (effective echo time, 32 ms) was then collected with a repetition time of 2,000 ms; field of view of 32 x 32 mm<sup>2</sup>; matrix of 128 × 128; 16 acquisitions; and 8 coronal slices of 2-mm thickness.

## **PET/CT**



PET/CT was performed within 24 hours of MRI in rats with confirmed tumors. Tumor-bearing rats were administered **<sup>18</sup>F-6b** via jugular catheter while in a microPET Focus 220 scanner (Siemens, Munich, DE). Data were collected in list-mode format for 90 minutes, followed by a CT scan (microCAT II; Siemens) for attenuation correction. For reconstruction, the dynamic PET acquisition was divided into twelve 10-s frames for the first two minutes, three 60-second frames for the following three minutes, and seventeen 300-second frames for the duration of the scan. The raw data within each frame were then binned into three-dimensional sinograms, with a span of three and ring difference of 47. The sonograms were reconstructed into tomographic images (128 x 128 x 95) with voxel sizes of 0.095 x 0.095 x 0.08 cm<sup>3</sup>, after scatter and attenuation corrections were applied, using a two-dimensional ordered-subsets expectation-maximization algorithm with 16 subsets and four iterations. Attenuation correction was accomplished by generating an attenuation map from the CT images. The CT image was first coregistered with the small animal PET image, segmented, and then projected into sonogram space with a span of 47 and ring difference of 23. Time-activity curves were generated by manually drawing 3-dimensional volumes of interest over tumor and contralateral brain using ASIPro (Siemens).

### **HPLC Radiometabolite Analysis**

Arterial blood (200 µL) was collected at 2, 12, 30, 60, and 90 min following injection of 1.5 mCi of **<sup>18</sup>F-6b**. After centrifugation, the plasma was extracted with

acetonitrile/water (340  $\mu$ L, 7/1, v/v). The mixture was then centrifuged and the supernatant used for reversed-phase HPLC analysis with 0.1 M aqueous ammonium acetate ( $\text{NH}_4\text{OAc}$ ) (pH 10) and acetonitrile (30/70, v/v) at 1.0 mL/min on a C18 Dynamax 250 x 4.6 mm column (Varian). Radiochromatographic data were recorded and collected using a radioisotope detector (Bioscan, Washington, DC, USA).

## **Histology**

Whole brains were harvested and fixed in 4% formalin for 48 hours, followed by paraffin embedding for immunohistochemistry. Tissue sections of 5.0- $\mu$ m thickness were taken and stained with TSPO-specific rabbit polyclonal antibody, a gift from Professor Vassilios Papadopoulos of McGill University. Immunoreactivity was assessed using a horseradish peroxidase detection kit (Dako, Glostrup, DK). Hematoxylin and eosin staining was used to evaluate cell density and tumor localization.

## **Biodistribution**

Fourteen different tissue samples were collected for the biodistribution study 60 minutes of 1.0 – 1.5 mCi of  $^{18}\text{F}$ -**6b** injection. Tissues included brain, liver, spleen, heart, blood, kidney, lung, colon, small bowel, stomach, testes, skull, muscle, and urine. For rats with displacement, **6b** (10 mg/kg) was injected 30

minutes after **<sup>18</sup>F-6b** injection. Radioactivity of the samples was determined with a NaI well counter (Capintec, Ramsey, NJ, USA). %ID/g value of each sample was calculated according to the weight and radioactivity of the samples.

## CHAPTER 6

### QUANTITATIVE, PRECLINICAL EVALUATION OF NOVEL TSPO-PET LIGAND <sup>18</sup>F-VUIIS1008 TO IMAGE GLIOMA

#### **6.1 Abstract**

Positron emission tomography (PET) imaging biomarkers of glioma are limited. Our laboratory has explored translocator protein (TSPO) PET ligands as candidates for molecular imaging of glioma, as TSPO levels correlate with tumor grade in this setting. The purpose of this study was to evaluate a novel, high-affinity TSPO PET ligand (<sup>18</sup>F-VUIIS1008) for quantitative assessment of TSPO expression in glioma. In this study, healthy mice and glioma-bearing rats were imaged with <sup>18</sup>F-VUIIS1008 in a microPET system. Dynamic acquisitions were acquired simultaneously upon tracer injection, with reversibility and specificity evaluated by 'cold' ligand displacement studies or blocking studies. Compartmental modeling of PET data from gliomas imaged with <sup>18</sup>F-VUIIS1008 was performed using metabolite-corrected arterial input functions and PMOD. In mice, <sup>18</sup>F-VUIIS1008 exhibited reversible binding in healthy, TSPO-rich tissues such as myocardium, lung, and renal tissue. In glioma studies, greater tumor-to-background ratio was observed for <sup>18</sup>F-VUIIS1008 compared to a previously evaluated tracer in this setting, <sup>18</sup>F-DPA-714. Tumor accumulation of <sup>18</sup>F-VUIIS1008 could be blocked by pretreatment with 'cold' ligand. Unlike healthy, TSPO-rich tissues, <sup>18</sup>F-VUIIS1008 exhibited indolent release from tumors with

displacement. Compartmental modeling suggested that  $^{18}\text{F}$ -VUIIS1008 binding in tumors, but not healthy brain, was essentially irreversible. These studies illuminate the novel agent,  $^{18}\text{F}$ -VUIIS1008, as a promising TSPO PET ligand with unique properties in cancer cells and may have utility for imaging glioma and potentially other solid tumors.

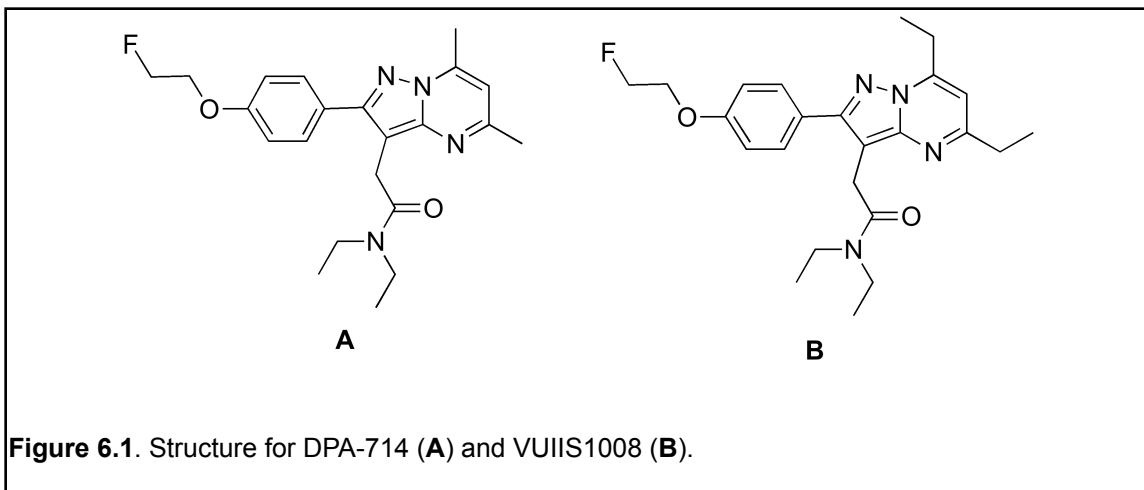
## **6.2 Introduction**

Malignant gliomas are the most common primary brain tumors and represent a particularly lethal form of cancer. They are characterized by invasive growth and recalcitrance to therapy, and thus, patients with malignant gliomas currently have a very poor prognosis. Gliomas are classified according to histological appearance and degree of malignancy according to criteria established by the World Health Organization.<sup>71</sup> Currently, the diagnosis and grading of gliomas are based upon the pathology of biopsy or resected specimens with limitations inherent to sampling heterogeneous tumors. In the absence of repeat biopsies, clinical decisions are routinely guided by imaging.<sup>50</sup> Though routinely employed clinically, CT and MRI and provide little molecular information attributable to the pathology of the disease and poorly discriminate margins, particularly with infiltrative disease. PET imaging has the potential to overcome many of the limitations associated with CT and MRI of brain tumors. However, tracers available for PET imaging of brain tumors are limited. For example,  $^{18}\text{F}$ -FDG PET is used clinically for grading brain tumors, although measures are confounded by high glucose uptake in normal brain that results in

modest to poor tumor-to-background ratios. Thus, there remains a need to develop and validate additional molecular imaging techniques suitable for detection and characterization of gliomas.

Translocator protein (TSPO) is an 18 kDa protein typically localized to the outer mitochondrial membrane that participates in regulation of numerous cellular processes, including cholesterol metabolism, steroid biosynthesis, cellular proliferation, and apoptosis, and is elevated in numerous diseased states. In oncology, TSPO expression is typically linked with disease progression and diminished survival<sup>5, 16, 20, 53, 55</sup> and is a hallmark of aggressive and potentially metastatic tumors.<sup>8, 10, 56</sup> For this reason, our laboratory has explored the use of TSPO imaging ligands within the context of colon cancer,<sup>7</sup> breast cancer,<sup>25</sup> and glioma,<sup>35, 37</sup> as these agents could potentially serve as useful cancer imaging biomarkers.

Recently, we carried out a focused library synthesis and structure activity relationship analysis of novel pyrazolopyrimidines to discover a PET ligand (VUIIS1008) that exhibited a 36-fold enhancement in binding affinity ( $K_i = 0.3$  nM) compared to a previously reported pyrazolopyrimidine, DPA-714<sup>37, 72</sup> (**Figure 6.1**). Radiolabeling this compound with fluorine-18 (<sup>18</sup>F) produced <sup>18</sup>F-VUIIS1008, which exhibited promising characteristics for *in vivo* cancer imaging. The purpose of the present study was to quantitatively evaluate the *in vivo* imaging performance of <sup>18</sup>F-VUIIS1008 in a preclinical model of C6 glioma. In murine biodistribution studies, we found that <sup>18</sup>F-VUIIS1008 accumulated in healthy, TSPO-dense tissues, such as myocardium, lung, and renal tissue, and



was readily displaceable. In C6 gliomas,  $^{18}\text{F}$ -VUIIS1008 uptake was robust, facilitating excellent contrast between tumor and normal brain. While  $^{18}\text{F}$ -VUIIS1008 uptake in the tumors could be effectively blocked by administering nonradioactive ligand prior to the PET agent, displacement studies revealed indolent release kinetics from tumors on the PET imaging timescale. Accumulation of  $^{18}\text{F}$ -VUIIS1008 in tumor and normal brain fit a 2-tissue, 4-rate-constant kinetic model ( $K_1$ ,  $k_2$ ,  $k_3$ ,  $k_4$ ), with tumors exhibiting negligible efflux ( $k_4$ ) values. Overall,  $^{18}\text{F}$ -VUIIS1008 exhibited higher tumor-to-background ratios than a previously evaluated tracer,  $^{18}\text{F}$ -DPA-714, as measured by comparing volumes of distribution ( $V_T$ ) in tumor and normal brain. Overall, these studies illuminate  $^{18}\text{F}$ -VUIIS1008 as a promising PET ligand for evaluating TSPO expression in tumors and potentially other diseases.

## 6.2. Materials and Methods

### Radiosynthesis

<sup>18</sup>F-VUIIS1008 and its tosylate ester precursor were prepared as described.<sup>37, 72</sup> In brief, using a commercial apparatus (TRACERlab FX F-N; GE Healthcare, Little Chalfont, UK), we dried aqueous <sup>18</sup>F-fluoride ion (~3 Ci/111 GBq) by iterative cycles of addition and evaporation of acetonitrile, followed by complexation with K<sup>+</sup>-K<sub>2.2.2</sub>/K<sub>2</sub>CO<sub>3</sub>. The complex was then reacted with 2-(4-(3-(2-(diethylamino)-2-oxoethyl)-5,7-diethylpyrazolo[1,5-a]pyrimidin-2-yl)phenoxy)ethyl 4-methylbenzenesulfonate (4.0 mg) at 99 °C for 20 min in anhydrous dimethyl sulfoxide (0.6 mL). <sup>18</sup>F-VUIIS1008 was purified using reversed-phase high-performance liquid chromatography (C18, Dynamax 250 x 21.4 mm; Varian), eluting at 6.0 mL/min with 10 mM NaH<sub>2</sub>PO<sub>4</sub> buffer (pH 6.7) and ethanol (47.5/52.5, v/v). <sup>18</sup>F-VUIIS1008 was collected directly into 140 mL of water (deionized), passed through a C-18 Sep-Pak (Waters, Milford, MA, USA) followed by sequential elution with 200 proof ethanol (1.0 mL) and saline (9.0 mL) into a sterile vial. Typical specific activities were 4203 Ci/mmol (156 TBq/mmol) or greater. The radiotracer preparation was visually inspected for clarity, absence of color, and particulates.

## **Animals**

All studies involving animals were conducted in compliance with federal and institutional guidelines. Healthy BL 6 mice were used for biodistribution studies. For glioma studies, two weeks prior to imaging, healthy male Wistar rats were stereotactically inculcated in the right hemisphere with  $1.0 \times 10^5$  C6 glioma cells (American Type Tissue Collection, Manassas, VA, USA). Prior to imaging, rats were affixed with venous and arterial catheters.



## **MRI**

MRI was used to localize tumors and for registration with PET. Rats were secured prone in a radiofrequency coil (38-mm inner diameter) and placed in a 4.7-T horizontal bore imaging system (Varian Inc., Palo Alto, CA, USA). A constant body temperature of 37 °C was maintained using heated airflow. An initial multislice gradient-echo imaging sequence (repetition time, 150 ms; echo time, 3.5 ms; matrix, 128 x 128; field of view, 40 x 40 mm<sup>2</sup>; slice thickness, 2 mm) was used to acquire 7 slices in each imaging plane (axial, coronal, sagittal) for proper positioning of subsequent scans. A multislice T<sub>2</sub>-weighted fast spin-echo scan with 8 echoes and 8.0-ms echo spacing (effective echo time, 32 ms) was then collected with a repetition time of 2,000 ms; field of view of 32 x 32 mm<sup>2</sup>; matrix of 128 × 128; 16 acquisitions; and 8 coronal slices of 2-mm thickness.

## **PET/CT**

PET/CT was performed within 24 hours of MRI in rats with confirmed tumors. Tumor-bearing rats were administered <sup>18</sup>F-VUIIS1008 *via* jugular catheter while in a microPET Focus 220 scanner (Siemens, Knoxville, TN, USA). Data were collected in list-mode format for 60 or 90 minutes, followed by a CT scan (microCAT II; Siemens) for attenuation correction. The dynamic PET acquisition was divided into twelve 10-second frames for the first two minutes, three 60-second frames for the following three minutes, and seventeen 300-second frames for the duration of the scan. The raw data within each frame were then binned into three-dimensional sinograms, with a span of three and ring

difference of 47. The sonograms were reconstructed into tomographic images (128 x 128 x 95) with voxel sizes of 0.095 x 0.095 x 0.08 cm<sup>3</sup>, after scatter and attenuation corrections were applied, using a two-dimensional ordered-subsets expectation-maximization algorithm with 16 subsets and four iterations. Attenuation correction was accomplished by generating an attenuation map from the CT images. The CT image was first coregistered with the small animal PET image, segmented, and then projected into sonogram space with a span of 47 and ring difference of 23. Time-activity curves were generated by manually drawing 3-dimensional volumes of interest over tumor and contralateral brain using ASIPro (Siemens).

#### ***In vivo* uptake and displacement of <sup>18</sup>F-VUIIS1008 in healthy mice**

*In vivo* uptake and displacement of <sup>18</sup>F-VUIIS1008 was performed in healthy BL 6 mice. Mice were administered 250 µCi (9.25 MBq) of <sup>18</sup>F-VUIIS1008 upon initiation of a dynamic PET acquisition. Thirty minutes post-tracer infusion, <sup>19</sup>F-VUIIS1008 (20 mg/kg) was administered intravenously. Regions of interest (ROIs) corresponding to heart, lung, kidney, and liver were manually drawn using ASIPro (Siemens).

#### ***In vivo* uptake, blocking, and displacement of <sup>18</sup>F-VUIIS1008 in C6 glioma-bearing rats**

*In vivo* uptake, blocking, and displacement studies were carried out in glioma-bearing rats (n=3) on sequential days. For blocking studies, excess <sup>19</sup>F-

VUIIS1008 (20 mg/kg) was injected five minutes prior to  $^{18}\text{F}$ -VUIIS1008 administration, followed by a 60-min dynamic PET scan. For displacement studies, excess  $^{19}\text{F}$ -VUIIS1008 (20 mg/kg) was injected 30 minutes after  $^{18}\text{F}$ -VUIIS1008 administration during a 60-min dynamic PET scan. ROIs were selected for tumor and brain using ASIPro (Siemens).

### **HPLC Radiometabolite Analysis**

Low concentration of radiometabolite and the parent compound in the plasma confers the limitation for the AIF correction with radio-HPLC methods.<sup>35, 37, 72</sup> This can be solved by using the more sensitive radiometabolite analysis with radio-TLC. In this analysis, arterial blood (200  $\mu\text{L}$ ) was collected at 2, 12, 30, 60, and 90 minutes following injection of 1.5 mCi (55.5 MBq) of  $^{18}\text{F}$ -VUIIS1008. After centrifugation, the plasma was extracted with acetonitrile/water (340  $\mu\text{L}$ , 7/1, v/v). The mixture was then centrifuged and the supernatant used for the TLC ( $\text{CH}_2\text{Cl}_2/\text{MeOH} = 9 : 1$  (V/V)) radiometabolite analysis with AR-2000 radio-TLC imaging scanner (Bioscan, France).

### **Image Analysis and Modeling**

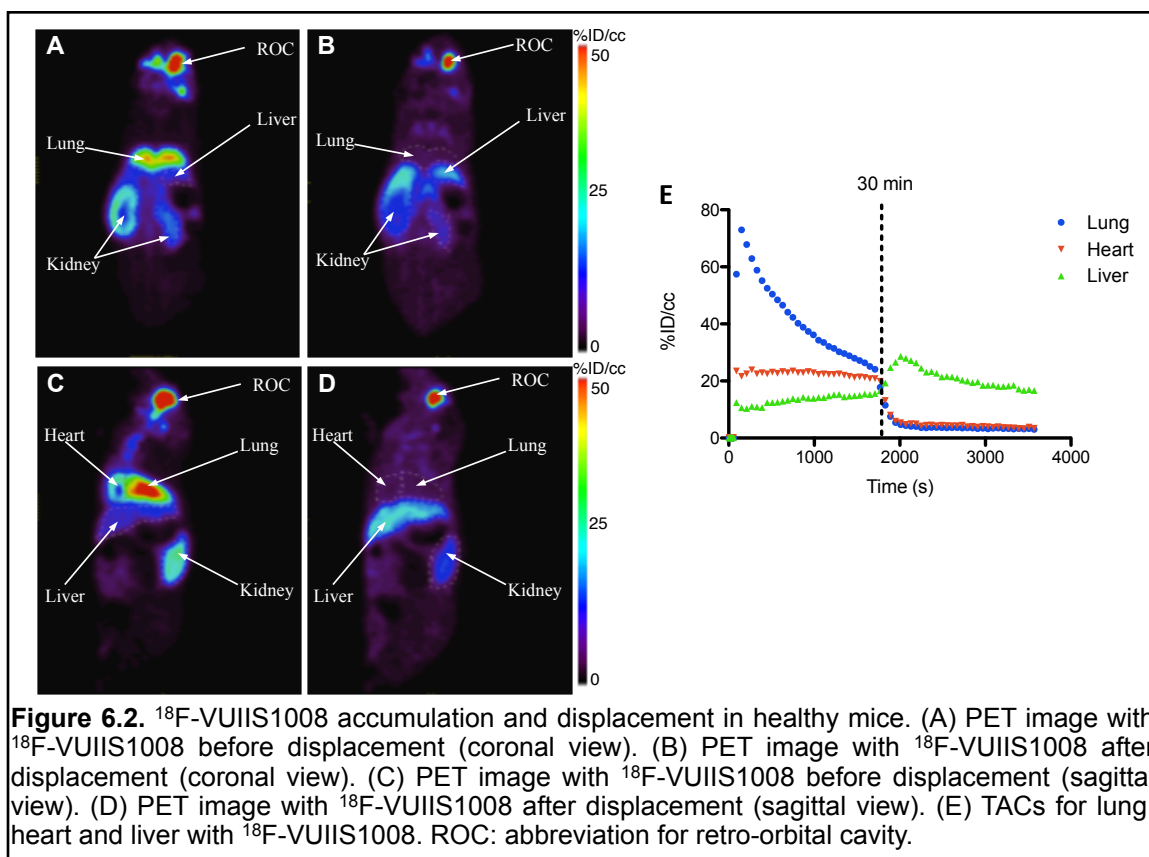
Time-activity curves (TACs) were generated by manually drawing three-dimensional volumes of interest over tumor and contralateral brain using ASIPro. The arterial input function (AIF) was computed from plasma sampling during imaging and corrected for metabolism of the parent ligand. In this study, a 1-tissue, 2-rate-constant kinetic model, and a 2-tissue, 4-rate-constant kinetic

model were used to characterize  $^{18}\text{F}$ -VUIIS1008 pharmacokinetics with the PMOD software package. Model fit was evaluated by ChiSquare ( $\chi^2$ ) value and visual inspection.

### 6.3. Results

#### $^{18}\text{F}$ -VUIIS1008 accumulation and displacement in healthy mice

We evaluated organ accumulation and reversibility of  $^{18}\text{F}$ -VUIIS1008 in normal tissues using healthy mice and 60-minute dynamic PET scanning. Thirty minutes after intravenous administration, the greatest accumulation of  $^{18}\text{F}$ -

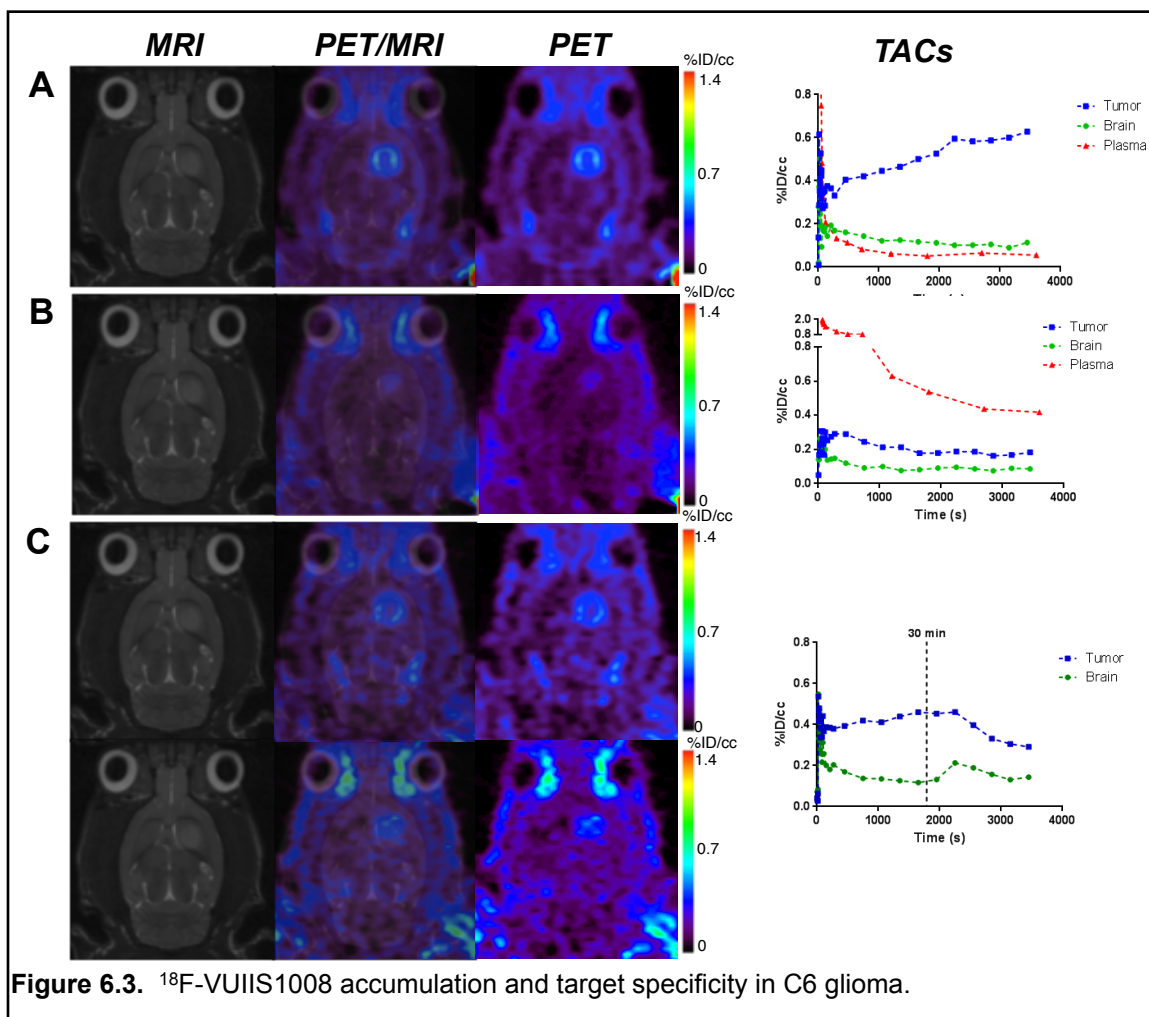


VUIIS1008 was observed in myocardium, lung, and renal tissue, with lesser

accumulation observed in the liver (**Figure 6.2**). Thirty minutes after tracer administration, intravenous administration of VUIIS1008 (20 mg/kg) resulted in rapid and complete displacement of  $^{18}\text{F}$ -VUIIS1008 from myocardium and lung tissue and approximately 50% displacement from renal tissue. Following displacement, slightly increased activity was observed in the liver. Overall, the biodistribution of  $^{18}\text{F}$ -VUIIS1008 appeared to be consistent with TSPO densities typically observed in healthy tissues and organs of excretion.

### **$^{18}\text{F}$ -VUIIS1008 accumulation and target specificity in C6 glioma**

Subsequently, accumulation of  $^{18}\text{F}$ -VUIIS1008 and its specificity was evaluated in C6 glioma-bearing rats. Tracer uptake, blocking, and displacement were evaluated in serial, 60-minute dynamic PET studies on an intra-subject basis over 48 hours (**Figure 6.3**, data from a single rat shown). Guided by T<sub>2</sub>-weighted MRI,  $^{18}\text{F}$ -VUIIS1008 exhibited robust accumulation in C6 gliomas with negligible accumulation observed in normal brain (**Figure 6.3A**). Overall, the TACs illustrated rapid tracer delivery to tumor and normal brain, as well as an expected radioactivity spike in plasma consistent with intravenous administration.  $^{18}\text{F}$ -VUIIS1008 did not accumulate in normal brain appreciably and cleared rapidly from this tissue and plasma. Conversely,  $^{18}\text{F}$ -VUIIS1008 accumulated in tumor tissue and activity increased modestly over time. Ultimately, a signal-to-noise reached of 6:1 comparing tumor to normal brain was achieved by the end of the 60-minute PET scan. To evaluate specificity, a blocking study was conducted where VUIIS1008 was administered five minutes prior to  $^{18}\text{F}$ -



VUIIS1008 administration with initiation of dynamic PET study (**Figure 6.3B**). A blocking dosage of 20 mg/kg of VUIIS1008 led to significantly elevated plasma radioactivity compared with the unblocked scenario and  $^{18}\text{F}$ -VUIIS1008 uptake in tumor tissue that mirrored levels similar to those observed previously in normal brain.  $^{18}\text{F}$ -VUIIS1008 uptake in tumor tissue was blocked by greater than 70% when comparing unblocked and blocked imaging studies. The blocking dose had an insignificant effect on  $^{18}\text{F}$ -VUIIS1008 accumulation in normal brain. To evaluate the reversibility of  $^{18}\text{F}$ -VUIIS1008 in tumor and normal brain, we conducted a displacement study, where VUIIS1008 was administered thirty

minutes following  $^{18}\text{F}$ -VUIIS1008 administration during a typical dynamic PET study (**Figure 6.3C**). Over the first thirty minutes, similar  $^{18}\text{F}$ -VUIIS1008 uptake characteristics were observed in tumor and healthy brain compared with the control study conducted 48 hours prior (see **Figure 6.3A**). Unlike displacement in healthy, TSPO-rich tissues (**Figure 6.2**), intravenous administration of VUIIS1008 (20 mg/kg) resulted in an indolent washout of  $^{18}\text{F}$ -VUIIS1008 from tumor tissue that was reduced approximately 50% by the conclusion of the PET study. Concurrently, minor tracer reperfusion and subsequent washout was observed in healthy brain following displacement.

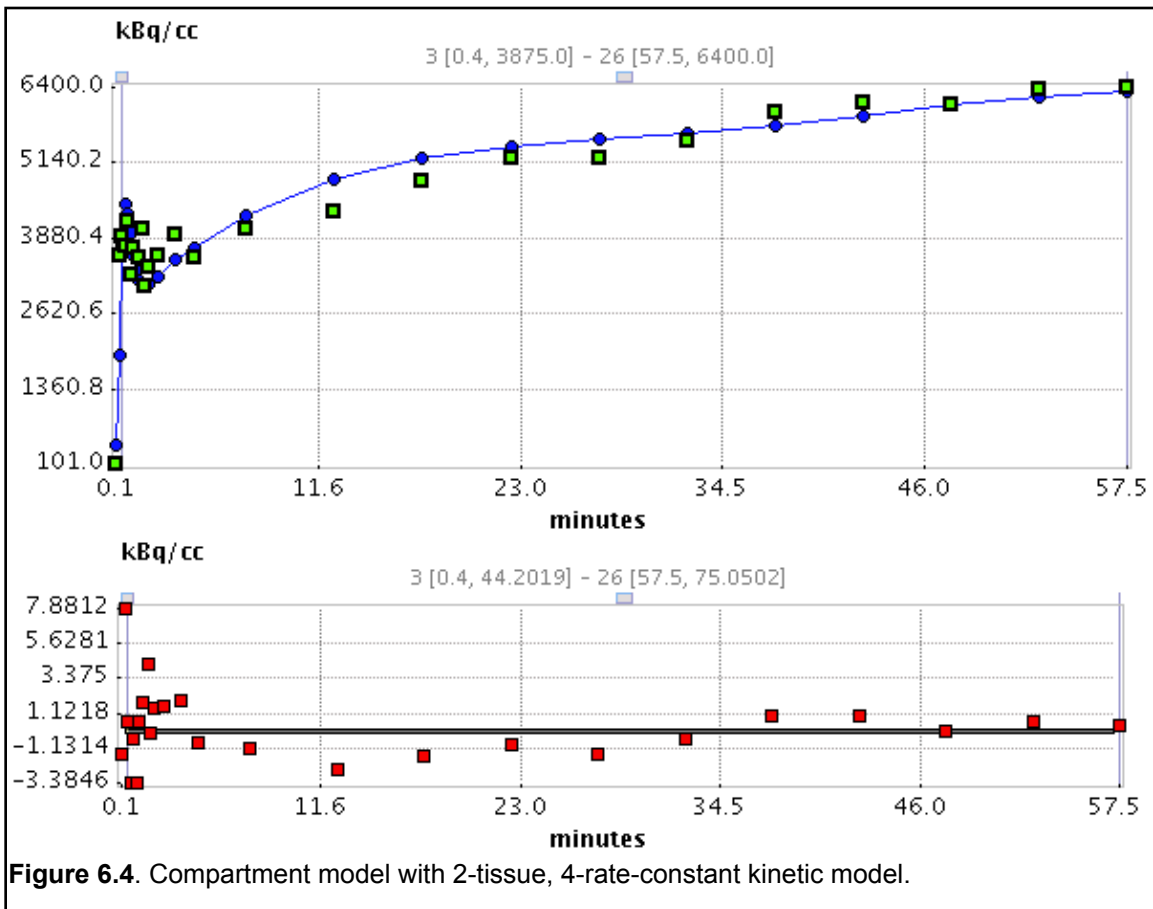


**Figure 6.4.** Compartment model with 2-tissue, 4-rate-constant kinetic model.

## Compartmental modeling

Pharmacokinetic modeling was used to quantitatively examine the uptake and clearance characteristics of  $^{18}\text{F}$ -VUIIS1008 in tumor tissue and normal brain. As with other TSPO PET ligands we have evaluated in this setting,<sup>35, 37</sup>  $^{18}\text{F}$ -VUIIS1008 pharmacokinetics in tumor and normal brain were best described by a 2-tissue, 4-rate-constant kinetic model, as opposed to a 1-tissue, 2-rate-constant kinetic model, on the basis of inspection (**Figure 6.4 and Figure 6.5**) and goodness of fit ( $\chi^2$ ) (**Table 6.1**). Terms that reflect delivery and efflux from a non-

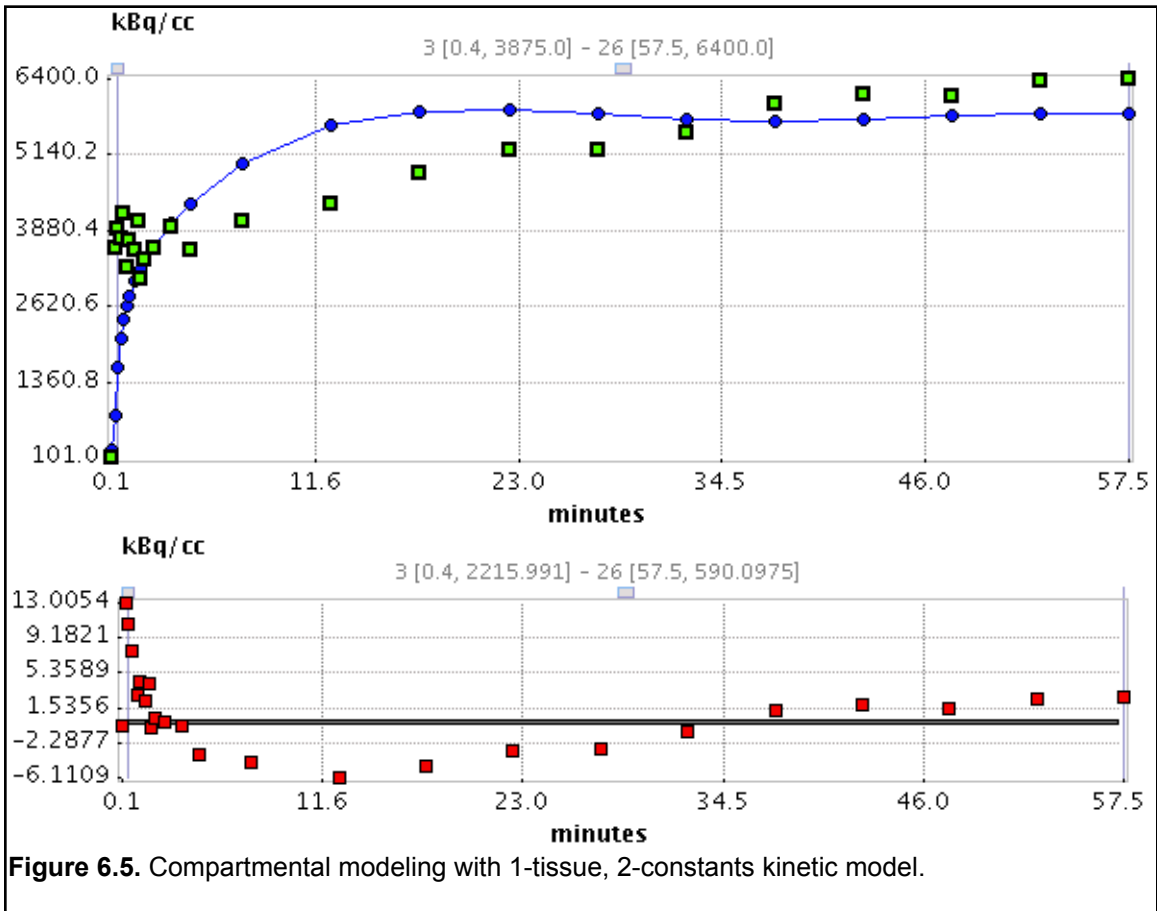


**Figure 6.5.** Compartmental modeling with 1-tissue, 2-constants kinetic model.

binding compartment ( $K_1$ ,  $k_2$ ) were similar for  $^{18}\text{F}$ -VUIIS1008 in normal brain and tumor tissue. Values for delivery to a specific binding compartment ( $k_3$ ),



**Table 6.1.** Modeling fit of  $^{18}\text{F}$ -VUIIS1008 with 1-tissue, 2-constant kinetic model and 2-tissue, 4-constant kinetic model.

Region	Model	$K_1$	$k_2$	$k_3$	$k_4$	$\chi^2$
Brain (n = 5)	1-Tissue, 2-constants	$0.322 \pm 0.15$	$0.101 \pm 0.017$			$55.165 \pm 12.385$
Brain (n = 5)	2-Tissue, 4-constants	$0.881 \pm 0.392$	$2.078 \pm 1.666$	$0.172 \pm 0.070$	$0.037 \pm 0.004$	$26.311 \pm 5.210$
Tumor (n = 5)	1-Tissue, 2-constants	$0.330 \pm 0.147$	$0.023 \pm 0.005$			$38.579 \pm 5.809$
Tumor (n = 5)	2-Tissue, 4-constants	$0.709 \pm 0.306$	$0.442 \pm 0.101$	$0.113 \pm 0.013$	$0.009 \pm 0.002$	$9.458 \pm 2.623$

Value = Mean  $\pm$  SE.

comparing tumor and normal brain, were also similar. Though the values for the parameter describing efflux ( $k_4$ ) from the specific binding compartment were small for both tissues, a detectable  $k_4$  was consistently observed in normal brain but was almost zero in tumor tissue suggesting binding in this compartment was essentially irreversible.

#### Comparison of pharmacokinetics of $^{18}\text{F}$ -VUIIS1008 and $^{18}\text{F}$ -DPA-714.

The *in vivo* performance of  $^{18}\text{F}$ -VUIIS1008 compared favorably to another TSPO PET agent we previously evaluated in this setting,  $^{18}\text{F}$ -DPA-714 (**Table 6.2**). In healthy brain and tumor tissue,  $^{18}\text{F}$ -VUIIS1008 exhibited lower ratios of delivery to efflux parameters ( $K_1/k_2$ ) in the non-binding compartment compared to  $^{18}\text{F}$ -DPA-714. For tumors, the opposite was observed for the specific binding compartment, where delivery to efflux parameter ( $k_3/k_4$ ) ratios were higher for  $^{18}\text{F}$ -VUIIS1008 compared to  $^{18}\text{F}$ -DPA-714. In normal brain, ( $k_3/k_4$ ) ratios were

similar for both tracers. Taken together, these results appear to be congruent with the relative affinities of these probes<sup>72</sup> and suggest that <sup>18</sup>F-VUIIS1008 may possess somewhat greater specificity than <sup>18</sup>F-DPA-714. Overall, calculated  $V_T$  levels for tumor and normal brain were higher for <sup>18</sup>F-DPA-714, yet  $V_T$  ratios for tumor and normal brain were higher for <sup>18</sup>F-VUIIS1008 in these studies (6.0 *versus* 4.4), which led to improved signal-to-noise ratio.

**Table 6.2.** Comparison between <sup>18</sup>F-VUIIS1008 and <sup>18</sup>F-DPA-714.

Probe	Region	$K_1/k_2$	$k_3/k_4$	$V_T=(K_1/k_2)(1+k_3/k_4)$
<sup>18</sup> F-VUIIS1008 <sup>a</sup>	Brain	0.855 ± 0.325	4.435 ± 1.387	4.210 ± 1.612
	Tumor	1.902 ± 0.816	12.634 ± 1.406	25.224 ± 10.035
<sup>18</sup> F-DPA-714 <sup>b</sup>	Brain	3.619 ± 0.551	4.024 ± 0.842	15.963 ± 3.566
	Tumor	6.867 ± 1.226	8.913 ± 1.155	70.033 ± 14.729

*a. Modeling with C6-glioma bearing rats (n = 5).*  
*b. See reference<sup>37</sup>*  
*Results = Mean ± SE.*

## 6.4 Discussion

Our laboratory has explored translocator protein (TSPO) expression as a target for molecular imaging of cancer.<sup>1-5</sup> Formerly referred to as peripheral benzodiazepine receptor (PBR), TSPO is an 18-kDa protein typically localized to the outer mitochondria membrane. TSPO participates in the regulation of numerous cellular processes, including cholesterol metabolism, steroid biosynthesis, cellular proliferation, and apoptosis.<sup>6</sup> In normal tissues, TSPO tends to be expressed in those that produce steroids and those that are mitochondria-enriched, such as skeletal muscle, renal tissue, and myocardium. Tissues such

as liver and brain exhibit comparatively modest expression.<sup>6</sup> While historically exploited as a target in neuroscience, elevated TSPO expression is also observed in cancers of the breast,<sup>10, 11</sup> prostate,<sup>8, 9</sup> oral cavity,<sup>16</sup> colon,<sup>6, 7, 20</sup> liver,<sup>15, 65</sup> and brain.<sup>14, 54</sup> In oncology, TSPO expression is typically linked with disease progression and diminished survival<sup>5, 16, 20, 53, 55</sup> and is a hallmark of aggressive and potentially metastatic tumors.<sup>8, 10, 56</sup> We recently reported the first utilizations of the PET agents *N*-[<sup>18</sup>F]fluoroacetyl-*N*-(2,5-dimethoxybenzyl)-2-phenoxyaniline (<sup>18</sup>F-PBR06)<sup>35</sup> and *N,N*-diethyl-2-(2-(4-(2-[<sup>18</sup>F]fluoroethoxy)phenyl)-5,7-dimethylpyrazolo[1,5-*a*]pyrimidin-3-yl)acetamide (<sup>18</sup>F-DPA-714)<sup>37</sup> for quantitative assessment of TSPO expression in preclinical glioma. In these proof-of-principle PET imaging studies, tumors proved detectable among surrounding normal brain and, importantly, TSPO levels could be quantitatively assayed in tumors using compartmental analysis of the PET data.<sup>35, 37</sup> However, potential drawbacks were observed with both agents in this context, including tracer accumulation in normal brain that reached levels potentially sufficient to prevent detection of gliomas with modest TSPO expression, such as lower grade disease. Both tracers also exhibited significant metabolism *in vivo*, which required correction of plasma input functions for quantitative analysis. While illustrating the potential of TSPO PET to detect tumors in brain, these studies prompted our desire to develop novel TSPO PET ligands with improved properties for cancer imaging.

In this study, we quantitatively evaluated the *in vivo* performance of a novel TSPO PET ligand, <sup>18</sup>F-VUIIS1008. A seemingly minor structural alteration, substitution of the 5,7-methyl groups on the pyrazolopyrimidine ring of <sup>18</sup>F-

DPA-714 with ethyl groups, results in  $^{18}\text{F}$ -VUIIS1008 (**Figure 6.1**). However, this structural modification returned a 36-fold enhancement in binding affinity for TSPO,<sup>72</sup> and as shown here, a number of intriguing and potentially improved properties for cancer imaging. For example,  $^{18}\text{F}$ -VUIIS1008 exhibits an interesting tumor-discriminating quality in that ligand binding is highly reversible in normal tissue, but was practically irreversible in tumor tissues evaluated in this study. The precise mechanism of this behavior has yet to be elucidated, but it was not obvious that the phenomenon was simply related to the density of TSPO in tumor tissue, as other TSPO-rich normal tissues such as myocardium, exhibited binding that was freely reversible. More practically,  $^{18}\text{F}$ -VUIIS1008 exhibited improved tumor-to-background ratio in these studies compared  $^{18}\text{F}$ -DPA-714 and, accordingly, might represent an improved probe for detecting tumors with modest TSPO expression profiles.

## **6.5. Conclusion**

These studies illuminate  $^{18}\text{F}$ -VUIIS1008 as a promising a PET ligand for evaluating TSPO expression in glioma. Further studies should evaluate this agent in other settings, which may include colorectal or breast cancer.

## CHAPTER 7

### CONCLUSION

The overall goal of this project was to explore the development and utilization of TSPO PET ligands as potential biomarkers of cancer. We first optimized the total synthesis of a high-affinity TSPO ligand, DPA-714, which gave us access to this known ligand. Our new protocol significantly reduced overall reaction times while maintaining or even improving synthetic yields. Going further, we synthesized and evaluated the pyrazolopyrimidine  $^{18}\text{F}$ -DPA-714 in preclinical studies that illustrated the feasibility of using this agent for cancer imaging and validated our overall approach to use TSPO PET ligands to visualize brain tumors. Though  $^{18}\text{F}$ -DPA-714 appeared suitable for quantitative assay of TSPO levels in tumors, we observed some drawbacks associated with  $^{18}\text{F}$ -DPA-714 which included metabolism and moderate uptake in normal brain. These observations led us to hypothesize that improved ligands based upon this scaffold could be developed.

Our next approach was to develop a synthetic strategy to enable the rapid expansion of libraries of diverse pyrazolopyrimidines. This methodology leveraged use of 3-(4-(2-fluoroethoxy)phenyl)-3-oxopropanenitrile in the synthetic sequence, as well as the advantages inherent to MAOS to reduce labor, time, and resources required for library syntheses. Applying this approach, we synthesized a diverse and demonstrative library of pyrazolopyrimidines by

introducing various diones at the final, divergent step of the synthesis. In the case of TSPO ligand design, we found this methodology enabled rapid exploration of structure-activity relationships. For example, a focused library of pyrazolopyrimidines led to the discovery that the 5,6,7-substitution pattern is a critical determinant of TSPO affinity. These SAR studies led to the discovery of VUIIS1008, a TSPO ligand exhibiting significantly increased affinity compared to DPA-714<sup>37</sup> and TSPO ligands derived from other chemical entities.<sup>35</sup> In addition to improved TSPO affinity, VUIIS1008 proved TSPO-selective, exhibiting negligible binding affinity to CBR. We developed radiochemistry methods to radiolabel VUIIS1008 with fluorine-18 to yield <sup>18</sup>F-VUIIS1008. *In vivo* PET imaging studies with <sup>18</sup>F-VUIIS1008 demonstrated the ability of this probe to detect C6 tumors. Blocking and displacement studies indicated the specific binding and partial irreversibility of <sup>18</sup>F-VUIIS1008 in tumors. Pharmacokinetic modeling studies illustrated potentially greater specificity for <sup>18</sup>F-VUIIS1008 compared with <sup>18</sup>F-DPA-714. Overall, these studies, which culminated in the discovery of <sup>18</sup>F-VUIIS1008, suggest the fruitfulness of developing novel TSPO ligands for cancer imaging. Ongoing studies with <sup>18</sup>F-VUIIS1008 and other novel pyrazolopyrimidines developed in this project focus on prioritization of a novel ligand for clinical translation.

## BIBLIOGRAPHY

1. Papadopoulos V, Baraldi M, Guilarte TR, et al. Translocator protein (18kDa): new nomenclature for the peripheral-type benzodiazepine receptor based on its structure and molecular function. *Trends Pharmacol Sci.* Aug 2006;27(8):402-409.
2. Papadopoulos V, Lecanu L. Translocator protein (18 kDa) TSPO: an emerging therapeutic target in neurotrauma. *Exp Neurol.* Sep 2009;219(1):53-57.
3. Anholt RR, De Souza EB, Oster-Granite ML, Snyder SH. Peripheral-type benzodiazepine receptors: autoradiographic localization in whole-body sections of neonatal rats. *J Pharmacol Exp Ther.* May 1985;233(2):517-526.
4. Gavish M, Bachman I, Shoukrun R, et al. Enigma of the peripheral benzodiazepine receptor. *Pharmacol Rev.* Dec 1999;51(4):629-650.
5. Galiegue S, Casellas P, Kramar A, Tinel N, Simony-Lafontaine J. Immunohistochemical assessment of the peripheral benzodiazepine receptor in breast cancer and its relationship with survival. *Clin Cancer Res.* Mar 15 2004;10(6):2058-2064.
6. Maaser K, Hopfner M, Jansen A, et al. Specific ligands of the peripheral benzodiazepine receptor induce apoptosis and cell cycle arrest in human colorectal cancer cells. *Br J Cancer.* Nov 30 2001;85(11):1771-1780.
7. Deane NG, Manning HC, Foutch AC, et al. Targeted imaging of colonic tumors in smad3<sup>-/-</sup> mice discriminates cancer and inflammation. *Mol Cancer Res.* Apr 2007;5(4):341-349.
8. Han Z, Slack RS, Li W, Papadopoulos V. Expression of peripheral benzodiazepine receptor (PBR) in human tumors: relationship to breast, colorectal, and prostate tumor progression. *J Recept Signal Transduct Res.* 2003;23(2-3):225-238.
9. Fafalios A, Akhavan A, Parwani AV, Bies RR, McHugh KJ, Pflug BR. Translocator protein blockade reduces prostate tumor growth. *Clin Cancer Res.* Oct 1 2009;15(19):6177-6184.
10. Hardwick M, Fertikh D, Culty M, Li H, Vidic B, Papadopoulos V. Peripheral-type benzodiazepine receptor (PBR) in human breast cancer: correlation of breast cancer cell aggressive phenotype with PBR expression, nuclear localization, and PBR-mediated cell proliferation and nuclear transport of cholesterol. *Cancer Res.* Feb 15 1999;59(4):831-842.
11. Carmel I, Fares FA, Leschiner S, Scherubl H, Weisinger G, Gavish M. Peripheral-type benzodiazepine receptors in the regulation of proliferation of MCF-7 human breast carcinoma cell line. *Biochem Pharmacol.* Jul 15 1999;58(2):273-278.
12. Black KL, Mazziotta JC, Becker DP. Brain tumors. *West J Med.* Feb 1991;154(2):186-197.

13. Decaudin D, Castedo M, Nemati F, et al. Peripheral benzodiazepine receptor ligands reverse apoptosis resistance of cancer cells in vitro and in vivo. *Cancer Res.* Mar 1 2002;62(5):1388-1393.
14. Starosta-Rubinstein S, Ciliax BJ, Penney JB, McKeever P, Young AB. Imaging of a glioma using peripheral benzodiazepine receptor ligands. *Proc Natl Acad Sci U S A.* Feb 1987;84(3):891-895.
15. Venturini I, Zeneroli ML, Corsi L, et al. Up-regulation of peripheral benzodiazepine receptor system in hepatocellular carcinoma. *Life Sci.* 1998;63(14):1269-1280.
16. Nagler R, Ben-Izhak O, Savulescu D, et al. Oral cancer, cigarette smoke and mitochondrial 18kDa translocator protein (TSPO) - In vitro, in vivo, salivary analysis. *Biochim Biophys Acta.* May 2010;1802(5):454-461.
17. Li W, Hardwick MJ, Rosenthal D, Culty M, Papadopoulos V. Peripheral-type benzodiazepine receptor overexpression and knockdown in human breast cancer cells indicate its prominent role in tumor cell proliferation. *Biochem Pharmacol.* Feb 15 2007;73(4):491-503.
18. Dolle F, Luus C, Reynolds A, Kassiou M. Radiolabelled molecules for imaging the translocator protein (18 kDa) using positron emission tomography. *Curr Med Chem.* 2009;16(22):2899-2923.
19. Nagler R, Savulescu D, Krayzler E, Leschiner S, Veenman L, Gavish M. Cigarette Smoke Decreases Salivary 18 kDa Translocator Protein Binding Affinity - in Association with Oxidative Stress. *Curr Med Chem.* May 24 2010.
20. Maaser K, Grabowski P, Sutter AP, et al. Overexpression of the peripheral benzodiazepine receptor is a relevant prognostic factor in stage III colorectal cancer. *Clin Cancer Res.* Oct 2002;8(10):3205-3209.
21. Miettinen H, Kononen J, Haapasalo H, et al. Expression of Peripheral-Type Benzodiazepine Receptor and Diazepam-Binding Inhibitor in Human Astrocytomas - Relationship to Cell-Proliferation. *Cancer Research.* Jun 15 1995;55(12):2691-2695.
22. Batarseh A, Papadopoulos V. Regulation of translocator protein 18 kDa (TSPO) expression in health and disease states. *Mol Cell Endocrinol.* Oct 7 2010;327(1-2):1-12.
23. Delavoie F, Li H, Hardwick M, et al. In vivo and in vitro peripheral-type benzodiazepine receptor polymerization: functional significance in drug ligand and cholesterol binding. *Biochemistry.* Apr 22 2003;42(15):4506-4519.
24. Mukherjee S, Das SK. Translocator protein (TSPO) in breast cancer. *Curr Mol Med.* May 2012;12(4):443-457.
25. Wyatt SK, Manning HC, Bai M, et al. Molecular imaging of the translocator protein (TSPO) in a pre-clinical model of breast cancer. *Mol Imaging Biol.* Jun 2010;12(3):349-358.
26. Manning HC, Goebel T, Thompson RC, Price RR, Lee H, Bornhop DJ. Targeted molecular imaging agents for cellular-scale bimodal imaging. *Bioconjug Chem.* Nov-Dec 2004;15(6):1488-1495.



27. Tang D, Buck JR, Hight MR, Manning HC. Microwave-assisted Organic Synthesis of a High-affinity Pyrazolo-pyrimidinyl TSPO Ligand. *Tetrahedron Lett.* Sep 1 2010;51(35):4595-4598.
28. Cornu P, Benavides J, Scatton B, Hauw JJ, Philippon J. Increase in omega 3 (peripheral-type benzodiazepine) binding site densities in different types of human brain tumours. A quantitative autoradiography study. *Acta Neurochir (Wien).* 1992;119(1-4):146-152.
29. Olson JM, Junck L, Young AB, Penney JB, Mancini WR. Isoquinoline and peripheral-type benzodiazepine binding in gliomas: implications for diagnostic imaging. *Cancer Res.* Oct 15 1988;48(20):5837-5841.
30. Papadopoulos V, Baraldi M, Guilarte TR, et al. Translocator protein (18 kDa): new nomenclature for the peripheral-type benzodiazepine receptor based on its structure and molecular function. *Trends Pharmacol Sci.* Aug 2006;27(8):402-409.
31. Hardwick M, Cavalli LR, Barlow KD, Haddad BR, Papadopoulos V. Peripheral-type benzodiazepine receptor (PBR) gene amplification in MDA-MB-231 aggressive breast cancer cells. *Cancer Genet Cytogenet.* Nov 2002;139(1):48-51.
32. Black KL, Ikezaki K, Toga AW. Imaging of Brain-Tumors Using Peripheral Benzodiazepine Receptor Ligands. *Journal of Neurosurgery.* Jul 1989;71(1):113-118.
33. Pappata S, Cornu P, Samson Y, et al. PET study of carbon-11-PK 11195 binding to peripheral type benzodiazepine sites in glioblastoma: a case report. *J Nucl Med.* Aug 1991;32(8):1608-1610.
34. Junck L, Olson JM, Ciliax BJ, et al. PET imaging of human gliomas with ligands for the peripheral benzodiazepine binding site. *Ann Neurol.* Dec 1989;26(6):752-758.
35. Buck JR, McKinley ET, Hight MR, et al. Quantitative, preclinical PET of translocator protein expression in glioma using 18F-N-fluoroacetyl-N-(2,5-dimethoxybenzyl)-2-phenoxyaniline. *J Nucl Med.* Jan 2011;52(1):107-114.
36. James ML, Fulton RR, Vercoullie J, et al. DPA-714, a new translocator protein-specific ligand: synthesis, radiofluorination, and pharmacologic characterization. *J Nucl Med.* May 2008;49(5):814-822.
37. Tang D, Hight MR, McKinley ET, et al. Quantitative preclinical imaging of TSPO expression in glioma using N,N-diethyl-2-(2-(4-(2-18F-fluoroethoxy)phenyl)-5,7-dimethylpyrazolo[1,5-a]pyrimidin-3-yl)acetamide. *J Nucl Med.* Feb 2012;53(2):287-294.
38. Selleri S, Bruni F, Costagli C, et al. 2-Arylpyrazolo[1,5-a]pyrimidin-3-yl acetamides. New potent and selective peripheral benzodiazepine receptor ligands. *Bioorg Med Chem.* Oct 2001;9(10):2661-2671.
39. Kozikowski AP, Kotoula M, Ma D, Boujrad N, Tuckmantel W, Papadopoulos V. Synthesis and biology of a 7-nitro-2,1,3-benzoxadiazol-4-yl derivative of 2-phenylindole-3-acetamide: a fluorescent probe for the peripheral-type benzodiazepine receptor. *J Med Chem.* Aug 1 1997;40(16):2435-2439.

40. Veenman L, Shandalov Y, Gavish M. VDAC activation by the 18 kDa translocator protein (TSPO), implications for apoptosis. *J Bioenerg Biomembr.* Jun 2008;40(3):199-205.
41. Galiegue S, Tinel N, Casellas P. The peripheral benzodiazepine receptor: a promising therapeutic drug target. *Curr Med Chem.* Aug 2003;10(16):1563-1572.
42. Chen MK, Guilarte TR. Translocator protein 18 kDa (TSPO): molecular sensor of brain injury and repair. *Pharmacol Ther.* Apr 2008;118(1):1-17.
43. Maaser K, Grabowski P, Oezdem Y, et al. Up-regulation of the peripheral benzodiazepine receptor during human colorectal carcinogenesis and tumor spread. *Clin Cancer Res.* Mar 1 2005;11(5):1751-1756.
44. Manning HC, Goebel T, Marx JN, Bornhop DJ. Facile, efficient conjugation of a trifunctional lanthanide chelate to a peripheral benzodiazepine receptor ligand. *Org Lett.* Apr 4 2002;4(7):1075-1078.
45. Manning HC, Smith SM, Sexton M, et al. A peripheral benzodiazepine receptor targeted agent for in vitro imaging and screening. *Bioconjug Chem.* May-Jun 2006;17(3):735-740.
46. Martin A, Boisgard R, Theze B, et al. Evaluation of the PBR/TSPO radioligand [(18F)DPA-714 in a rat model of focal cerebral ischemia. *J Cereb Blood Flow Metab.* Jan 2010;30(1):230-241.
47. James ML, Fulton RR, Henderson DJ, et al. Synthesis and in vivo evaluation of a novel peripheral benzodiazepine receptor PET radioligand. *Bioorg Med Chem.* Nov 15 2005;13(22):6188-6194.
48. Doorduyn J, Klein HC, Dierckx RA, James M, Kassiou M, de Vries EF. [11C]-DPA-713 and [18F]-DPA-714 as new PET tracers for TSPO: a comparison with [11C]-(R)-PK11195 in a rat model of herpes encephalitis. *Mol Imaging Biol.* Nov-Dec 2009;11(6):386-398.
49. Damont A, Hinnen F, Kuhnast B, et al. Radiosynthesis of [18F]DPA-714, a selective radioligand for imaging the translocator protein (18 kDa) with PET. *Labelled Compounds and Radiopharmaceuticals.* 2008;51:296-292.
50. Dhermain FG, Hau P, Lanfermann H, Jacobs AH, van den Bent MJ. Advanced MRI and PET imaging for assessment of treatment response in patients with gliomas. *Lancet Neurol.* Sep 2010;9(9):906-920.
51. van den Bent MJ, Vogelbaum MA, Wen PY, Macdonald DR, Chang SM. End point assessment in gliomas: novel treatments limit usefulness of classical Macdonald's Criteria. *J Clin Oncol.* Jun 20 2009;27(18):2905-2908.
52. Diorio D, Welner SA, Butterworth RF, Meaney MJ, Suranyi-Cadotte BE. Peripheral benzodiazepine binding sites in Alzheimer's disease frontal and temporal cortex. *Neurobiol Aging.* May-Jun 1991;12(3):255-258.
53. Nagler R, Savulescu D, Krayzler E, Leschiner S, Veenman L, Gavish M. Cigarette Smoke Decreases Salivary 18 kDa Translocator Protein Binding Affinity - in Association with Oxidative Stress. *Curr Med Chem.* May 24 2010;17(23):2539-2546.
54. Black KL, Ikezaki K, Toga AW. Imaging of brain tumors using peripheral benzodiazepine receptor ligands. *J Neurosurg.* Jul 1989;71(1):113-118.

55. Miettinen H, Kononen J, Haapasalo H, et al. Expression of peripheral-type benzodiazepine receptor and diazepam binding inhibitor in human astrocytomas: relationship to cell proliferation. *Cancer Res.* Jun 15 1995;55(12):2691-2695.
56. Hardwick M, Rone J, Han Z, Haddad B, Papadopoulos V. Peripheral-type benzodiazepine receptor levels correlate with the ability of human breast cancer MDA-MB-231 cell line to grow in SCID mice. *Int J Cancer.* Nov 1 2001;94(3):322-327.
57. Chauveau F, Van Camp N, Dolle F, et al. Comparative evaluation of the translocator protein radioligands 11C-DPA-713, 18F-DPA-714, and 11C-PK11195 in a rat model of acute neuroinflammation. *J Nucl Med.* Mar 2009;50(3):468-476.
58. Cleveland WS, Devlin SJ. Locally Weighted Regression - an Approach to Regression-Analysis by Local Fitting. *Journal of the American Statistical Association.* Sep 1988;83(403):596-610.
59. Innis RB, Cunningham VJ, Delforge J, et al. Consensus nomenclature for in vivo imaging of reversibly binding radioligands. *J Cereb Blood Flow Metab.* Sep 2007;27(9):1533-1539.
60. Logan J, Fowler JS, Volkow ND, Wang GJ, Ding YS, Alexoff DL. Distribution volume ratios without blood sampling from graphical analysis of PET data. *J Cereb Blood Flow Metab.* Sep 1996;16(5):834-840.
61. Rupprecht R, Papadopoulos V, Rammes G, et al. Translocator protein (18 kDa) (TSPO) as a therapeutic target for neurological and psychiatric disorders. *Nat Rev Drug Discov.* Dec 2010;9(12):971-988.
62. Politis M, Su P, Piccini P. Imaging of microglia in patients with neurodegenerative disorders. *Front Pharmacol.* 2012;3:96.
63. Ching AS, Kuhnast B, Damont A, Roeda D, Tavitian B, Dolle F. Current paradigm of the 18-kDa translocator protein (TSPO) as a molecular target for PET imaging in neuroinflammation and neurodegenerative diseases. *Insights Imaging.* Feb 2012;3(1):111-119.
64. Scarf AM, Ittner LM, Kassiou M. The translocator protein (18 kDa): central nervous system disease and drug design. *J Med Chem.* Feb 12 2009;52(3):581-592.
65. Venturini I, Zeneroli ML, Corsi L, et al. Diazepam binding inhibitor and total cholesterol plasma levels in cirrhosis and hepatocellular carcinoma. *Regul Pept.* Apr 24 1998;74(1):31-34.
66. Waterhouse RN, Mardon K, Giles KM, Collier TL, O'Brien JC. Halogenated 4-(phenoxy)methylpiperidines as potential radiolabeled probes for sigma-1 receptors: in vivo evaluation of [123I]-1-(iodopropen-2-yl)-4-[(4-cyanophenoxy)methyl]piperidine. *J Med Chem.* May 23 1997;40(11):1657-1667.
67. Pike VW. PET radiotracers: crossing the blood-brain barrier and surviving metabolism. *Trends Pharmacol Sci.* Aug 2009;30(8):431-440.
68. Imaizumi M, Kim HJ, Zoghbi SS, et al. PET imaging with [11C]PBR28 can localize and quantify upregulated peripheral benzodiazepine receptors

- associated with cerebral ischemia in rat. *Neurosci Lett*. Jan 16 2007;411 (3):200-205.
69. Fujimura Y, Kimura Y, Simeon FG, et al. Biodistribution and radiation dosimetry in humans of a new PET ligand, (18)F-PBR06, to image translocator protein (18 kDa). *J Nucl Med*. Jan 2010;51(1):145-149.
  70. Taliani S, Pugliesi I, Da Settimo F. Structural requirements to obtain highly potent and selective 18 kDa Translocator Protein (TSPO) Ligands. *Curr Top Med Chem*. 2011;11(7):860-886.
  71. Louis DN, Ohgaki H, Wiestler OD, Cavenee WK. *WHO Classification of Tumours of the Central Nervous System*2007.
  72. Tang D, McKinley ET, Hight MR, et al. Synthesis and Structure-Activity Relationships of 5,6,7-substituted Pyrazolopyrimidines: Discovery of a novel TSPO PET Ligand for Cancer Imaging. *Journal of Medicinal Chemistry*. 2013;Submitted.